A PROGRAM TO DEVELOP HIGH PERVEANCE IONIZERS

by

John C. Beynon and P. W. Kidd

Prepared for

NATIONAL AERONAUTICS AND SPACE ADMINISTRATION

N67-37657

(ACCESSION NUMBER)

(THRU)

(PAGES)

(CODE)

(NASA CR OR TMX OR AD NUMBER)

(CATEGORY)

FACILITY FORM 602

TRW.

SYSTEMS GROUP

A PROGRAM TO DEVELOP HIGH PERVEANCE IONIZERS

by

John C. Beynon and P. W. Kidd

Prepared for

NATIONAL AERONAUTICS AND SPACE ADMINISTRATION

Contract NAS3-7106

1 September 1967

Technical Management
NASA Lewis Research Center
Cleveland, Ohio
Spacecraft Technology Division

TRW SYSTEMS
One Space Park
Redondo Beach, California

TABLE OF CONTENTS

LIST OF ILLUSTRATIONS

Sometimes a few small breakthroughs add up to a lot. Our progress with the contact ion engine in a period of less than a year is an example.

First we found that the contaminated emitter problem was essentially a "remnant-oxygen" condition which increased the emitter temperature requirement by as much as 200°C (for the same neutral efflux).

Secondly we found that this "remnant-oxygen" condition could be eliminated by temporarily exposing an emitter to a partial pressure of acetylene gas. The cure was apparently permanent as long as no further oxygen or water vapor reached the emitter.

Third, the most probable cause of emitter contamination was identified as Step No. 21 in the fabrication process and the necessary corrective action taken.

Fourth, we developed a reasonably safe process for electropolishing an emitter's surface thereby improving the emittance by as much as a factor of 2 and neutral fraction by as much as 3.

Fifth, we proved that structurally stable nickel grids are compatible with our contact ion engine (as verified by prolonged life tests). Because of lower sputtering yield life is at least double that of the conventional copper electrode.

Sixth, the improvement in emittance by the electropolishing process focussed attention on the need for more efficient heat shielding. In post-contractual experiments* we have already reduced the thermal losses by 25%.

Individually these accomplishments are slight compensation for a period beset with repeated setbacks -- side leakage in emitters, boiler leakage, safety interlock malfunctions, power failures, etc. etc. etc.

---

* Emitter G-7-3 was electropolished and incorporated in a specially designed shielding arrangement with in-house funding.

Collectively, however, these small successes have produced a factor of eight reduction in the ionization energy requirement. This major advance in thruster technology makes the TRW Systems ion engine the most efficient ion thruster developed to date for comparable electrode durability.

It is with considerable satisfaction, therefore, that we review the progress achieved during four years of intensive effort. We would like to thank NASA Lewis Research Center for their support under NAS3-7106.

A PROGRAM TO DEVELOP HIGH PERVEANCE IONIZERS

by
John C. Beynon and P. W. Kidd

ABSTRACT

This is the final report for Contract NAS3-7106.

This year's work has consisted of the evaluation of several accelerator electrode materials for their compatibility with a cesium contact ion engine. Pure metals such as beryllium, iron, nickel and copper have been tested as well as several alloys including cupro-nickel, copper iridium, and nickel-iron alloys.

All of the above mentioned elements appear to be compatible with the contact engine. Prolonged tests with either iron or beryllium were unsuccessful however, due to warpage of grid bars during operation. This structural instability could presumably be corrected by a more sophisticated method of controlling the crystal growth during the wire drawing process. Since this was beyond the scope of contract NAS3-7106, TRW Systems was asked to and did propose a follow-on program for further studies with beryllium. However, the funding for this work was cancelled before a contract was awarded.

Six life tests were made during the course of this contract, four with copper electrodes and two with nickel. Both are quite satisfactory materials for the TRW Systems engine design. Although these tests ranged in duration from 100 to 524 hours, the neutral fraction was generally high. Equivalent operating time with an emitter yielding a 1% neutral fraction ranged between 770 and 7800 hours. From this data (and additional sputtering experiments) the end life of a nickel electrode in a 1% neutral environment, best state of the art emitter contouring accuracy, and an ion current density of 17 ma/cm^2 would be a minimum of 10,000 hours.

One very encouraging development in connection with the contact ion engine has been the identification and control of a recurrent "poisoning" problem which invariably led to high neutral fractions and high operating temperatures.

Subsequently, the low neutral fraction measurements with button ionizers (performed by Shelton, Cho and Hall) have been duplicated in engine tests. This fact combined with several improvements in the ionizer fabrication process has resulted in a significant improvement in ionizer efficiency.

1. INTRODUCTION

This is the final report for work accomplished at TRW Systems under contract NAS3-7106 for studies related to the durability and efficiency of high perveance contact ion engines.

It is a report of the proven feasibility of nickel as an electrode material for contact ion engines. This is the first time that materials other than copper have been successfully used for this application. Electrode life is thereby doubled.

It is also a report of important improvements in fabrication technology leading to better thermal efficiency and ionizer performance characteristics.

It is also the report of a solution to an emitter contamination problem which has severely handicapped our experiments during the past two years. The diagnostic technique of operating an ion engine alternately in an oxidizing and then reducing atmosphere has not only identified the performance of a contaminated emitter as one with a "remnant-oxygen" characteristic but provides means of obtaining the true emitter characteristic under adverse conditions.

It also includes the report of many failures – failure of beryllium as a successful electrode material because of fabrication difficulties – failure of life tests due to malfunction in safety interlocks or poor engine optics and many others. It is a report at the same time of the extremely exacting requirements that have been met in the fabrication and testing of a contact ion engine.

These and other pertinent data regarding the present program are grouped in the main body of this report in Sections 2 through 8 and Appendix I.

In Section 2 the present processing techniques of the TRW Systems high perveance contact ion emitter, accel electrode, and other engine parameters are described. This section also includes a production summary of 49 emitters fabricated during the past four years and describes the various techniques of fabrication employed. The more important achievements are recorded here:

    (1) The perfection of an electropolishing technique which yields a low emissivity and optimized microstructure for the porous tungsten surface;

(2) Potential elimination of the side leakage problem in the vapor plating process; and

(3) Modification of the contour machining operation so as to eliminate possible emitter contamination.

Section 3 describes and evaluates the pre-operative measurements for the several emitters which were used for the electrode material compatibility evaluation, the life tests and the emitter contamination studies.

Section 4 describes the electronic equipment and vacuum stations which are part of the engine test facility.

In Section 5 the operational performance of the four main emitters employed for electrode material evaluation and life tests are described. This data is preceded by a discussion of the correct interpretation of measured neutral measurements from either engine or button data and the contamination problem which has seriously handicapped both emitter and electrode material evaluation during the past two years.

Section 6 includes not only the results of a compatibility and feasibility evaluation of six accelerator electrode materials but also the results of two sputtering experiments. This latter data yields accurate relative sputtering yields for copper, nickel, cupro-nickel, iron, beryllium and silicon in a 2000 volt cesium ion beam.

Section 7 described six life tests ranging from 100 hours to 524 hours in duration. A discussion of both electrode and emitter durability is included here. Of the six life tests the first and last are probably the most important. In the first, a copper grid was operated for the equivalent of 16,000 hours operation for an emitter with .5% neutrals and a current density of .015 amperes per cm^2. The final test established the feasibility of nickel as an electrode material and the long term stability of the electropolished porous tungsten surface.

In Section 8 the present potential of the contact ion engine in the light of recent improvements in thermal efficiency are discussed. The importance of this development is illustrated by calculating electrode life and engine efficiency as a function of ion beam density for several of the better ionizer materials which have been tested at TRW Systems during the past few years.

2

In Appendix I the general equations for calculation of electrode life relative to either engine scale or operating specific impulse are established. This is a slightly modified version of the paper presented at the second International Conference on Electron and Ion Beam Science and Technology in New York (April 1966) under the title "Affects of Accel-Decel on Thruster Durability" by S. G. Forbes and J. C. Beynon.

It should also be understood that this is the report of a contact engine design which differs from that of either E.O.S., H.R.L, or NASA-Lewis in one important category: it is specifically designed to operate at high current densities at I_{sp}'s as low as 4000 seconds without the requirement of accel-decel. This is accomplished by employing a diode spacing of one millimeter and a parallel slit geometry with a one millimeter pitch.

This is less than one-half that used by other engine designers and as a consequence the machining tolerances are correspondingly smaller. The design is further restricted in fabrication techniques because of the small size. For example H.R.L.'s method of electron beam welding solid tungsten inserts to form the flute peaks of the emitter contour would be an extraordinary achievement when applied to the TRW Systems design. Each solid tungsten ridge is the equivalent of a triangular section .003 inches on a side and 1.2 inches long.

Why, then, has TRW Systems persisted in a design which appears to be ridiculously difficult? The reasons have changed to some extent with the improving technology. The early porous ionizer data indicated that very high current densities and a replaceable electrode structure were the only means of obtaining a long life at high efficiency. The present emitter was designed, fabricated and operated with a grid change mechanism and at current densities as high as 50 ma/cm^2.

The development of better ionizers from spherical tungsten brought about such a significant reduction in neutral fraction that it now appeared feasible to obtain an electrode life matching that of a practical mission at reasonably high current densities.

Re-evaluation of the TRW Systems design proved that greater electrode life would be obtained by increasing the diode spacing only in the case where the direct interception of the ion beam was the major source of electrode erosion. If the ion focussing optics could be generated with sufficient accuracy that charge exchange ions caused at least one half of the total erosion then maximum electrode life would be obtained by simple diode operation at the minimum (perveance limited) accelerating voltage required to achieve a given current density.

The most recent improvements in emitter fabrication — in particular the final electropolish of the contoured surface — have made a very significant improvement in both electrode life and engine efficiency. In fact it now appears that efficiencies significantly higher than that of the cesium bombardment engine can be achieved without replacing electrodes in a two year mission. There is one factor that is quite certain however. By scaling this engine up to a 2 mm spacing, electrode life would be reduced by a factor of 3 if the engine is operated at the same neutral fraction, net beam potential, and current density.* Because the electrode mass per unit area has also been increased by a factor of two, the arrival rate of sputtered material on the emitter is higher by a factor of six. A 3 mm diode engine would have 1/8th the life and a backsputtering rate 24 times that of the 1 mm engine!**

However, the development of the contact engine is incomplete. While this report proves that several significant improvements in technology have been achieved during this program many factors remain to be established:

(1) The long term stability of the emitter (in the absence of contaminants) with respect to permeability, emissivity, critical temperature and neutral fraction;

(2) The corresponding long term electrode durability which at present is only extrapolated from relatively short duration life tests; and

(3) The development of further improvements in shielding efficiency.

* .02 amps/cm^2 operation.

** For a complete analysis of the scaling laws see Appendix I of this report.

TRW Systems believes that the program which was interrupted early in 1966 was on the way toward answering these questions. Whether such a continued effort is warranted in the light of the excellent efficiencies and projected lifetime for other thrusters requires careful consideration however.

Perhaps the time has arrived when there is sufficient knowledge about practical electric propulsion missions of the immediate or more distant future to weigh the potential advantages of the cesium contact engine over other propulsion devices against the probable cost of completing this development.

Some of the more obvious advantages of the contact engine are

(1) higher thrust density

(2) less beam spread

(3) more easily scaled to the small size required for housekeeping missions.

other possible advantages might be

(1) higher rocket efficiency*

(2) less possibility of contaminating solar panels, etc., with neutral efflux

(3) a simpler power conversion requirement

(4) better weight-reliability capability.**

---

* Present and projected efficiency calculations in this report are based upon the requirements of electrically heating the ionizer. The radioisotope heated contact engine (TRW Patent No. 3210926, issued October 12, 1965) improves engine efficiency even further.

** In a system containing redundant thrusters.

2. FABRICATION

2.1 EMITTER FABRICATION

2.1.1 Basic Design

The basic emitter configuration is illustrated in the cutaway of Figure 1 and is fabricated by procedures outlined in the final report for Contract NAS3-5906.[1]

The original concept for this module originated in late 1961 and is designed for a 1 mm diode spacing. Correct ion optics is provided by contouring the face of the emitter with 52 grooves of .0225 inch radius across the width of the emitter on a 1 mm pitch. As confirmed by both computer analyses and actual operating data this flute radius provides slight over-focussing with emission limited operation and almost parallel ion beam in the case of space charge limited operation. Calculated perveance is 8 x 10^{-6} amps/$V^{3/2}$ at an aspect ratio of 45. Experimentally a somewhat higher voltage is required to minimize the neutral fraction – yielding a useable perveance of approximately 5 x 10^{-6} amps/$V^{3/2}$.

2.1.2 Production Summary (Evolution of Present Process)

Because of the contamination problem it is perhaps wise to review at this time the history of the production techniques used during the past few years.[1,2,3] The production summary of Table I is useful to illustrate some of the milestones in the development of this module.

Braze

Initially all brazes were made by Semicon of California using a molybdenum boron-carbide proprietary braze. Because at that time Semicon refused to reveal the constituents of the brazing alloy TRW Systems initiated a brazing evaluation program of its own and with emitters C-1 and C-2 attempted a vanadium braze. While the initial braze was excellent it was found that during side sealing operations (when the emitter was fired in hydrogen) the braze deteriorated severely. Consequently this process was discontinued and a rhodium braze evaluated. Rhodium has a short flow range due to the rapid alloying

Figure 1. Cutaway of a completed emitter.
(ST1-10)

TABLE I. TRW SYSTEMS EMITTER DESIGN - PRODUCTION SUMMARY

EMITTER CODE	EMITTER MATERIAL	CONTRACT*	BRAZE	SIDE SEAL	EMITTER CONTOUR	COMMENT
A-1	Semicon	1	1	1	2	Operated to 40 ma/cm^2
A-2	"	1	1	1	3	Inoperable due to leak
B-1, B-2	"	2	1	1	3	EDM after cesium operation
D-1 thru D-6	"	2	1	1	1	Low emissivity, side leakage
C-1, C-2	"	2	2	2	–	Vanadium braze failed
E-1, E-2	"	2	3	3	3	Side leaks after operation
E-3 - E-8	"	2	3	4,5	3	Best to date
F-1, F-2	Phillips	3	3	6	3	Vapor plate before braze
F-3 thru F-9	Spectramat	3	3	6	3	Vapor plate after braze Initiated kerosene flush
G-1	EOS	4	3	6	3	
G-2b	Hughes	4	3	6	3	Electropolish experiment by NASA
G-3	EOS	4	3	6	3	
G-4	EOS	4	3	6	3	First sputtered emitter
G-5	TRW Systems	4	3	6	4	Best solid ridges to date
G-4-2	EOS	5	3	7	4	
G-6(b)	Phillips	5	3	7	4	
G-6	Phillips	5	3	6	4	Best life test (electropolished
G-4-3	EOS	5	3	6	4	
ST1-10	TRW Systems	5	3	6	4	Terminated kerosene flush
ST1-12	TRW Systems	5	3	6	4	
G-3-2	EOS	5	3	6	4	
G-7-1	Hughes 324S	5	3	6	4	EDM too deep
G-7-3	Hughes 324S	5	3	6	4	Complete but not tested
E4-A	EOS	5	3	6	4	
G-7-2 etc.**	Various	5	–	–	–	

TABLE I (cont'd)

*	Contracts	1	TRW in-house funding	(1961-62)
		2	AF33(657)-8687	(1962-63)
		3	AF33(657)-10788	(1963-64)
		4	NAS3-5906	(1964-65)
		5	NAS3-7106	(1965-66)

** Machined Parts Inventory

        G-7-2, E7A, E7B, ST1-7, ST1-8.

Brazing Code: (1) Mo - B - C

              (2) Vanadium

              (3) Rhodium

Side Seal Code: (1) Semicon W-plate

               (2) Brazed side strips

               (3) Rhodium plate

               (4) Vapor plated tungsten (San Fernando Labs) sides only

               (5) Vapor plated tungsten (TRW Systems) sides only

               (6) Vapor plated tungsten (TRW Systems) sides and front

               (7) Vapor plated tungsten (San Fernando Labs) sides and front

Emitter Contour Code:

               (1) Cold machined (plastic infiltrated) by Semicon of California

               (2) EDM with copper electrode

               (3) EDM with graphite electrode

               (4) EDM with graphite (rough cut) followed by
                     EDM with copper infiltrated tungsten (finish cut).

with tungsten at its melting point and also tends to diffuse through the porous tungsten at emitter temperatures of operation. However because of the large distance between the brazed surface and the ion emitting area this diffusion has not been a problem. Side leakage due to poor flow characteristics of the braze is later overcome by vapor plating the sides and top of the emitter. Hence the rhodium braze has been retained to the present time.

Side Sealing

The original emitters were side-sealed by a proprietary "electra-plated" tungsten process of Semicon of California. The thickness of this tungsten plate ranged between 2 to 5 thousandths of an inch and it was found that after short operating periods with cesium side leaks developed. Attempts to seal the sides with brazed strips of tungsten or electroplated rhodium also proved unsatisfactory. Beginning with E-3 the emitter sides were sealed by vapor plated tungsten. This step was performed initially San Fernando Laboratories.* However, due to extremely long delays in delivery TRW Systems undertook an investigation of vapor plating techniques and developed a comparable process. It was found that with a plating thickness of .02 inches along the sides side leakage was no longer a problem (until recently).

Originally only the sides were vapor plated and the front surfaces of the emitter were masked by a graphite slab. Beginning with F-1 both the sides and front surface of the emitter were coated with vapor plated tungsten to minimize carbiding effects. All of the solid tungsten from the front surface was removed during the contouring. Beginning with F-3, however, an attempt was made to retain some solid tungsten at the flute tips to minimize direct interception of ions by the accelerating electrode in the region where the optics fail.** This is a difficult operation due to the accuracy requirements of measuring the emitter dimensions prior to and after vapor plating and

* San Fernando Laboratories, 10258 Norris St., Pacoima, California

** Due to a finite radius at the flute tips.

and retaining a reference base. However the majority of failures were due to flute chipping during the machining process -- a problem which was not resolved until the double electrode system described below was employed.

The side leakage problem had disappeared until quite recently. This is believed to be partially due to an excessive rhodium fillet on the outside edge of the braze junction -- a condition that has been subsequently corrected.

A recent communication with San Fernando Laboratories suggests that impurities in the tungsten hexafluoride may also be a causitive factor. They found that the free fluorine content of the WF_6 supplied to them by Allied Chemical had increased substantially during the past two years. This was discovered in searching for reasons why their customer's cesium diodes (fabricated from vapor plated tungsten) were developing leaks. Subsequently they have found that by maintaining the fluorine content below 20 p.p.m. they have been able to obtain a much more ductile deposit than they had ever obtained before. In fact, for the first time the deposits can be recrystallized by vacuum firing. More importantly, the void formation in the as deposited tungsten is no longer detectable.

Emitter Contouring

Emitter A-1 was contoured by electric discharge machining using a copper electrode and distilled water. Emitter A-2 also used distilled water but a graphite electrode was employed. Subsequent processing of emitters B-1 and B-2 which has been previously operated as ion emitters (using focus grid wires) proved extremely difficult. Subsequently kerosene was used as the dielectric.

Graphite was retained as the only machining electrode material through G-4 production. The primary advantage of this material is that it can be machined with a pre-ground broach providing excellent accuracy and reproducibility of the emitter contour. The electrode is a cylinder designed to machine 26 grooves on the first pass (at .08" pitch) and the remainder on the second pass (with a .04" upshift of the work). Tool rotation is geared so that the tool rotates less than 1/2 revolution per pass. This prevents tapering of a groove along its length due to electrode wear but does leave a fairly coarse surface finish.

11

Beginning with G-5, a tool fabricated from copper infiltrated tungsten and dimensionally identical with the graphite electrode wheel was added as a finishing tool. This electrode is used to remove the last two or three thousandths of an inch of the emitter surface and rotates at a reasonably high speed. Because of the smallness of the cut, tapering along the contour length is negligible. Since the inception of this finishing operation chipping of the solid tungsten flutes has virtually disappeared and the overall finish has improved. Extreme accuracy is required in transferring tools however.

Prior to emitter F-3 all emitters which had been contoured by electric discharge machining were completely clogged in the porous region. Throughput was only achieved by vacuum firing. This problem was overcome by introducing a backing pressure of fresh kerosene through the feed tube into the plenum chamber so that as soon as the machining reached the porous section of the emitter a reverse flow of kerosene would prevent clogging. The emitter could then be further flushed with either freon or acetone after the EDM.

During the routine flushing of emitter G-6 a dark colloidal deposit was withdrawn from the plenum chamber. This substance was later analyzed and found to contain oxides of the elements iron, nickel, copper, chromium, zinc, molybdenum and manganese. A sample of the kerosene which was used to flush through the emitter during the EDM machining was then passed through a sub-micron glass filter and a similar colloidal material collected. Analysis proved it contained essentially the same elements plus several others but in different proportions, as shown in Table II. This could be explained by varying amounts of brass, stainless steel and iron oxide as the major constituents.

The presence of such a contaminant within the plenum chamber of an emitter leads to several obvious deleterious effects. Cesium may gradually break down the oxides permitting the metal atoms to combine with the tungsten. Nickel is a notorious sintering agent as is iron. Diffusion of titanium or chromium to the surface would lead to a poisoned condition (according to Shelton). These facts appear to explain to a large extent, many of the poisoning problems experienced during the past year. Even though the contaminant would vary from emitter to emitter (depending upon the residue in the kerosene) gradual deterioration of ionizer performance is to be expected.

12

TABLE II. Comparison of residues from plenum
of Emitter G-6 and filtrate* of
kerosene used as emitter flush by the
L. C. Miller Co.**

Element	Percent of Total Metallics:	
	Kerosene Filtrate	Emitter G-6
Fe	∿81%	∿25%
Si	9.5	0.9
Cu	4.75	60
B	4.2*	––
Zn	.28	––
Cr	.12	2.5
Ni	.08	1.0
Ti	.05*	––
Mo	.01	––
Ag	.002	––
Mg	.001	––
Al	.0008*	––
An		10.5
Mn		.3

* Filtration was performed in a sub-micron glass filter. The detection of
the elements indicated by an asterisk may have been caused by portions of
this glass being included in the sample analysis.

Note: This compilation includes both x-ray diffraction and spectrographic
analysis. The latter was performed by the Atlas Testing Company.

** L. C. Miller had purchased this particular material from the Shell Oil Co.
as "freshly refined kerosene." In sampling a new shipment from Shell (in
a new barrel) similar impurities were found in colloidal suspension.

Subsequently the process has been changed. Preinfiltration of the porous section of the emitter with either polyethylene glycol or polystyrene coil dope has proven to be safe from the standpoint of not leaving a carbon residue (or the formation of tungsten carbide) during vacuum firing. Emitter G-7-1 was processed by flowing prefiltered kerosene through the plenum chamber during machining. This emitter was not tested, however, because no solid tungsten flute peaks were retained due to a machining error.

Electropolishing

Beginning with Emitter A-1 it was noted that the heat radiation from the front surface of the emitter was high. Measurements by Forbes and Shelton indicated an emissivity in the neighborhood of .3 to .4 compared with .2 for tungsten at 1500°K. This was distinctly higher than that exhibited by Emitters D-1 through D-6 which were fabricated by Semicon of California using cold machining of a plastic infiltrated porous tungsten. In the latter case an emissivity almost identical with that of solid tungsten was measured. Beginning with Emitter F-1 a final electropolishing process was added to the fabrication process. The procedure employed was that of placing the emitter fluted side down in a sodium hydroxide solution with a .020 inch diameter tungsten rod in the center of each contour radius to act as a cathode. This presents a uniform field to the emitter surface and minimizes enlargement of the contour radius.

While this led to a significant reduction in emissivity and an improvement in the porous surface structure, several emitters were effectively ruined by localized pitting at various sites over the emitter surface . Others became rejects because of areas where no metal had been removed because of a film of foreign material on the surface. The process was therefore discarded as being too dangerous.

During 1965 a program of investigating electropolishing of porous tungsten was initiated at Oak Ridge under NASA sponsorship. Emitter G-2b was electropolished at Oak Ridge apparently using a single remote cathode. The surface finish was excellent. However, a noticeable increase in flute radius occurred and a few pits were noted.

In order to improve the electropolishing process a rather complete study was initiated on October 1, 1965 at TRW Systems. As a result a process has been developed which:

(1) virtually eliminates the pitting problem;

(2) does not significantly alter the contour optics;

(3) yields the emissivity of solid tungsten; and

(4) improves the surface microstructure without significantly enlarging the pores.

The more important findings leading to the present process are listed below.

1. Tungsten is removed anodically in a hydrogen solution at the rate of 1/6 mole per Faraday. With sodium hydroxide as the electrolyte ion flow rate is controlled by a viscous layer which is unstable. This is probably a tungsten hydroxyl compound that tends to decompose into an oxide. If this layer is not continuously washed away by the electrolyte a slow etching occurs rather than a polish.

2. The thickness and viscosity of this viscous layer increases with concentration of the hydroxide. At or above 1% concentration the removal rates of either porous or solid tungsten will be equal and a smooth surface will result if the flow rate of this viscous layer over the surface is relatively slow and free of gaseous agitation.

3. Pitting can be caused by the presence of undissolved hydroxides at various sites. This causes local areas of high concentration which increases the metal removal rate.

4. Pitting may also be caused by the presence of impurities imbedded in the tungsten which are not attacked by the hydroxyl ions, do not form viscous layers, and cause a considerable evolution of oxygen due to the reaction at the anode

$$4 \ (OH)^- \rightarrow 4e^- + 2 \ H_2O + O_2$$
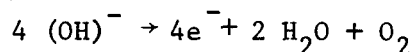
The scrubbing action of the evolved gas can break up the viscous layer on the tungsten in the immediate vicinity. There may also be a further increase in reaction rate because of localized heating (the absence of a viscous layer lowers the resistance between anode and cathode by as much as a factor of ten). Materials such as copper, silver, gold, Pt, Rh, Rh-Mo, and stainless steel have this characteristic.

5. By vacuum firing just prior to electropolishing most surface contaminants are removed. By thoroughly flushing the porous tungsten with distilled water and electrolyte any soluble residues are removed before voltage is applied.

6.   Drawing of fresh electrolyte through the porous tungsten immediately following the polishing cycle prevents oxide precipitation. The solution drawn from the pores is a deep blue in color. This coloring which has not (as yet) been chemically identified disappears in a few minutes.

7.   By having the emitter tilted at an angle of 45° to allow free flow of the viscous fluid and employing the close-spaced tungsten grid mentioned above as the cathode, a uniform polish results, with only slight rounding of the flute peaks (a radius of less than .0005" has been observed when .001" of tungsten is removed from the surface).

The step-by-step proceeding employed in the present process is outlined in the next section. The overall results have been extremely gratifying. The improved surface finish is illustrated in Figures 2 and 3 (which represent Emitters G-6 and ST1-12 respectively) showing the microstructure before and after polishing. The lower emissivity also provides a significant improvement in the electrical efficiency.

2.1.3 Present Process

The various steps in the production of an emitter are listed in Table III. Many of these were described in detail in NASA CR-54325. The critical areas in the process are: (1) vapor plate, (2) electric discharge machining, and (3) electropolish. These particular operations are described in greater detail below.

Vapor Plate

The various changes that were made in the vapor plating process during 1965 are summarized in Table IV.

(1)   Parts and Apparatus

a. Emitter

b. Emitter heaters – 2 each 30 in. long x .023 tungsten wire threaded through alimina tubing

c. Carbon support boat (which prevents tungsten deposition on lower half of emitter)

d. Quartz emitter support

e. Quartz bell jar (or Vycor)

f. (1) Tank hydrogen

g. (1) Tank Tungsten hexafluoride (5 lbs.)

16
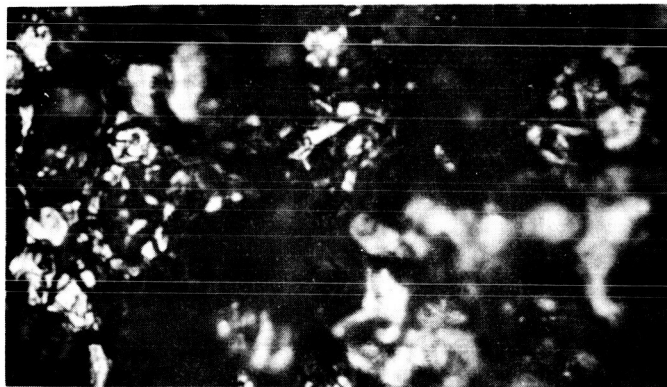
X700

(a) G-6 after elox

X700

(b) G-6 after electropolish

Figure 2. Emitter G-6 porous surface before
and after electropolishing.
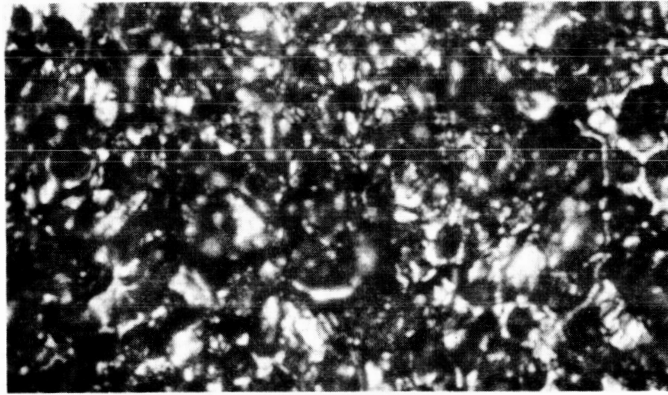
X700

(a) ST1-12 after elox

X700

(b) STL-12 after electropolish

Figure 3. ST1-12 surface finish before and
after electropolishing.

18

TABLE III. PRODUCTION CHART

OPERATION	DATE		Operator	Remarks
	Start	Finish		
1. Infiltrate with _____				
2. Cut blanks note positions assign numbers				
3. Machine				
4. Metallurgically polish				
5. Etch inside plenum				
6. Defiltrate				
7. Photograph 9 areas for pore count				
8. Density by Hg immersion				
9. Transmission coefficient (9-points)				
10. Total transmission				
11. Braze feed tube to plenum & base				
12. Leak check feed tube braze				
13. Braze emitter to base-feed-tube assembly				
14. Inspect braze fillets & minimize as required				
15. Photograph bubble test under freon Threshold photo Uniform pattern photo				
16. Transmission measurement				
17. Dimension check				
18. Fire 1500°C min for cleanup				
19. Vapor plate				
20. Leak check vapor plate & feed tube braze				

Departures from Listed Operations

_____

_____

_____

_____

Porous Material Source:

_____

Page 1 of 2

Emitter No._____

TABLE III.   (cont'd)

OPERATION	DATE		Operator	Remarks
	Start	Finish		
21. Prepare for elox				
22. Elox sides				
23. Leak check sides & feed tube braze				
24. Elox Grooves				
25. Elox Mounting Holes				
26. Remove elox coolant & infil-trant				
27. Leak check sides & FTB				
28. Vacuum fire for clean-up				
29. Leak check				
30. Transmission check				
31. Photograph surface (225X)				
32. Bubble test photograph (225X)				
33. Braze feed tube fitting				
34. Leak check sides FTB				
35. Photograph				
36. Electro-polish photograph and fire for clean-up				
37. Assemble in Engine				

Departures from Listed Operations

Porous Material Source:

20

Emitter No._____

TABLE IV. REVISIONS TO CHEMICAL VAPOR PLATING APPARATUS

Item	Material or Arrangement January 1965	Material or Arrangement December 1965	Reason for Change
Heating of Plated Emitter	RF Induction	Internal Heater	To obtain control of temperature. RF coupling changed during plating process requiring continual readjustment
Reactant Mixture Distribution	Perimeter feed close to emitter	Broadcast feed remote from emitter	Excessive buildup of W on corners, non-uniform coating
WF_6 and H_2 Lines	Tygon, Copper, Glass	Stainless steel, minimum glass	Water content of tygon resulted in leaching of glass and silicon deposition in tungsten
Reactant Jar	Pyrex	Vycor	Leaching of pyrex and deposition of silicon in deposited tungsten
WF_6 Flow Measurement	Orifice & Upstream pressure	Float flow meter	Gas flow measurement not reliable because orifices sometimes plugged
H_2 Flow Measurement	Orifice & Upstream pressure	Float flow meter	
Vacuum valve Gas control valves Reactant jar closures	Brass	Stainless steel	Etching of metal and deposition of products in vapor deposited tungsten
Reactant Jar "O" Rings	Neoprene	Viton A	Decomposition of Neoprene

21

h. A special vacuum system

i. Suitable meters, gages and electrical power

j. Fore vacuum pump which exhausts the reaction product gases through a series of liquid nitrogen filled Dewar flasks.

(2) Process

The vapor deposition of tungsten occurs when a partial pressure of tungsten hexafluoride and hydrogen is incident upon a heated emitter. One of the major by-products of this reaction is hydrofluoric acid. The temperature of the work is maintained at 550°C using a chromel-alumel thermocouple attached to the bottom of the emitter. The thermocouple is spotwelded using a platinum flux. A quartz tube shields the thermocouple for approximately 3" down from the emitter. This operating temperature was chosen to obtain an optimum plating rate, crystal size and uniformity.

The WF_6 flow rate is 100 cc/min. The hydrogen flow should be 2 SCFH H_2 measured on an Airco flow gage. (Note: Upstream tank pressure must be 30 psi for flow gage to be accurate.)

Prior to vapor plating the emitter is heated to 1000°C in a partial pressure of H_2 and held at this temperature for 5 minutes. Power is then turned off. After cooling the emitter surface is closely inspected for any foreign particles. If none are found temperature is raised to 550°C. Hydrogen flow is initiated and set at the desired rate before introducing the WF_6. On start-up the valve directly under the quartz tube is left open and the main chamber valve is closed. After several minutes of operation a sudden rise in chamber pressure indicates that the pores in the emitter have been sealed. At this point the main chamber valve is cracked and the emitter valve closed. All further pressure control is obtained via the chamber valve. Normal operating pressure is about 1/2 atmosphere. The liquid nitrogen traps should be filled after the emitter has been inspected following preheat. A large amount of HF acid will be trapped during the course of a 2 hour run. These traps are very dangerous and the frozen HF must be disposed of very carefully. (Note: The traps should be placed in a fume hood and allowed to warm up. Tap water should be left on. Do not attempt to pour water into the frozen traps. Do not leave fume hood window up.)

22

In a 2 hour period the tungsten deposit will range between .028 and .032 inches in thickness.

A typical quantitative analysis of the impurities in our vapor plated tungsten is included in Table V. Al, Cu and Si are the only positively identified contaminants.

Electropolishing

(1) Preparation

The sides and bottom of the emitter are mechanically and electrolytically polished after which the emitter is vacuum fired at 1500°C for 30 minutes and the feed line coupling is brazed to the feed tube. For electropolishing, the feed tube and sides and bottom of the emitter are coated with Micropeel* and the feed tube is connected to a filter flask which is a part of a manifold which can be either pressurized or evacuated. In a special fixture a grid is placed in front of the emitter so that a 0.020" diam. tungsten rod is suspended above each contour and its center is .005 inch closer to the emitter than the contour radius.

(2) Polishing Procedure

The assembly is placed in a tank containing a 1% solution of NaOH at room temperature with the emitter tilted at 45° to the vertical.

Electrolyte is drawn through the emitter into the filter flask until all of the trapped gases have been removed. The filter flask is then raised to atmospheric pressure and polishing is begun at 4.5 volts for a period of between 20 and 30 ampere minutes. This is sufficient to remove between .5 and .7 thousandths of an inch of tungsten from the contoured surface.

The filter flask is immediately evacuated at the conclusion of the polishing until sufficient electrolyte is drawn through the emitter that reaction products are well diluted. These reaction products are detected by a deep indigo blue coloring entering the filter flask which later becomes transluscent. Electrolyte is then replaced by distilled water and continual flushing is maintained until a neutral Ph is obtained.

* Micropeel manufactured by Michigan Chrome and Chemical Co., Detroit, Michigan.

TABLE V. Certified Report of Spectrographic Analysis
of Vapor Plated Tungsten

Sample No. G-4-3

Tungsten	Rem.
Silver	1 PPM*
Aluminum	10 PPM (det. limit 1)
Boron	10 PPM*
Barium	3 PPM*
Beryllium	1 PPM*
Bismuth	1 PPM*
Cobalt	3 PPM*
Chromium	3 PPM*
Copper	5 PPM (det. limit 1)
Magnesium	1 PPM*
Manganese	1 PPM*
Molybdenum	30 PPM*
Niobium	100 PPM*
Nickel	1 PPM*
Lead	3 PPM*
Tin	3 PPM*
Silicon.	20 PPM (det. limit 3)
Titanium	2 PPM (det. limit 3)
Vanadium	1 PPM*
Zirconium	30 PPM*
Total other elements . .	300 PPM*

* Indicates Detection Limit

Analysis Performed by: Materials Testing Laboratories
Division of Magnaflux Corporation
6800 E. Washington Blvd.
Los Angeles 22, California

After flushing, the plastic coating is removed and the emitter is re-fired in vacuum. It is now ready for assembly into an engine.

2.2 ACCELERATOR GRID DESIGN AND FABRICATION

This design evolved from the previous requirement* of a replaceable lightweight grid using copper grid bars. While a larger frame, (providing a greater length of support for the grid bars) is obviously desirable, the corresponding engine redesign requirements were considered too costly for the present program.

A grid assembly consists of 53 grid bars of dimensions .018" x .035" x 1.5" are lightly retained in a slotted graphite frame. Two U-channels of .002 inches thick tungsten slip over the sides of the frame. A thin sheet of graphite is sandwiched between the U-channel and the graphite frame on the slotted side. By having each grid bar in contact with graphite alone the sticking probability is quite low -- at least for Cu and Ni. The assembly is completed by grid indexing step-pins which are press-fitted into the graphite to retain the U-channels. The slotting pitch in the grid frame is .0402 inches. The thermal expansion of graphite and grid temperature is such that a perfect match occurs between it and the emitter when the latter is operated at 1500°K. Because of the low expansion coefficient of graphite a 200°C change in emitter temperature will change the registration at either end of the emitter by less than .001".

Copper, Cupron (or Cupro-Nickel) and nickel grid bars are prepared by rolling .026" wire to the dimension .018" x .034". This step is followed by electric heating to preanneal the wire and then a 10 to 15% draw. Individual grid bars are cut to length on a specially fashioned shear which leaves no burr. The bars are then cleaned and assembled into a grid frame. The completed assembly is vacuum fired at 700° to 900°C for out-gassing and to check the bars for possible warpage.

* Contract AF33(657)-10788 Statement of Work.

Iron grid bars have been more difficult to fabricate and require a more elaborate heat treatment. So far, however, a satisfactory process has not been developed. In general this material is much more subject to warpage during operation than nickel, copper or nickel-copper alloys.

Attempts to fabricate a stable beryllium grid assembly has so far proved unsuccessful. The major difficulty with beryllium has been the structural instability of the material. The most likely causes of this defect now appears to be (a) residual stresses in the processed bars and (b) random internal occlusions for those grid bars which were processed from pressed and sintered sheet. Two fabrication procedures were attempted: (1) Brush beryllium pressed and sintered sheet which had been preannealed was processed into grid bars by a photoetching technique. These grid bars generally failed after a few minutes of operation in an ion beam. (2) Better results were obtained by rolling .02" dia. beryllium wire and then using the same processing as that for copper or nickel. Beryllium has a greater tendency to weld to graphite than copper or nickel. However in experiments with a nickel plated grid frame the bars warped without sticking.

Because of the extremely low sputtering cross-section of beryllium a contract extension was initiated by NASA to study the processing of beryllium. However this funding was later cancelled.

2.3   ENGINE ASSEMBLY

A grid change mechanism which was developed under a previous contract[3] has been retained as a useful means of evaluating the influence of grid materials on an emitter and also for checking its emissivity by measuring the heating requirements with and without a special grid containing a tungsten sheet of emitter dimensions (see Section 8 of this report).

The basic functional arrangement of the engine components is illustrated in the cutaway drawing of Figure 4. When the grid lock bars are in the position shown the grid is registered with respect to the emitter. Removal of a grid is accomplished by rotating the eccentric rotary shafts on either side 180° which then allows free sliding of the grid frame along the grid slide rail. The grids are stored in a grid cartridge for post examination or re-use as desired. Figure 5 is a photograph of an engine mounted on a base plate.

GRID REGISTRATION PIN

GRID SIDE RAIL

POROUS TUNGSTEN

GRID LOCK BAR

DENSE TUNGSTEN

PLENUM CHAMBER

HEATER ELEMENT

HEAT SHIELDS

EMITTER MOUNTING ROD

ENGINE FRAME

SAPPHIRE ACTUATOR PIN

ECCENTRIC ROTARY SHAFT
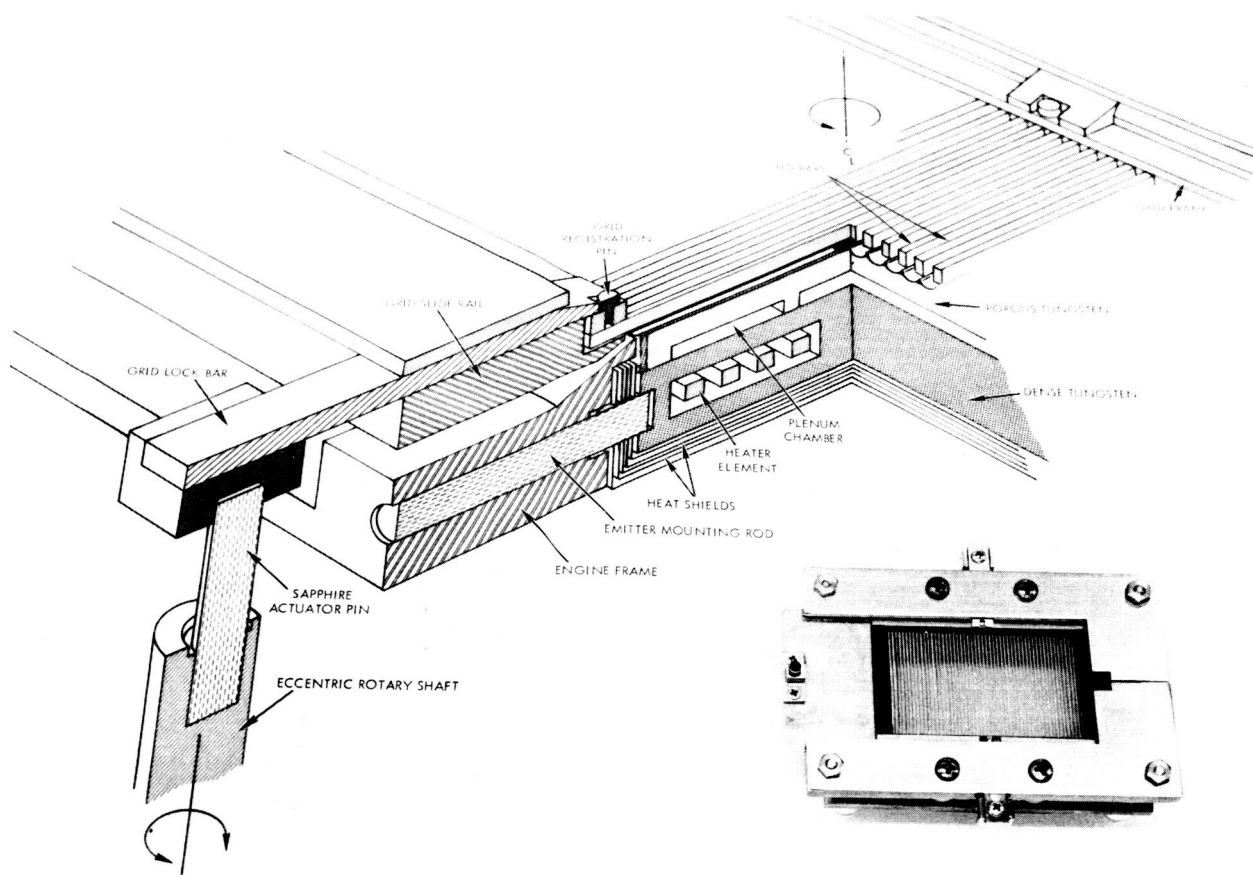
Figure 4.   Photograph and cutaway drawing of engine module

27
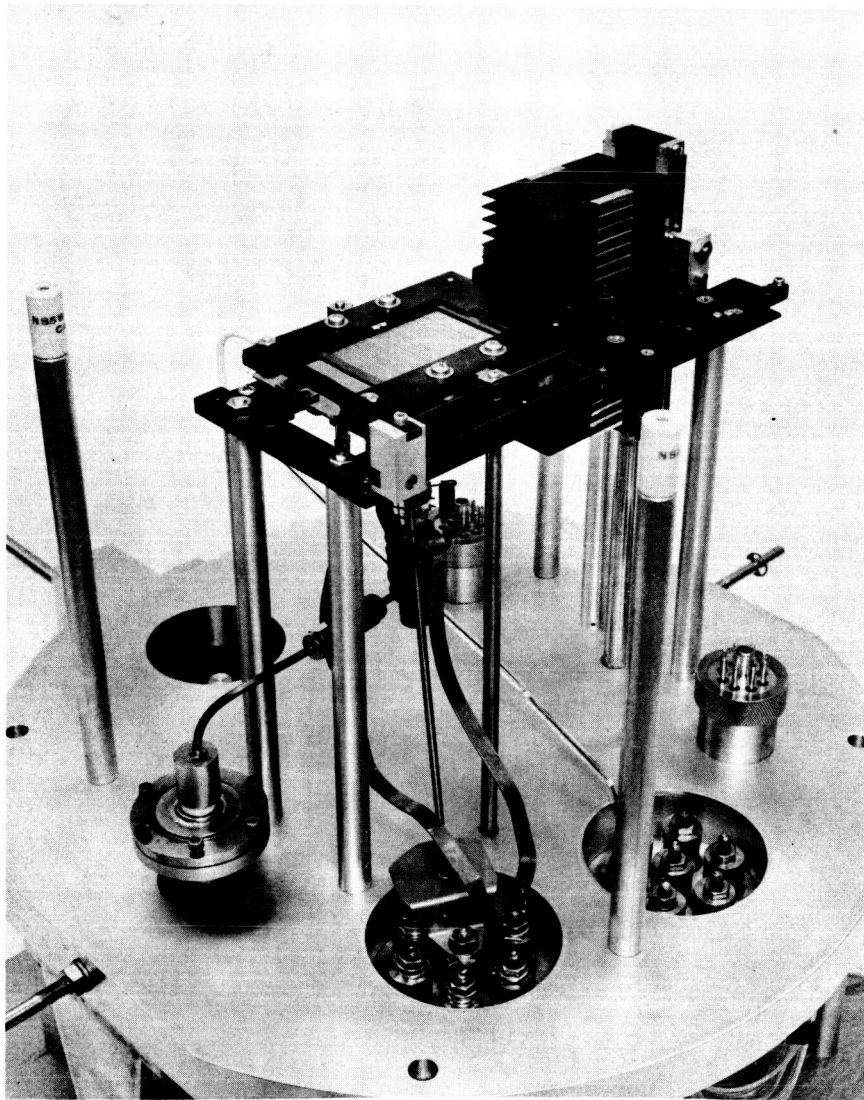
Figure 5. Single module engine with grid changer.

The only change in this design during the present program has been that of replacing all molybdenum parts with either tungsten or rhenium. This eliminates the possibility of emitter contamination with molybdenum which might occur when the emitter is operated in a partial pressure of oxygen. (Molybdenum oxide is quite volatile). While this lowers the thermal efficiency of the engine (molybdenum heat shields were previously employed). Engine efficiency was not of primary concern in this program.

3. PRE-OPERATIVE EMITTER TESTING AND EVALUATION

3.1 GENERAL DISCUSSION

The Shelton et al button tests have shown that the latest spherical tungsten compacts with or without additives such as iridium, rhenium or tantalum are a significant improvement over the angular crushed tungsten powder ionizers (with perhaps the exception of the Spectramat 1-10 micron powder lot). One of the prime objectives of this program has been to determine if these properties can be reproduced in a large high perveance thrustor.

The main anticipated difficulty is that of maintaining uniform beam density (i.e. permeability uniformity) in such a large compact. Variations in pore density and permeability can be detected to some degree by the preoperative analysis which is part of the present fabrication procedure. These can be later correlated with actual performance data. Non-uniform throughput can be expected to raise the neutral fraction and also the critical temperature since the region of highest cesium gas flow will produce ion current densities well above the average measured beam density.

These various pre-operative measurements are classified below under the headings of "pore data," "bubble patterns" and "microphotography."

3.2 PORE DATA

Transmissivity, pore count, and pore size data are listed in Table VI through X for emitters G-4-2, G-4-3, G-6, G-6(b), and G-3-2 respectively. As is to be expected, the transmission of spherical tungsten emitters is much lower than that of the angular tungsten powders [G-6 and G-6(b)]. Transmission uniformity over the 9 areas was quite good for each emitter. Pore count and pore diameter measurements are not much different for either the angular or spherical tungsten compacts. This latter data is somewhat suspect however, particularly when considered in relation to the photomicrographs of the metallographical polished samples of Figure 6. It is difficult to conceive of how the pore count of G-6(b) could be only 20% less than that of G-4-3. Average pore size according to the count is almost identical for these two samples.
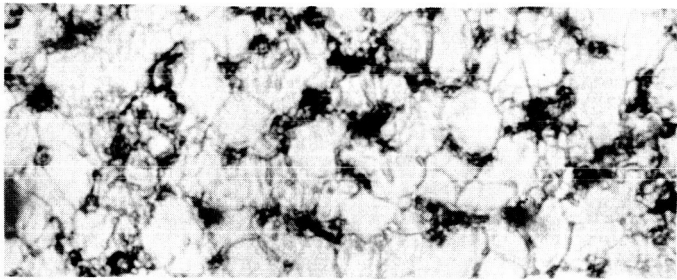
(a) Emitter G-6 material

(b) Emitter G-6(b)
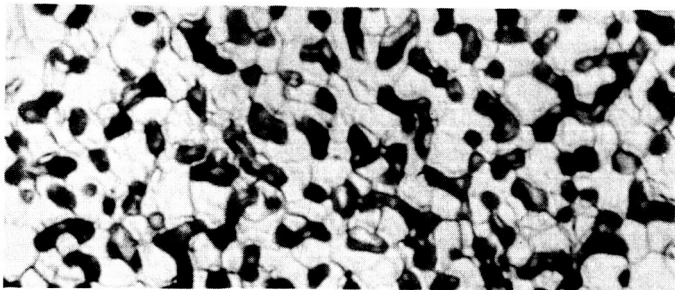
(c) Emitter G-3

(d) Emitter G-4-3

(e) Hughes' 324-S material

(f) TRW tungsten-rhenium alloy
with the sigma phase removed to
obtain interconnecting porosity

Figure 6. Photomicrographs of various ionizer
materials (after metallographic
polishing).

Figure 6 is a good illustration of the progress in contact ion emitter material development during the past few years. G-6(b) and G-6 essentially represent this state-of-the-art as it was in 1961 to 1962. G-3 and G-4 might be representative of the earlier spherical tungsten compacts. Hughes 324-S m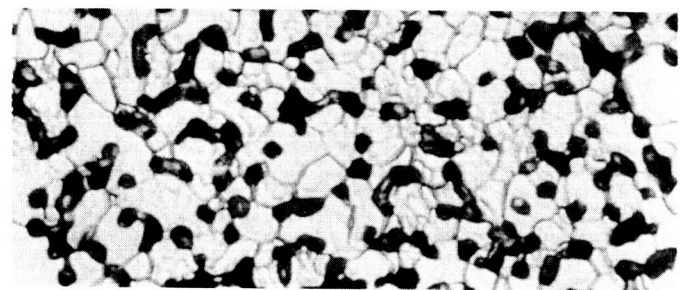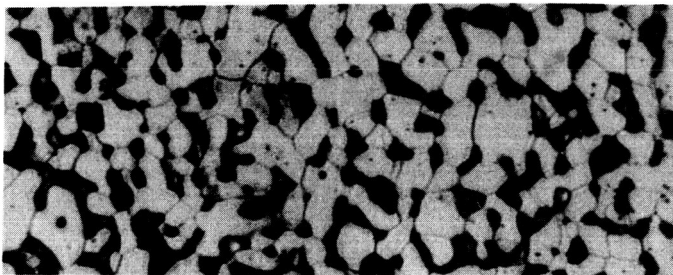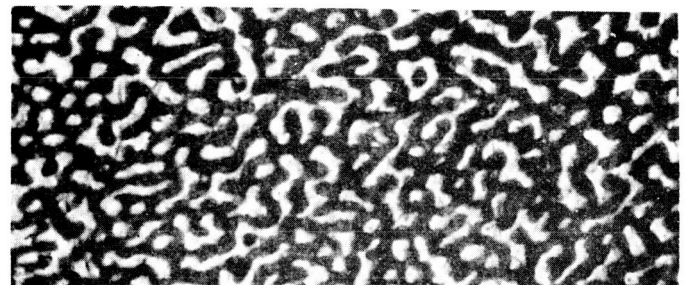aterial (from which G-7-1, and G-7-3 emitters were fabricated) shows an improvement in pore distribution. The final microphotograph represents the formation of porous tungsten from a special tungsten-rhenium alloy — a TRW Systems development.[4]

3.3   BUBBLE PATTERNS

Bubble tests, while not a conclusive evaluation of permeability uniformity do detect gross differences in transmission which might be caused by internal cracking or localized voids. It is essentially a quick over-all check (the transmission measurements of Tables VI through X are only localized spot checks).

This technique of submerging an emitter in chemically pure acetone and forcing argon gas through the emitter by way of the feed tube is also useful in detecting leaks through the sides or bottom of the emitter. Leak checks were normally made at 8 to 10 p.s.i. Since the recent side leakage problem developed, this pressure limit has been raised to 20 p.s.i.

Figure 7 contains photographs of the bubble pattern for several emitters taken immediately after brazing. From these tests one would rate these emitters in descending order of throughput uniformity as G-6(b), G-4-2, G-7-1, G-4-3, G-7-3, and ST1-10. ST1-10 is so non-uniform that it probably would be useless as an emitter. This is one of the reasons that it was selected for sectioning after completion of the vapor plate and contouring by E.D.M.

Another useful function of the bubble test is that of comparing the gas bubble patterns of the as-brazed emitter with the finished product as illustrated in Figure 8. G-6 shows excellent uniformity in both cases. ST1-12 shows the same basic pattern of nonuniformity in both cases. This indicates that the emitter characteristics have not been significantly altered by the vapor plating or electric discharge machining operations. The fine streaming of the gas bubbles for the electropolished emitter (ST1-12) is an indication of an improved surface microstructure over that of the original as-brazed surface.

FEED TUBE END

1
Pore Count 5.7 x 10^6
Pore Size 1.9 microns
Transmission 5.8 x 10^{-5}
Relative J

2
Pore Count 6.2 x 10^6
Pore Size
Transmission 5.9 x 10^{-5}
Relative J

3
Pore Count 6.1 x 10^6
Pore Size
Transmission 5.7 x 10^{-5}
Relative J

4
Pore Count 6.0 x 10^6
Pore Size
Transmission 6.3 x 10^{-5}
Relative J

5
Pore Count 5.9 x 10^6
Pore Size
Transmission 6.4 x 10^{-5}
Relative J

6
Pore Count 6.2 x 10^6
Pore Size
Transmission 6.2 x 10^{-5}
Relative J

7
Pore Count 5.8 x 10^6
Pore Size
Transmission 5.9 x 10^{-5}
Relative J

8
Pore Count 5.6 x 10^6
Pore Size
Transmission 6.1 x 10^{-5}
Relative J

9
Pore Count 5.5 x 10^6
Pore Size
Transmission 6.2 x 10^{-5}
Relative J

Density 78.5%
Average transmissivity = 6.1 x 10^{-5}
Total transmissivity = 5.5 x 10^{-5}
Mean Pore Count = 5.9 x 10^6

Emitter - Top View

TABLE VI

Material E. O. S.

Lot W.A. 5141

Sample (Emitter G-4 No. 2)

FEED TUBE END

1 Pore Count 4.65 x 10^6/cm^2 Pore Size 1.909 μ Transmission 5.0 x 10^{-5} Relative J	**4** Pore Count 4.53 x 10^6/cm^2 Pore Size 1.987 μ Transmission 5.2 x 10^{-5} Relative J	**7** Pore Count 4.54 x 10^6/cm^2 Pore Size 1.988 μ Transmission 5.4 x 10^{-5} Relative J
2 Pore Count 4.70 x 10^6/cm^2 Pore Size 1.874 μ Transmission 5.4 x 10^{-5} Relative J	**5** Pore Count 4.73 x 10^6/cm^2 Pore Size 2.020 μ Transmission 5.5 x 10^{-5} Relative J	**8** Pore Count 4.46 x 10^6/cm^2 Pore Size 1.992 μ Transmission 5.6 x 10^{-5} Relative J
3 Pore Count 4.65 x 10^6/cm^2 Pore Size 2.042 μ Transmission 5.5 x 10^{-5} Relative J	**6** Pore Count 4.59 x 10^6/cm^2 Pore Size 2.028 μ Transmission 5.9 x 10^{-5} Relative J	**9** Pore Count 4.54 x 10^6/cm Pore Size 1.959 μ Transmission 5.6 x 10^{-5} Relative J

Material   E.O.S.

Lot   WA 5141

Sample   G-4 No. 3

Emitter - Top View   TABLE VII

Density   78.60%

Average Pore Density: 4.60 x 10^6/cm^2
Average Pore Size: 1.978 μ
Average Transmissivity: 5.4 x 10^{-5}
Total Transmissivity: 6.5 x 10^{-5}

34

FEED TUBE END

1	4	7
Pore Count 3.72 x 10^6/cm^2 Pore Size 1.96 μ Transmission ___ Relative J ___	Pore Count 3.92 x 10^6/cm^2 Pore Size 2.127 μ Transmission 2.0 x 10^{-4} Relative J ___	Pore Count 3.83 x 10^6/cm^2 Pore Size 2.064 μ Transmission 2.0 x 10^{-4} Relative J ___
2	**5**	**8**
Pore Count 4.08 x 10^6/cm^2 Pore Size 1.971 μ Transmission 2.8 x 10^{-4} Relative J ___	Pore Count 3.92 x 10^6/cm^2 Pore Size 2.083 μ Transmission 2.0 x 10^{-4} Relative J ___	Pore Count 3.98 x 10^6/cm^2 Pore Size 2.027 μ Transmission 2.0 x 10^{-4} Relative J ___
3	**6**	**9**
Pore Count 3.88 x 10^6/cm^2 Pore Size 2.065 μ Transmission 2.0 x 10^{-4} Relative J ___	Pore Count 3.80 x 10^6/cm^2 Pore Size 2.079 μ Transmission 2.0 x 10^{-4} Relative J ___	Pore Count 3.92 x 10^6/cm^2 Pore Size 2.020 μ Transmission 2.0 x 10^{-4} Relative J ___

Density 77.98%

Average Pore Density: 3.89 x 10^6/cm^2
Average Pore Size: 2.045 μ
Average Transmission: 2.1 x 10^{-4}
Total Transmission: 1.8 x 10^{-4}

Emitter - Top View

TABLE VIII

Material Phillips Mode E

Lot ___

Sample G6B

1		
Pore Count _____	2 Pore Count _____	3 Pore Count _____
Pore Size _____	Pore Size _____	Pore Size _____
Transmission 2.2×10^{-4}	Transmission 2.1×10^{-4}	Transmission 2.1×10^{-4}
Relative J _____	Relative J _____	Relative J _____

4		
Pore Count _____	5 Pore Count _____	6 Pore Count _____
Pore Size _____	Pore Size _____	Pore Size _____
Transmission 2.2×10^{-4}	Transmission 2.2×10^{-4}	Transmission 2.1×10^{-4}
Relative J _____	Relative J _____	Relative J _____

7		
Pore Count _____	8 Pore Count _____	9 Pore Count _____
Pore Size _____	Pore Size _____	Pore Size _____
Transmission 2×10^{-4}	Transmission 2.2×10^{-4}	Transmission 2.1×10^{-4}
Relative J _____	Relative J _____	Relative J _____

FEED TUBE END

Density __71.44%__
Average transmissivity: 2.1×10^{-4}
Total transmissivity: 2.9×10^{-4}

Emitter - Top View

Material ____ Phillips Mod E

Lot ____

Sample ____ G6

TABLE IX

36

FEED TUBE END

1
Pore Count $4.50 \times 10^6/cm^2$
Pore Size 2.091 μ
Transmission 4.8×10^{-5}
Relative J

2
Pore Count $4.77 \times 10^6/cm^2$
Pore Size 2.161 μ
Transmission 5.5×10^{-5}
Relative J

3
Pore Count $4.74 \times 10^6/cm^2$
Pore Size 2.086 μ
Transmission 5.8×10^{-5}
Relative J

4
Pore Count $4.68 \times 10^6/cm^2$
Pore Size 2.105 μ
Transmission 5.1×10^{-5}
Relative J

5
Pore Count $4.85 \times 10^6/cm^2$
Pore Size 2.112 μ
Transmission 5.5×10^{-5}
Relative J

6
Pore Count $4.81 \times 10^6/cm^2$
Pore Size 2.093 μ
Transmission 5.8×10^{-5}
Relative J

7
Pore Count $4.77 \times 10^6/cm^2$
Pore Size 2.017 μ
Transmission 5.3×10^{-5}
Relative J

8
Pore Count $4.81 \times 10^6/cm^2$
Pore Size 2.087 μ
Transmission 5.6×10^{-5}
Relative J

9
Pore Count $4.91 \times 10^6/cm^2$
Pore Size 2.055 μ
Transmission 5.5×10^{-5}
Relative J

Density 78.78%
Average Pore Density: $4.76 \times 10^6/cm^2$
Average Pore Size: 2.090 μ
Average Transmission: 5.5×10^{-5}
Total Transmission: 6.25×10^{-5}

Emitter - Top View

TABLE X

Material   E. O. S. 1-10μ

Lot

Sample   G-3 No. 2

37
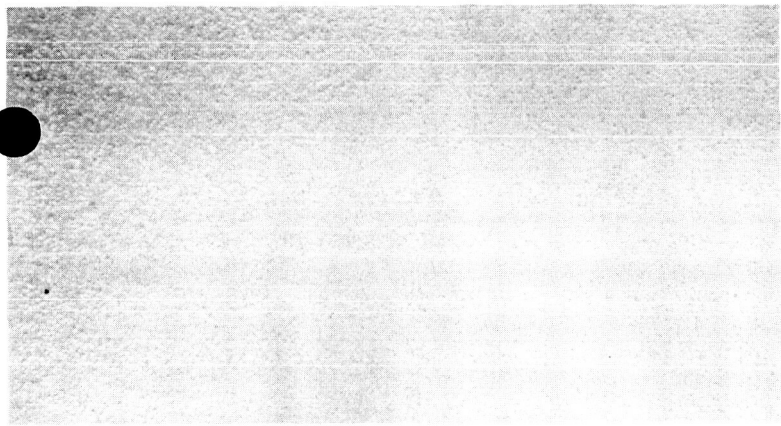
(a) G-6(b) [2.5 psi]
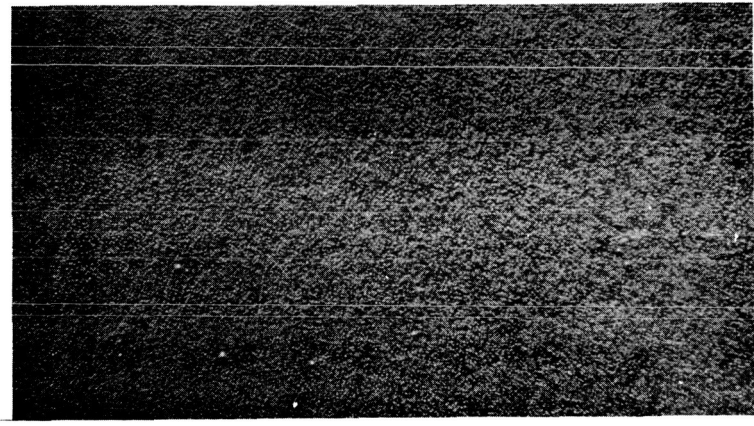
(b) G-4-2 [4.5 psi]
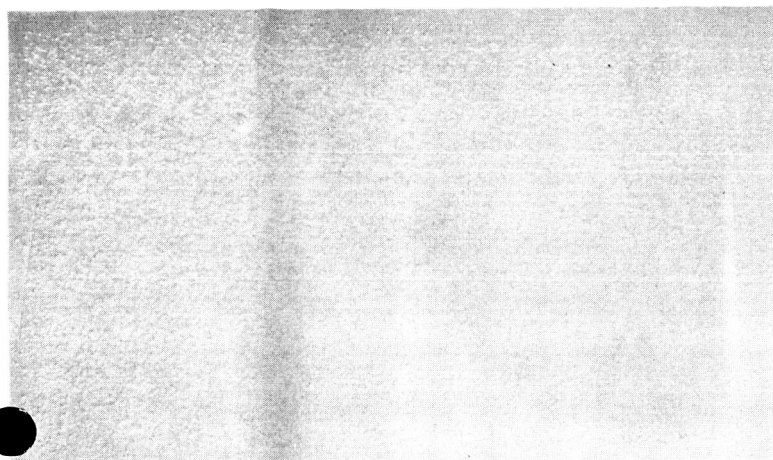
(c) G-4-3 [6.5 psi]
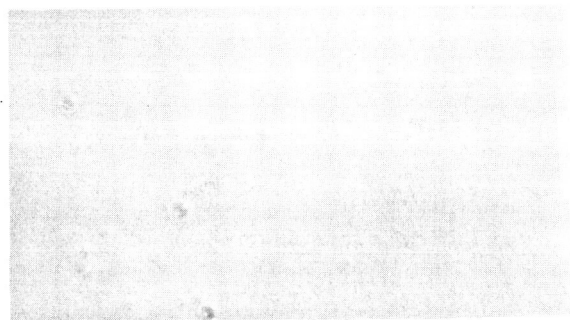
(d) G-7-1 [10 psi]
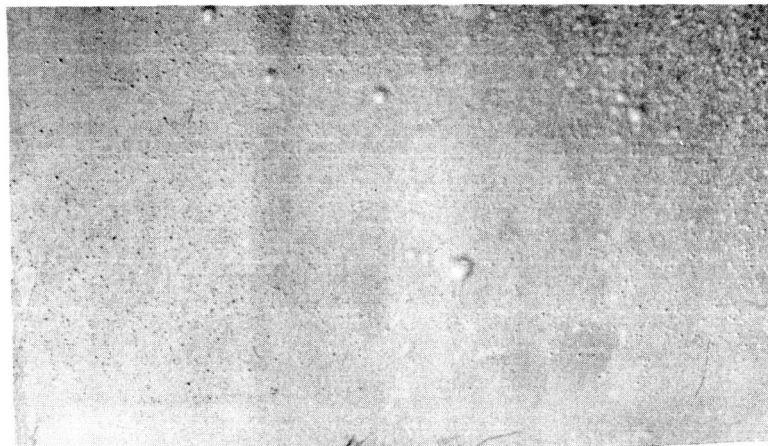
(e) G-7-3 [10 psi]

(f) ST1-10 [2 psi]

Figure 7. Bubble patterns of several
emitters after completion of
the brazing operation (back
pressure of Argon indicated in
brackets).

38
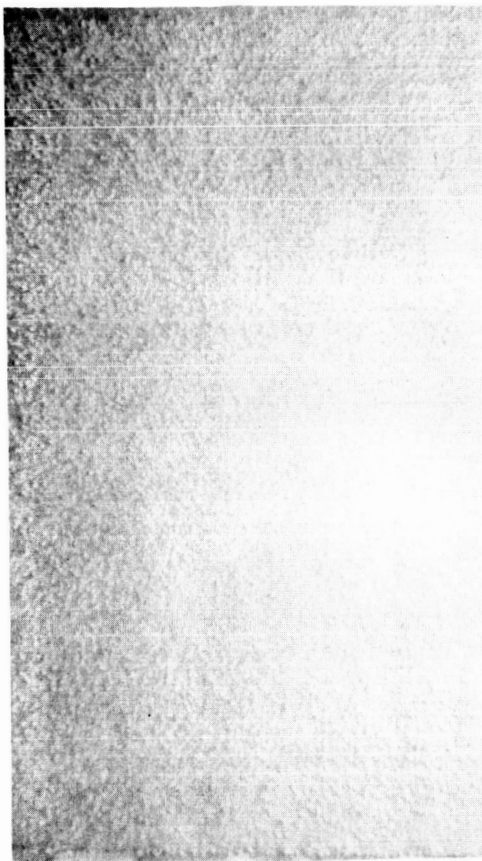
(a) G-6 after braze [3 psi]
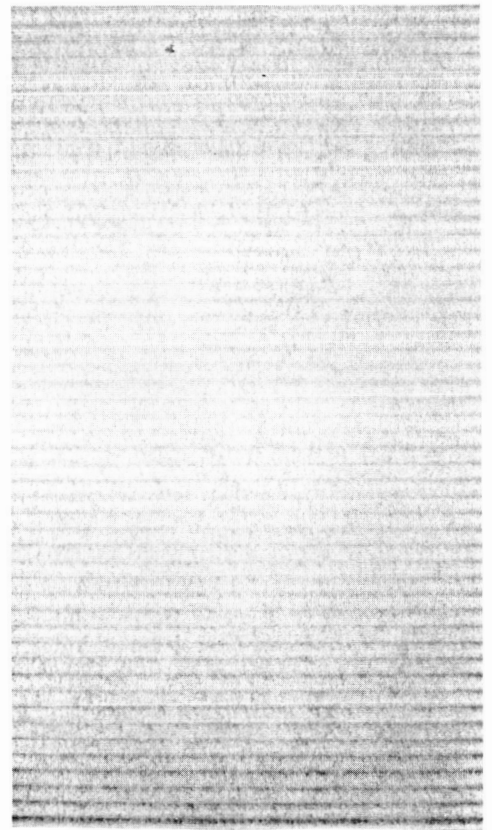
(b) G-6 after elox [1.5 psi]
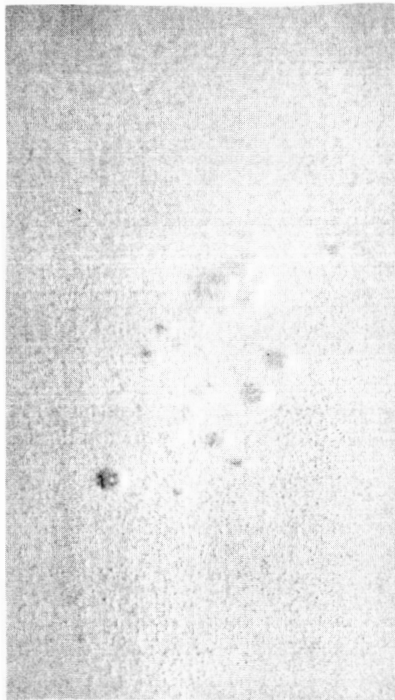
(c) ST1-12 after braze [8 psi]
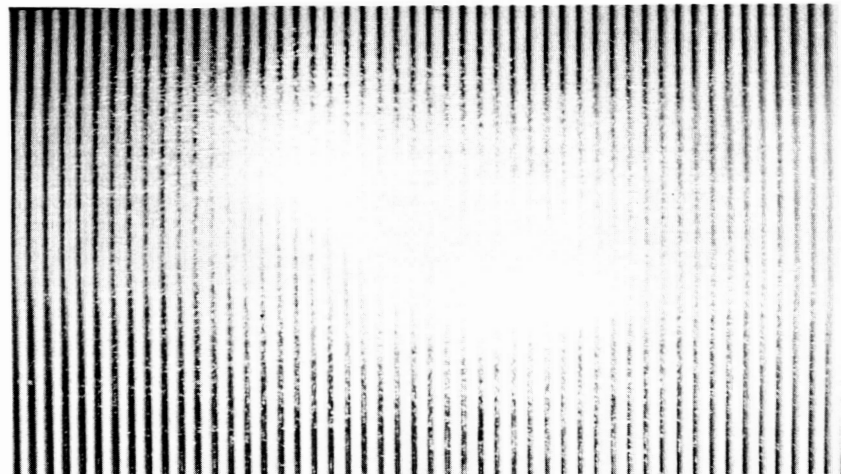
(d) ST1-12 after polish [6 psi]

Figure 8. Comparison of bubble patterns
after braze with that of the
completed emitter (back pressure
of Argon indicated in brackets).

3.4   MICROPHOTOGRAPHY

The dramatic improvement of an emitter surface after electropolishing as compared with the electric discharge machining was illustrated in the photographs of Figures 2 and 3. The difference between a mechanically polished surface and an electropolished surface is illustrated in Figure 9 where both types are illustrated as obtained from a Hughes 324-S material sample. On the general basis of pore distribution one would expect a superior performance from the electropolished surface as an ion emitter.

If this were really the case this electropolished emitter (G-7-3) would outperform any contact ionizer ever tested. This statement is made because this particular mechanically polished sample from which the photo-micrograph of Figure 9(a) was made yielded the best contact ionizer results to date.

Figure 10 shows an enlarged view of the flute contour of ST1-10 which was sectioned immediately after completion of the electric discharge machining operation. The solid flute tips show a rather ragged unevenness. Any ions formed in this region (due to back reflected neutrals) would probably strike the accelerator grid. Electropolishing improves this surface considerably. The seeming roughness and increased porosity in the porous tungsten to a depth of about one thousandth of an inch below the contour surface may be a true representation of the surface condition after E.D.M.; or it may have been caused during polishing of the sample for metallographic inspection. In any event this is the approximate amount of material which is removed during the electropolish operation.

3.5   DISCUSSION OF THE DATA

While permeability uniformity for the spherical tungsten emitters is generally poorer than that of the angular tungsten compacts the G-4 series emitters and the G-7 series emitters are not significantly worse. One could anticipate therefore good overall performance for these particular emitters.

The ST1-10 and ST1-12 uniformity being poor implies that this emitter size is too large for this material. In general it appears that the 1.2" x 2.0" slab size required for the porous material is approaching the upper limit for uniform compacts of spherical tungsten.
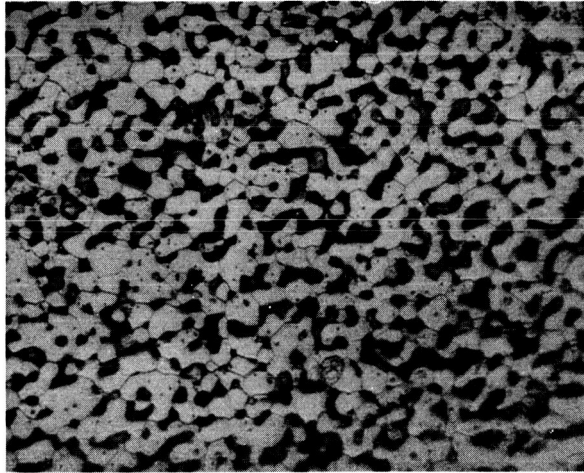
(a) Mechanically polished for metallographic inspection.
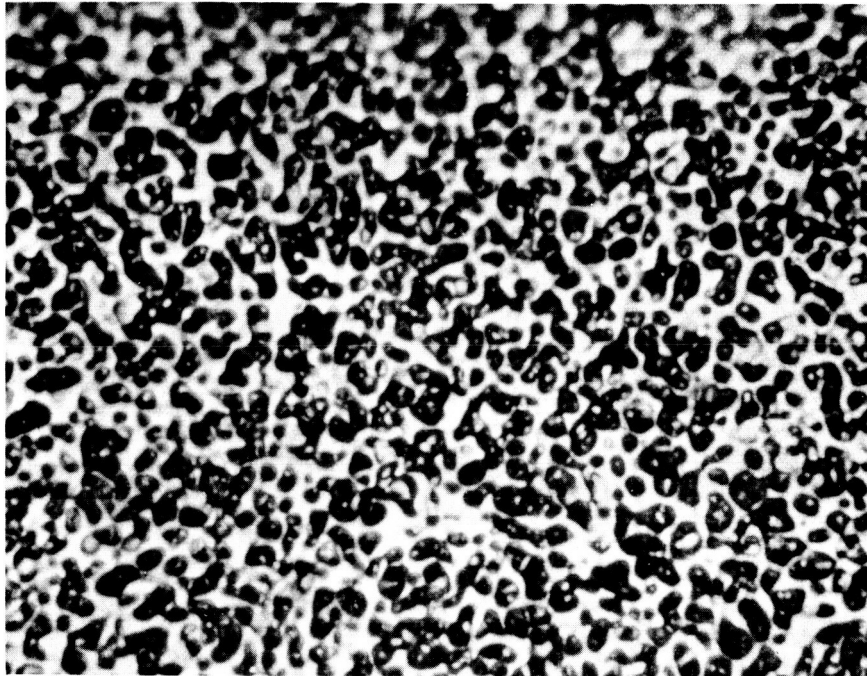
(b) Electropolished

Figure 9. Comparison of micro-structure after
electropolishing with that of metallo-
graphic polish (Hughes 324-S material).

41
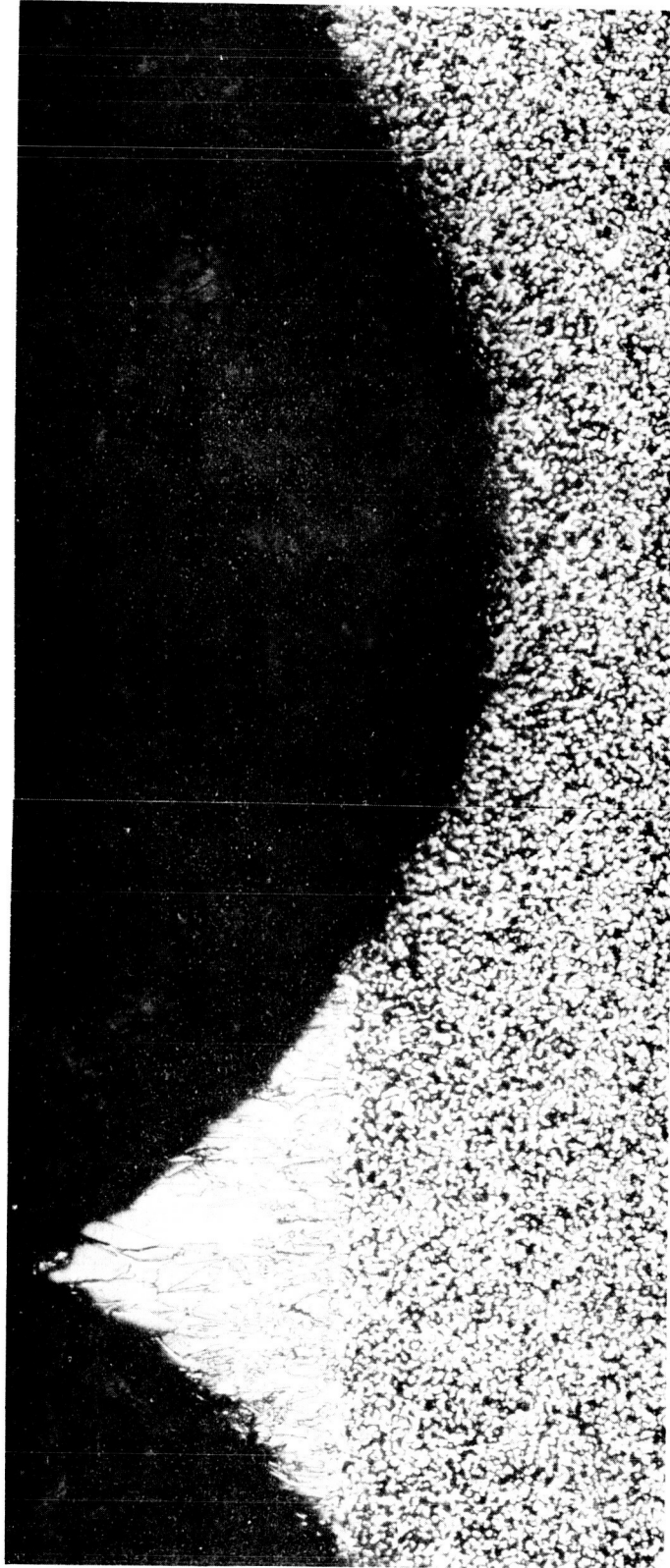
Figure 10. Emitter cross-section and surface structure after contouring by electric discharge machining (ST1-10).

42

4. ENGINE TESTING FACILITY

4.1 VACUUM STATIONS

The ion engine testing facility includes two 4' x 8' stainless steel vacuum chambers each equipped with a cryo-baffled 10 inch NRC diffusion pump. The ultimate vacuum is 7×10^{-8} torr. Each tank is equipped with a quadrupole mass spectrometer for residual gas analysis. Two copper liners and a 4' dia. x .5" thick copper collector plate provide a Faraday cage around the ion beam. The liner nearest the engine is cooled by refrigeration. The other liner and the collector are water cooled. Means are provided for checking input and output temperatures of the cooling fluid. This provides a cross-check upon the power density and distribution of the ion beam.

A view of one station is illustrated in Figure 11. The engine can be viewed at any time through the viewing port shown in the photograph to the right of the operator. A rotary seal provides access to a trap door which can be raised or lowered when viewing is desired. This trap door is a portion of the refrigerated liner.

4.2 VACUUM CONTROL AND INTERLOCK

The tank vacuum is measured continuously by an NRC Company thermo-couple gauge and the diffusion pump baffle is continually cryo-cooled with liquid nitrogen by means of an automatic trap filler. A special safety interlock circuitry designed by TRW Systems removes the high voltage and boiler power in case of a prolonged arc or a permanent short of the accelera-tor grid to either the engine or the grounded frame. In case of vacuum failure the entire power into the engine is removed and the head gate is closed by means of a pneumatic valve. The wiring diagram for this safety interlock is shown in Figure 12.

4.3 ASSOCIATED POWER SUPPLIES AND MEASURING EQUIPMENT

4.3.1 Engine Operation

Each station has sufficient power and measuring equipment to operate two TRW Systems' ion engines continuously at each station. The high voltage supply for Station No. 1 has a maximum voltage capability of 4000 volts at
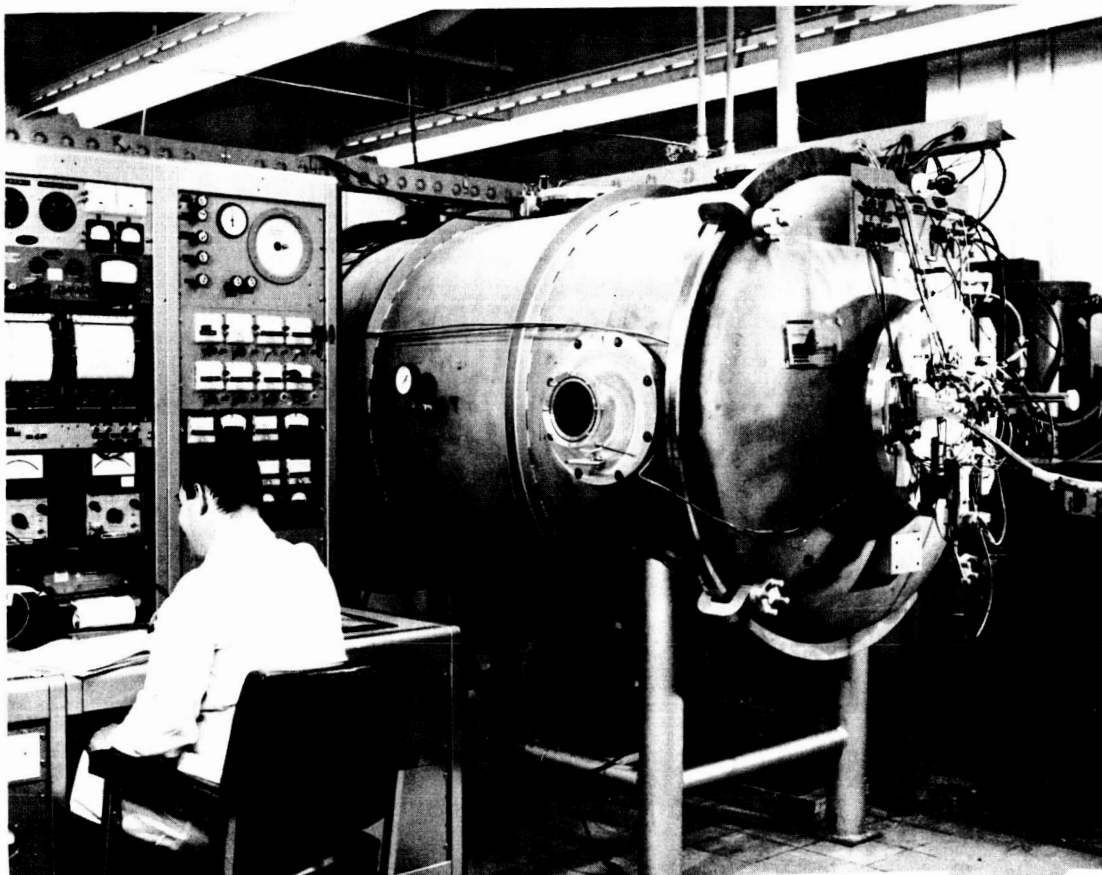
Figure 11.   One of four 4 ft by 8 ft
vacuum tanks.

440 V MAIN   120V AC

01   01

WALL SWITCH

02

S1 DIFFUSION PUMP CONTROL   S2 HEAD-GATE VALVE CONTROL

1 OFF SWITCH
BLACK
4
ON SWITCH
K_{11} RED K_{11}
5   6
5

10 CLOSED SWITCH
BLACK
OPEN SWITCH K_{12}
RED   7

K_{11} K_{11} K_{11}

ON LIGHT   OFF LIGHT

OPEN LIGHT   CLOSED LIGHT

K_{11} RELAY   G   R

K_{12} RELAY   HEAD-GATE SOLENOID VALVE   G   R

DIFFUSION PUMP OVER TEMPERATURE CONTACT
3
02

OVER PRESSURE CONTACT IN N.R.C. IONIZATION GAUGE CONTROL

OUTLET 440V 3φ

DIFFUSION PUMP HEATER

EXTERNAL CONNECTOR

TERMINAL STRIP WIRING GUIDE

IN COMING MAIN 120V 50	01	CONTROL POWER OUTLET STRIP	03	REMOTE INTERLOCK ON - H.V.	22
	02		04		22
K11 RELAY DIFF PUMP POWER	02	THRUST POWER OUTLET STRIP	05	DIFFUSION PUMP H_2O	1
	4		06		2
	5	OUTLET CONTACTS -HIGH VOLTAGE	03	DIFFUSION PUMP OVER TEMPERATURE	3
	6		18		
VACUUM FAILURE ION GAGE CONTROL	5	OUTLET CONTACTS -H.V.	03		
	10		18		
HEAD GATE SOLENOID VALVE	02	REMOTE INTERLOCK ON + H.V.	19		
	7		20		

45-1
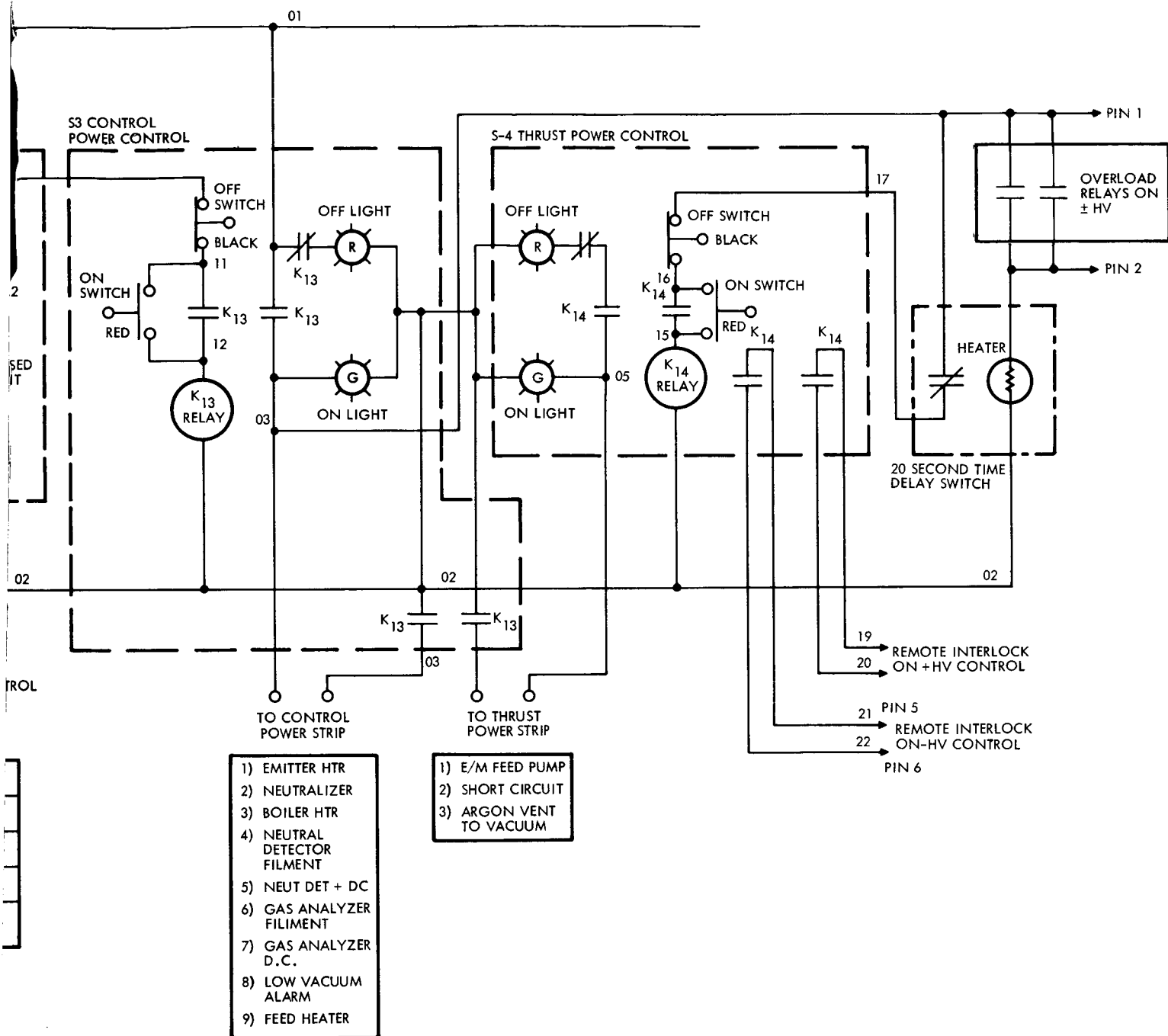
Figure 12. Safety Interlock Circuitry.

40 KVA rating. Station No. 2 has a 5000 volt capability at 10 KVA. Emitter heaters and boiler heaters are Variac controlled and isolation is provided by specially wound and isolated transformer cores. Each station has a bias grid power supply whose output voltage can be continuously adjusted between zero and -600 volts.

Emitter voltage, bias voltage, all heater voltages and currents are measured by means of direct-reading Triplett meters. Source current, beam current and grid drain are measured directly on a specially fabricated and calibrated panel containing redundant multi-range meters. Boiler temperature is obtained by connecting the associated Chromel-Alumel thermocouple outlet to a precalibrated 20 microammeter movement. Emitter temperature can be checked at any time using a Leads and Northrup multivolt potentiometer Model No. 8690 with an isolation cage to prevent accidental electrocution of the operator. Beam current and grid drain are monitored continuously on a 2-channel Varian Strip Chart Recorder.

4.3.2 Neutral Detectors

The neutral cesium detector used for this and previous contracts is illustrated schematically in Figure 13. A pair of collimating apertures define the direction from which neutral cesium atoms will be accepted. The neutral atomic beam, so defined, strikes a tungsten ribbon ionizer operating above the critical temperature. The ions formed are accelerated away from the ionizer by a positive ionizer potential of about 50 volts. The ion current is collected on a nearby plate and is measured by a low current electrometer. A shutter and an ion deflector are placed between the colli-mating apertures. The shutter provides means for monitoring background currents not associated with neutral cesium being measured. The ion de-flector prevents entrance of ions or electrons into the detector.

When used to measure neutral efflux from an ionizer, the detector current is measured under three conditions:

1. Shutter closed (background current)
2. Shutter open — ion accelerating voltages "on"
3. Shutter open — ion accelerating voltages "off".
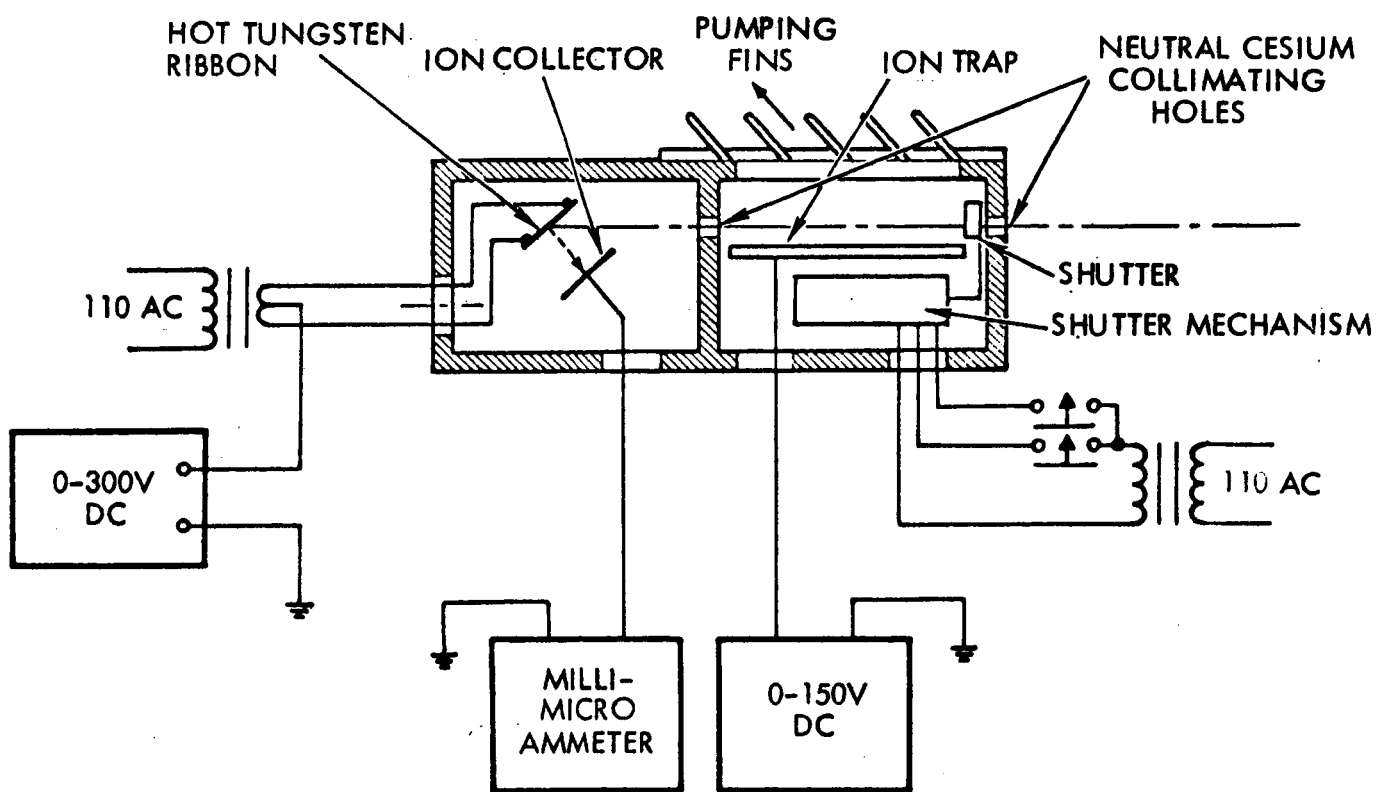
Figure 13. Schematic layout of the neutral cesium detector.

47

The ratio of voltage-on to voltage-off readings corrected for background currents (usually small) is taken to be the fraction, α, of neutral efflux from the thrustor. Several tacit assumptions are made, such as constancy of the angular distribution for neutral efflux, detector linearity, non-interference from the ions, etc. These assumptions are usually valid if reasonable care is taken in the design and placement of the neutral detector.

During the present program two neutral detectors have been employed for testing each ionizer. Each one sees approximately 2 cm^2 of emitter area.

D-C power supplies, shutter control and heater capability is provided for two neutral detectors at each station. Equivalent neutral reading is read directly on Hewlett Packard Model No. 425A D-C Microvolt Ammeters and also monitored continuously on a 2-channel Varian Strip Chart Recorder.

5. ENGINE OPERATIONAL PERFORMANCE

5.1 CORRECTION OF MEASURED NEUTRAL FRACTION DATA AND CORRELATION OF ENGINE AND BUTTON IONIZER MEASUREMENTS

As first pointed out on Page 86 of Ref. 3 measured neutral efflux must be corrected for a backscattering factor, G when the accelerating grid in any way impedes the molecular flow of neutral efflux. This fact has been overlooked by many workers in the field and hence bears repeating here.

Beam "on" measurements do not measure backscattered neutrals due to the fact that these are ionized upon striking the emitter surface; during beam "off" measurements, however the ionizer no longer acts as a sink. While the ratio of "on" to "off" neutral measurements does measure the operating propellant utilization this neutral density can be significantly less than in the accel region where improperly focused (and hence grid eroding) charge exchange ions are formed in direct proportion to the neutral density.

The measured neutral fraction α_m, the "true" neutral fraction emerging from the emitter, α, and the neutral fraction, α_a, in the accelerated region are related as follows:

$$\alpha_m = \alpha \frac{(1 - G)}{(1 - \alpha G)} \tag{1}$$

$$\alpha_a = \alpha \frac{(1 + G)}{(1 - \alpha G)} \tag{2}$$

$$\frac{\alpha_a}{\alpha_m} = \frac{1 + G}{1 - G} \tag{3}$$

For a parallel slit geometry such as the TRW Systems' ion engine G can be calculated approximately from the expression

$$G = W/W_f + (1 - W/W_f)(1 - K) \tag{4}$$

49

where
$$W = \text{width of a grid bar}$$
$$W_f = \text{spacing between adjacent ionizer flutes}$$

and
$$K = \text{Clausing's factor[5] for tubes of rectangular cross section.}$$

For the TRW Systems' engine G = .7. The relationship between α and α_m for this value of G is plotted in Figure 14. In comparing engine data with that of button ionizer data of Shelton, Hall and Cho the corrected α will be used rather than α_m.

Button data needs no correction for reflection since the accelerating electrode is actually behind the ionizer. Some of the button data presented herein will be labeled "neutral fraction at 20° to normal." This qualification is made because of a recently discovered forward peak in the neutral efflux which implies that measurements of neutral fraction at 20° are a factor of 2 too high for charge exchange calculations.

Neutral detectors for the engine measurements are off axis 30° and would therefore be a factor of 1.5 too high according to the same integrated distribution. However, the additional focusing action of the emitter contours probably adds a sufficient increment in the forward direction that the distributional correction factors for either engine or button data are about the same.

The engine emitter performance will therefore be referred to as duplicating the button ionizer data when α as determined from the measured neutral fraction α_m using either equation (1) or Figure 15, duplicates the "20°" button measurements.

The button measurements for clean polished Hughes' 324S material (which also represents the best published contact ionizer efficiency to date) can be used as an illustration. This data is plotted in Figure 15. The button data of .28% at 1400°K for a current density of 20 ma/cm^2 would be duplicated by engine tests if the neutrals at the same temperature and current density measured .085% in an oxygen free environment.

50
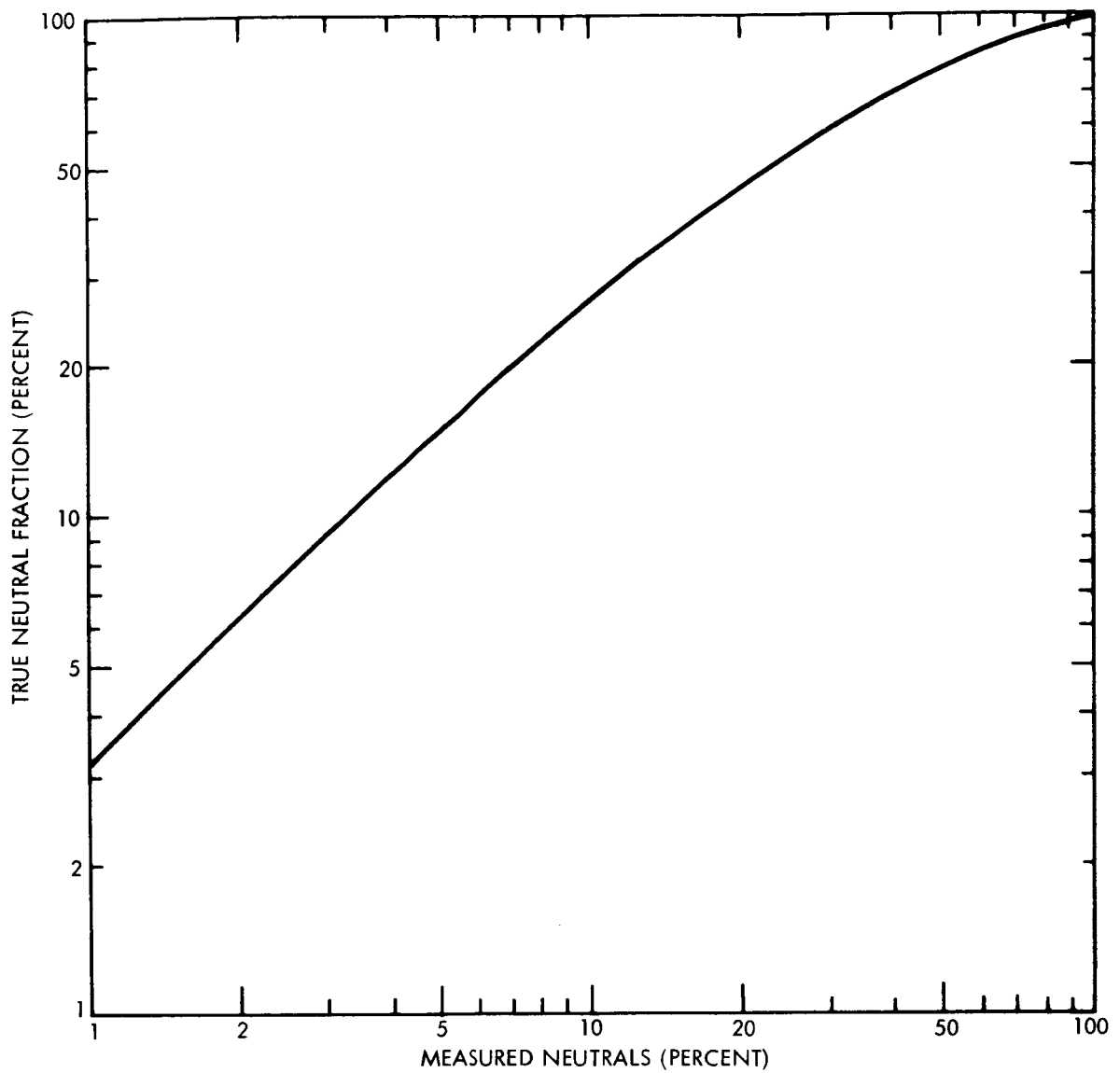
Figure 14. Plot of the true versus measured neutral fraction for the TRW Systems' engine design.
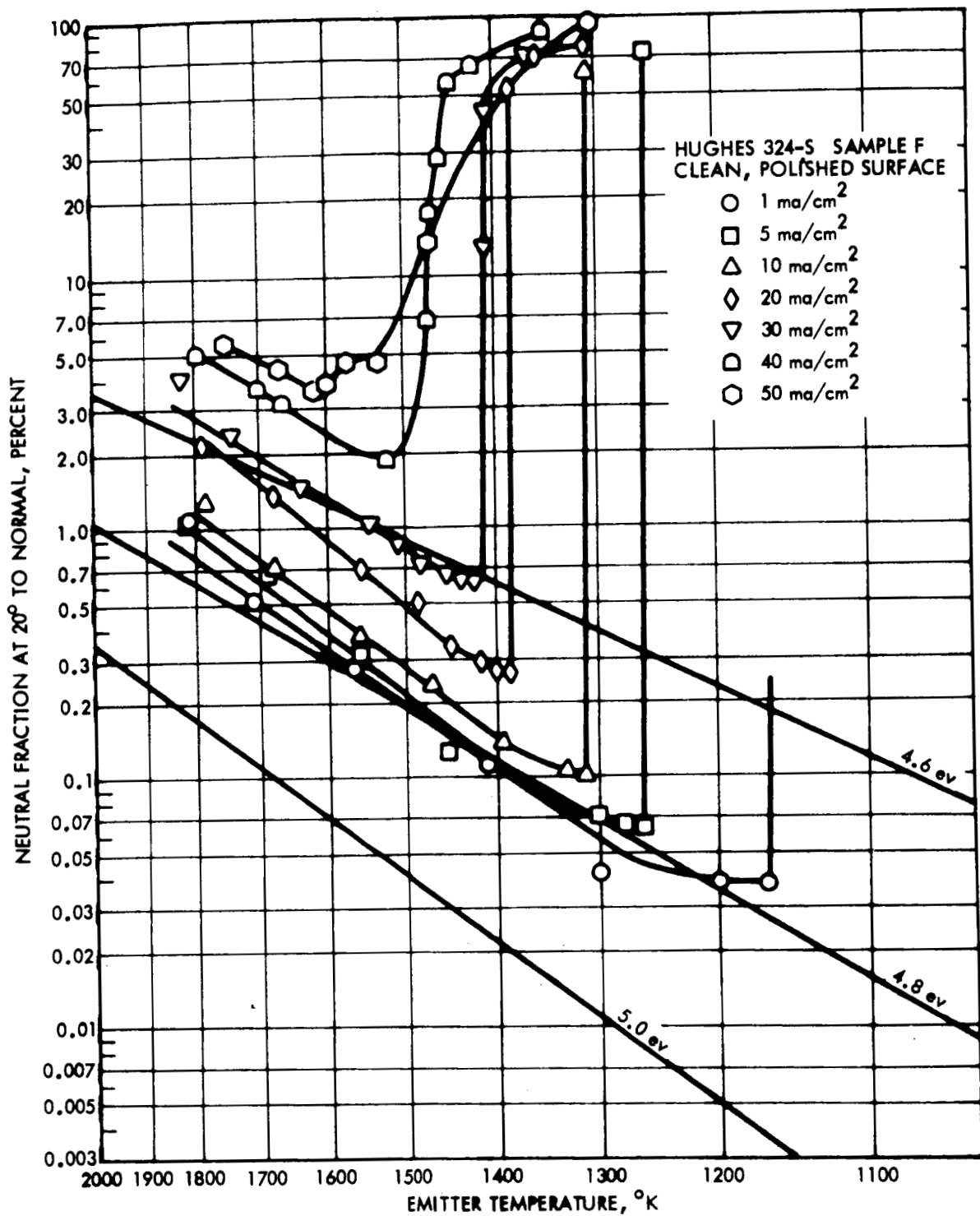
Figure 15. Button test of clean polished
Hughes 324-S material: α vs T
for various current densities.

The indicated work function lines in Figure 15 are used for all α vs T plots recorded here. These are calculated from the Saha-Langmuir equation.

At current densities below a certain level (usually 5 ma/cm) the neutral fraction levels off at a value which is characteristic of the substrate material[7]. This leveling off value when corrected for backscattering, can be used in the Saha-Langmuir equation to determine the work function.

While there is some argument as to whether this calculated work function is actually the work function of the substrate (i.e. the accepted tungsten work function is 4.62 eV for polycrystalline material and the value for porous tungsten is calculated from the Saha-Langmuir equation using the "leveling off" neutral fraction is closer to 4.8 eV, it has been found by Shelton and Cho[7] to be the same for most uncontaminated ionizers.

Thus the data of Figure 15 indicates a substrate work function of nearly 4.8 volts for Hughes 324S material.

In designating substrate work function to engine data, care is taken to use a lower than average current density since the "leveling off" implies that neutral fraction is no longer dependent upon pore distribution. A rise in neutral fraction with emitter temperature is a good indication that the substrate characteristic is the determining factor -- not the pore distribution.

5.2   THE EMITTER CONTAMINATION PROBLEM

Until recently the measured neutrals from the large ionizers has been considerably higher than that from comparable button data.

The seriousness of this problem during last year's program is illustrated by comparing the button data for G-4 material in Figure 16 with emitter G-4-1 performance data of Figure 17. Remembering that the measured neutrals of engine data must be multiplied by 3 to be compared with the button measurements we see that even at temperatures 200° above the normal critical temperatures (for the button) the equivalent neutrals from the engine are almost an order of magnitude higher.
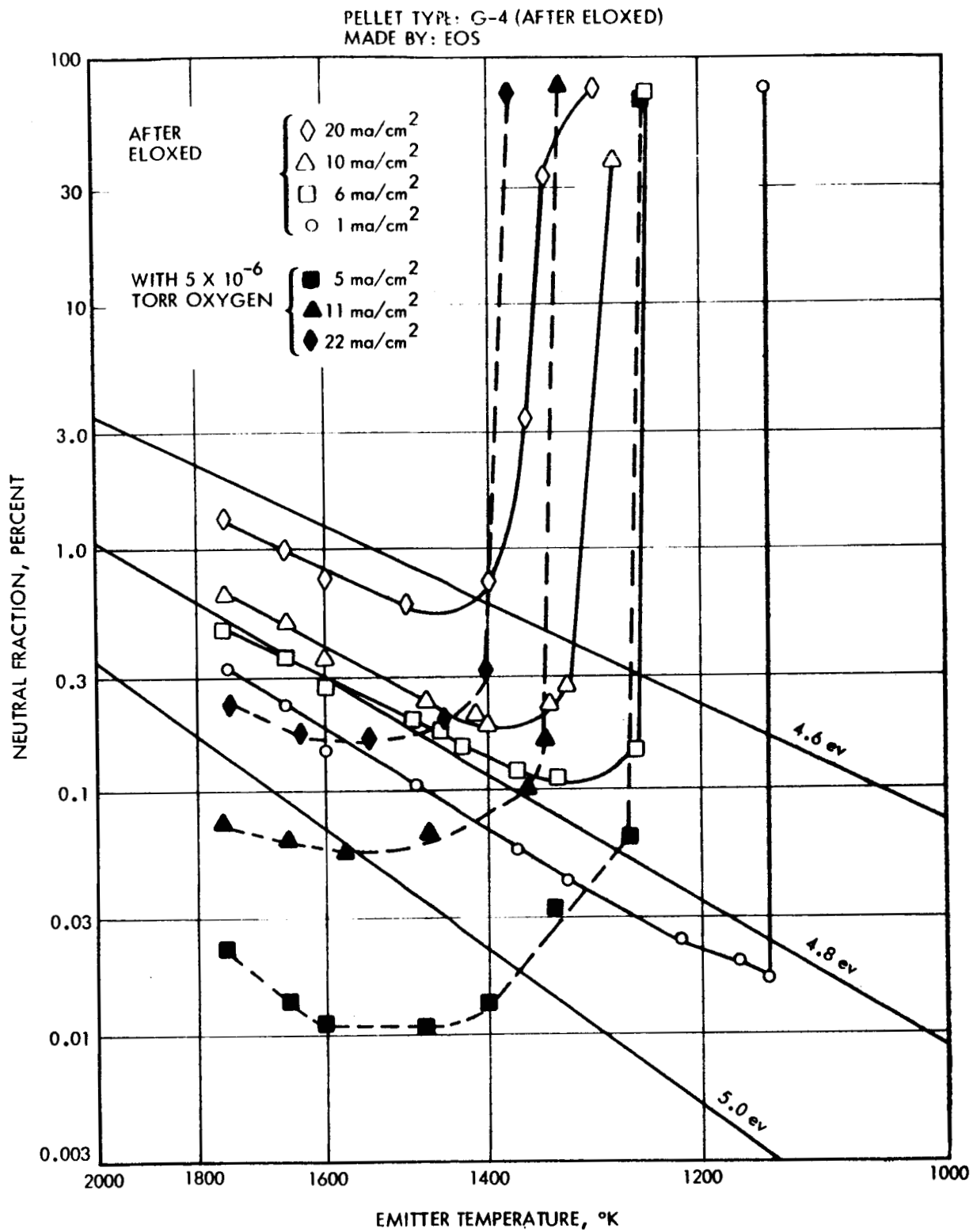
Figure 16. Button test of G-4 material after
electric discharge machining.
α vs T at various ion current densities.
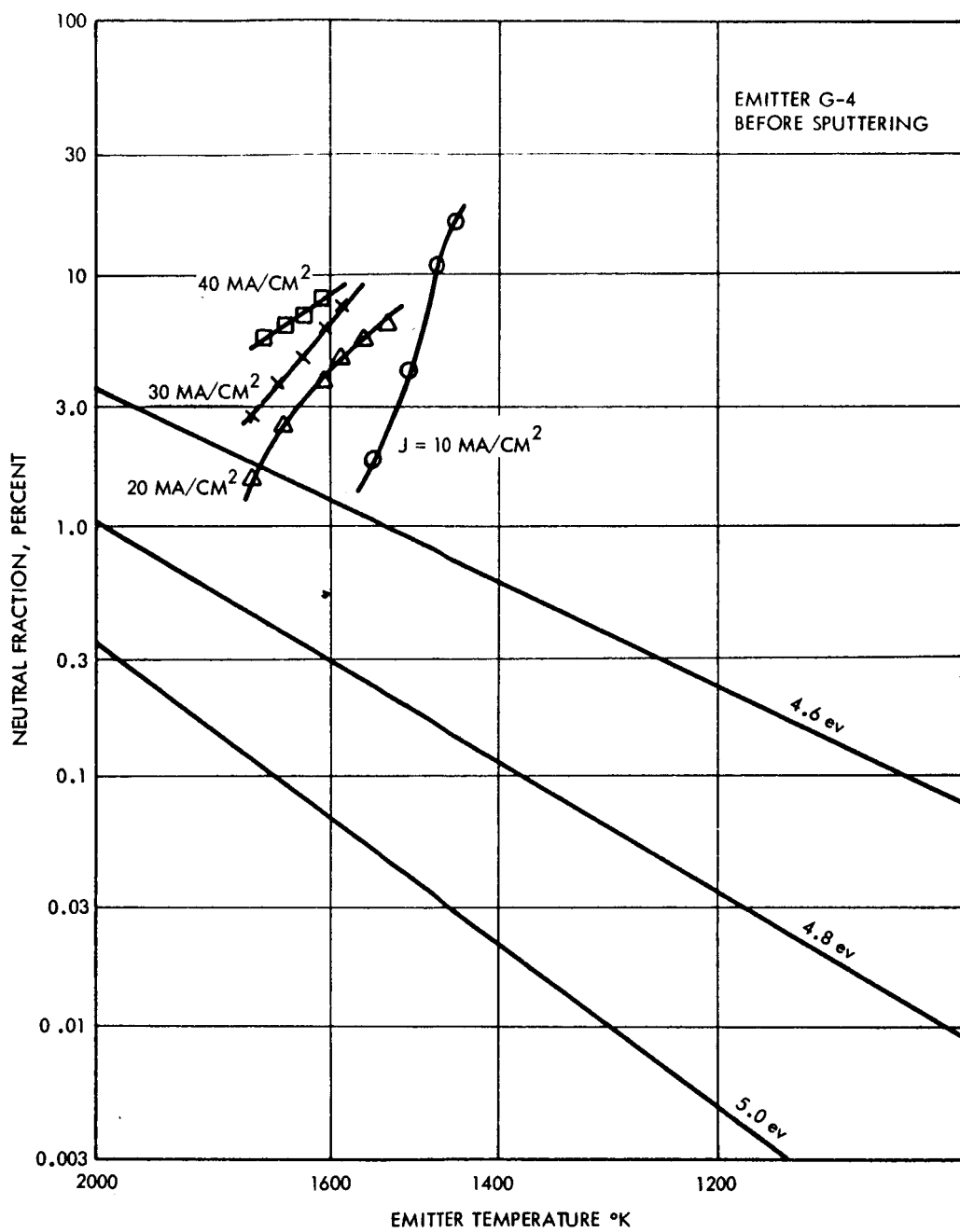
Figure 17. Engine test of Emitter G-4
α_m vs T at various ion current
densities.

55

It is now known that this large difference in performance was due to a combination of poor surface microstructure and a "remnant-oxygen" condition.

Our ability to verify this conclusion is largely due to our present capability of introducing either an oxydizing or reducing atmosphere during actual engine operation without at the same time carbiding the emitter or contaminating it with such material as molybdenum (see engine design changes of Section 2.3).

This "remnant-oxygen" condition which is characterized by high poorly defined critical temperatures apparently requires prior operation in an oxygen or water vapor environment. If this oxygen level is sufficiently high, the emitter data matches or even improves upon the button performance.

Figure 18 illustrates the similarity of the "oxygenated" data obtained at 10 ma/cm^2. Curve (1) represents G-6(b) emitter data* in 8 x 10^{-6} torr O_2 while Curve (4) was obtained from button measurements of the same material in 5 x 10^{-6} torr O_2.

Shortly after the O_2 removal the α vs T characteristic of the emitter became that of Curve (2). This high neutral — high critical temperature characteristic is quite stable for long periods of operating time in a good vacuum and is representative of a "remnant-oxygen" condition.

However, after 15 to 30 minutes of reducing atmosphere of acetylene at 5 - 9 x 10^{-9} torr the "clean" tungsten characteristic of Curve (3) is obtained. This condition too is stable for long periods of time in an oxygen (or water vapor) free environment.

Figure 19 shows the α_m vs T characteristics in the "oxygenated", "remnant-oxygen" and "clean" tungsten condition for emitter G-6(b) at 5 ma/cm^2. Any one of these curves could be repeated at any time by the appropriate sequence of oxygen or acetylene addition.

* Taken before sputtering of the surface in an ion beam.
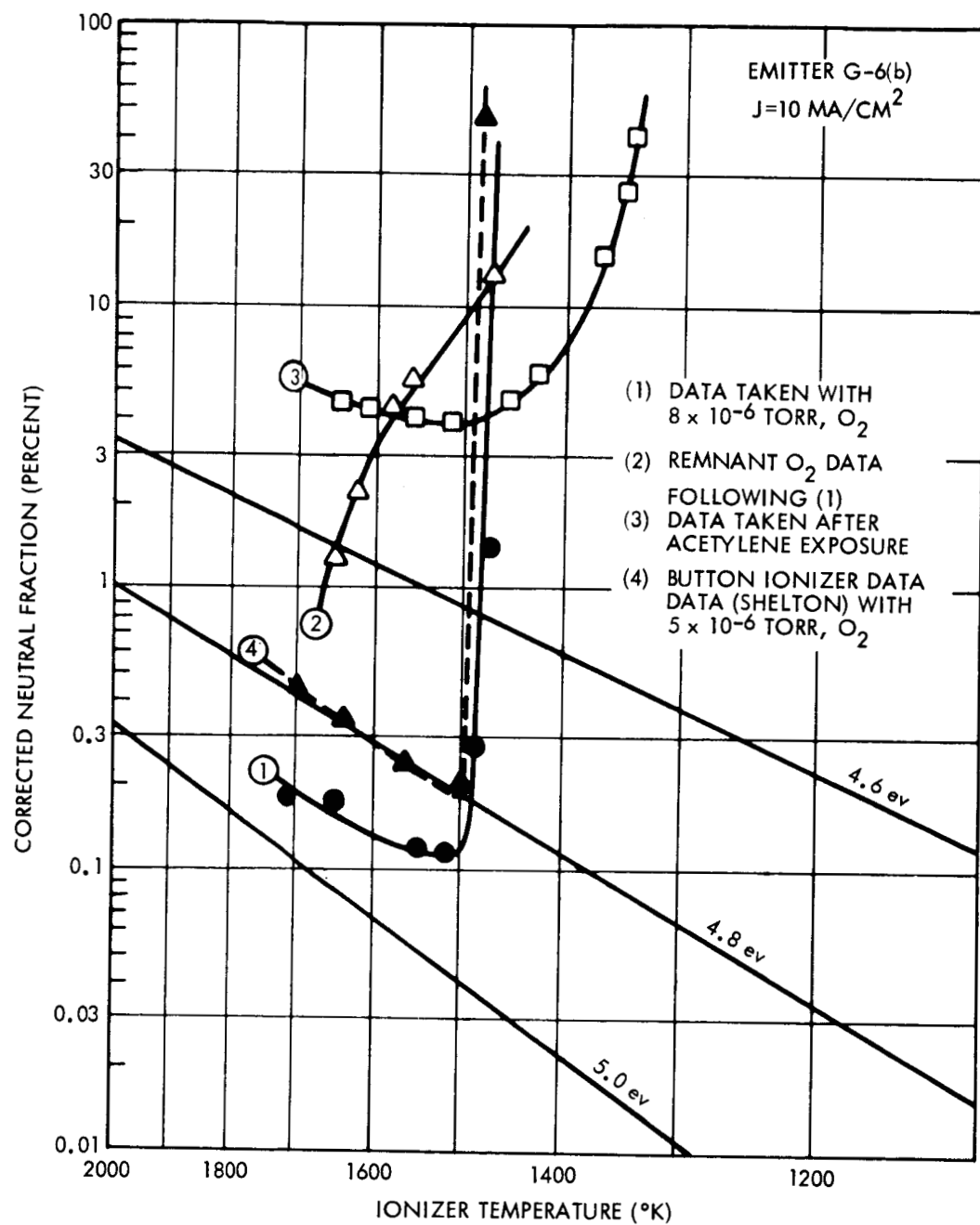
Figure 18. Evidence of remnant-oxygen con-
ditions — its generation and removal
by means of the oxygen-acetylene cycle.
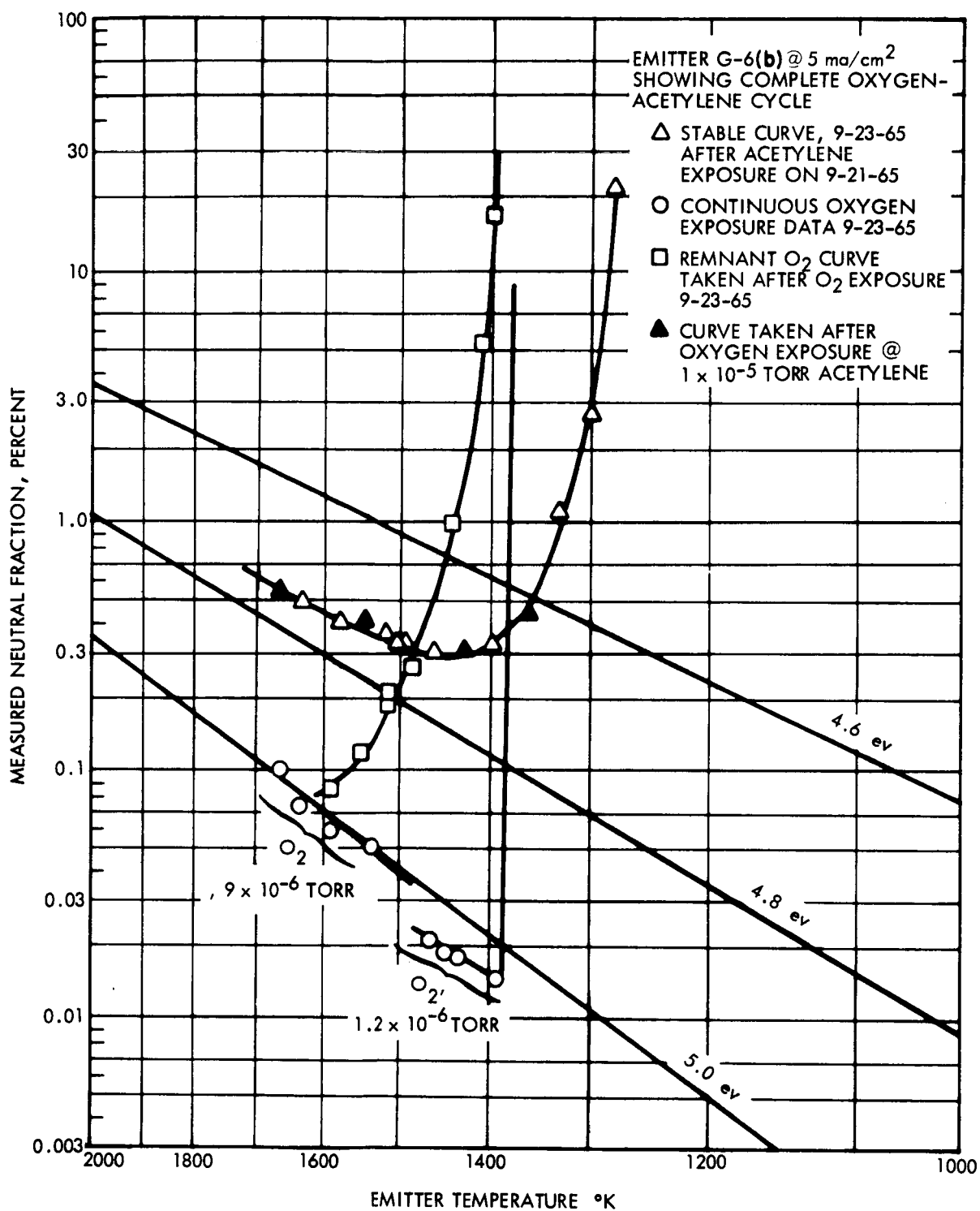
Figure 19. Measured neutral fraction vs
temperature at 5 ma/cm^2. Data
shows complete oxygen–acetylene
cycle.

58

Figure 20 shows α vs T curves at 5, 10 and 15 ma/cm^2 for this same emitter measured during or shortly after acetylene exposure, i.e. with the emitter in the "clean" tungsten condition. Particular attention is drawn to the 10 ma/cm^2 curve. The same characteristic curve was obtained before and after 24 hours of continuous operation at 15 ma/cm^2 without further acetylene exposure. It was found later that a tank vacuum which included water vapor at as low a level as 1 x 10^{-7} torr (as measured by the gas analyzer) would cause eventual conversion of the emitter ionizer characteristic to the "remnant-oxygen" condition.

5.3   THE EFFECT OF IMPROVED SURFACE MICROSTRUCTURE

The curves of Figures 18, 19, and 20 were taken with G-6(b) in the as-eloxed* condition. It was noted that at ion current densities of 10 and 15 ma/cm^2 the "clean" tungsten curves measured a neutral minimum about 3 times greater than that of the equivalent button data while at 5 ma/cm^2 there was almost a 1/1 correspondence.

As discussed in Section 5.1, the low current density measurements are indicative of the surface work function while the high current density characteristics are more sensitive to the pore distribution. The close match at 5 ma/cm^2 in contrast with the large discrepancy at 10 and 15 ma/cm^2 was considered good evidence that G-6(b) was subject to pore clogging rather than a low work function surface.

Subsequently this emitter was sputtered in an ion beam until from 75 to 100 micro-inches of the surface had been removed. When re-installed as an ion engine it was found that while the 5 ma/cm^2 "clean" curve was only slightly improved by this operation the 10 and 15 ma/cm^2 curves were improved by almost a factor of 3. Before and after sputtering characteristics are illustrated in Figure 21. This improved emitter data was now equivalent to or actually superior to the button data** as is illustrated in Figure 22.

---

* As contoured by electric discharge machining and prior to either sputtering or electropolishing.

** Button measurements were made from two samples taken from the same slab from which G-6(b) was fabricated.
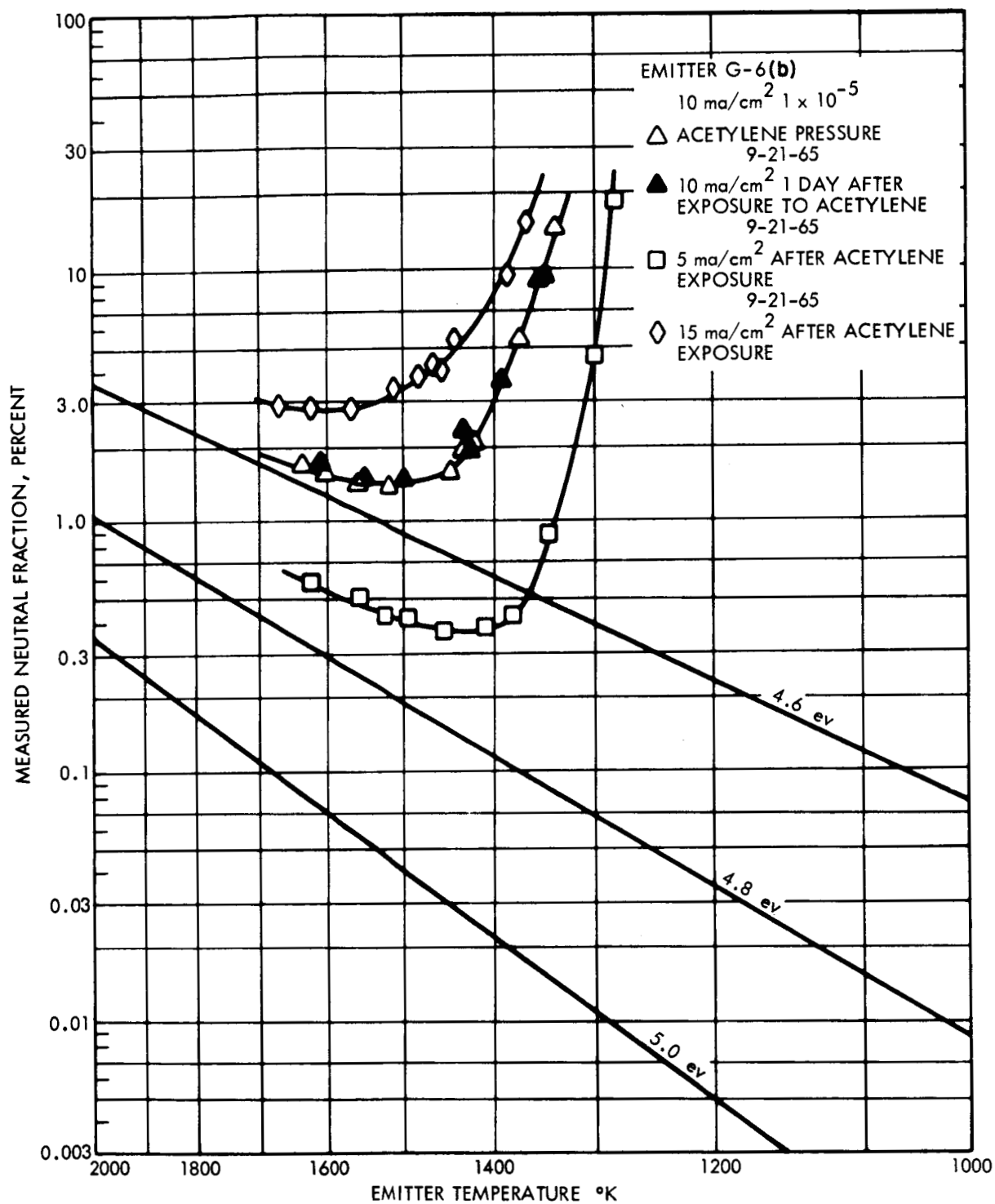
Figure 20. Measured neutral fraction
vs temperature for emitter G-6(b)
after acetylene exposure. Data
taken at 5, 10, and 15 ma/cm^2.

60
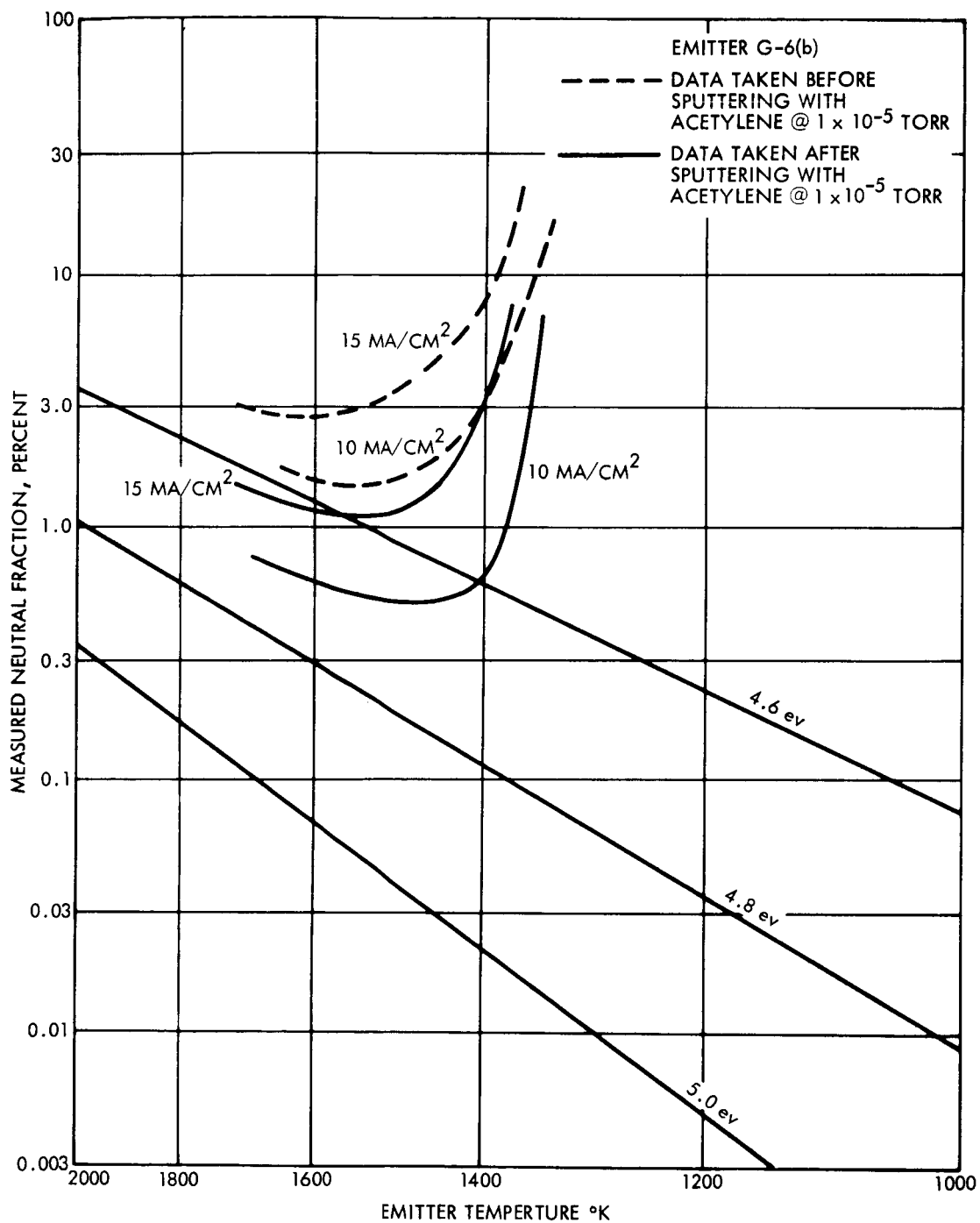
Figure 21.   Measured neutral fraction vs temperature at 10 and 20 ma/cm^2 before and after G-6(b) was sputtered.
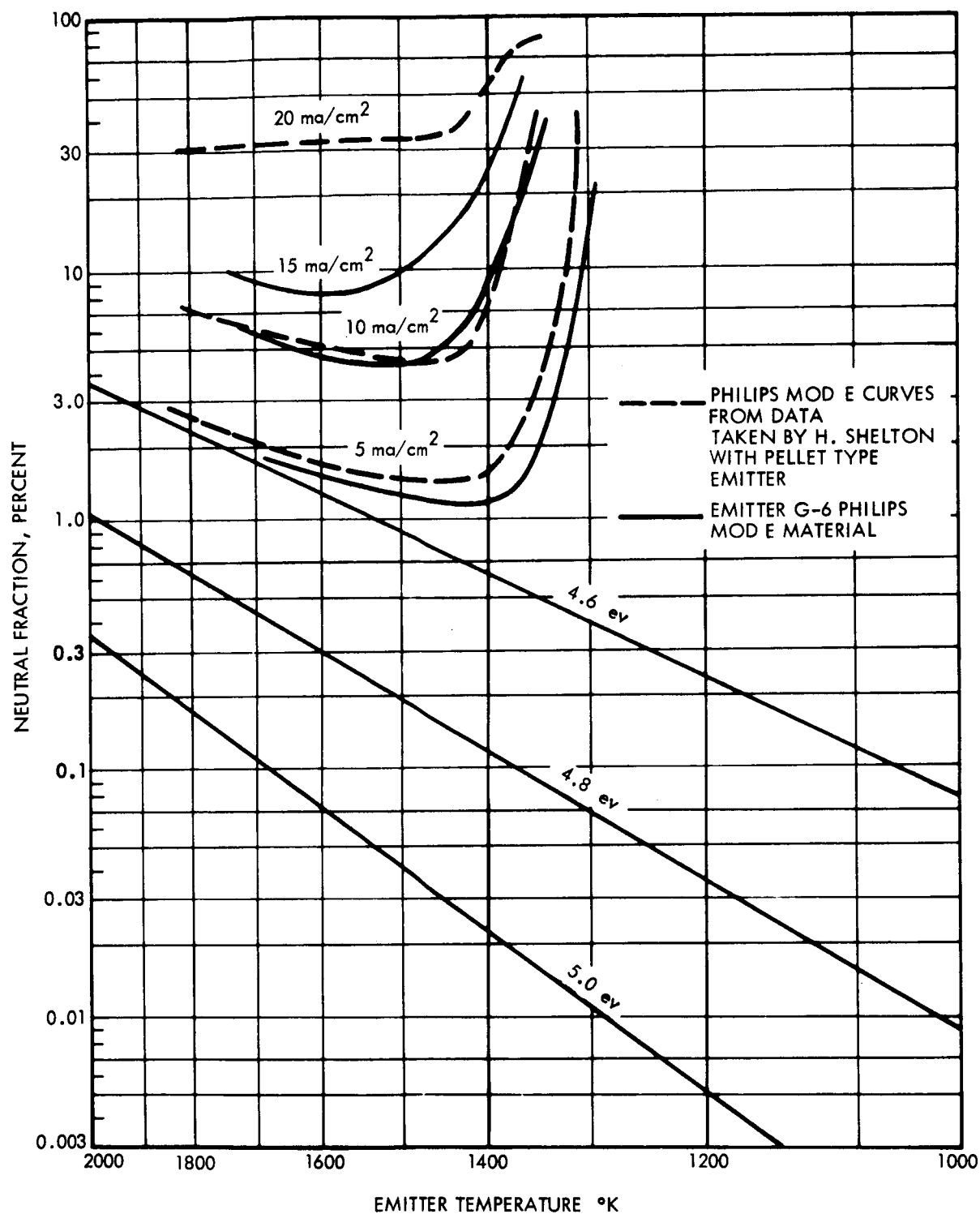
Figure 22. Emitter G-6(b) data, after sputtering (and acetylene exposure) is compared with button data at various current densities.

While the "oxygenated" tungsten characteristic from button data had been previously duplicated in engine tests many times this was the first time that good correlation was obtained at high current densities for the "clean" tungsten condition. Consequently not only was the contamination problem now resolved but at the same time we were finally able to prove that the small button sample performance could be duplicated in a large high perveance thrustor.

5.4 OPERATIONAL CHARACTERISTICS OF 4 EMITTERS

Emitter G-6(b)

The "after-acetylene" curves of Figure 22 are considered to be the true operational or "clean" tungsten characteristics of emitter G-6(b). All of our experience to date indicates that this is indeed a stable situation if the vacuum and cesium are free of oxygen or water vapor.

Emitter G-4-2

The characteristic of emitter G-4-2 were measured after the completion of the first life test. This data is shown in Figure 23. While good results were obtained at 10 ma/cm^2 the high critical temperature at 15 ma/cm^2 even in the presence of oxygen implied wide variations in permeability over the emitter surface. However this data was taken before the experimental arrangement for careful addition of acetylene had been completed. Hence the "evidence" is inclusive.

Emitter G-4-3

The characteristics of G-4-3 after sputtering in an ion beam and preliminary reduction of surface oxides with acetylene yielded the (corrected) α vs T curve of Figure 24 which also includes button data at 11 and 22 ma/cm^2. Although the engine performance is slightly inferior to the button ionizer this is considered excellent correlation. In comparison with the G-4-1 data of Figure 17, the improvement in performance is quite dramatic. Figure 24 represents the lowest reproducible neutral fraction operation which has been achieved with our high perveance ionizers to the present time.
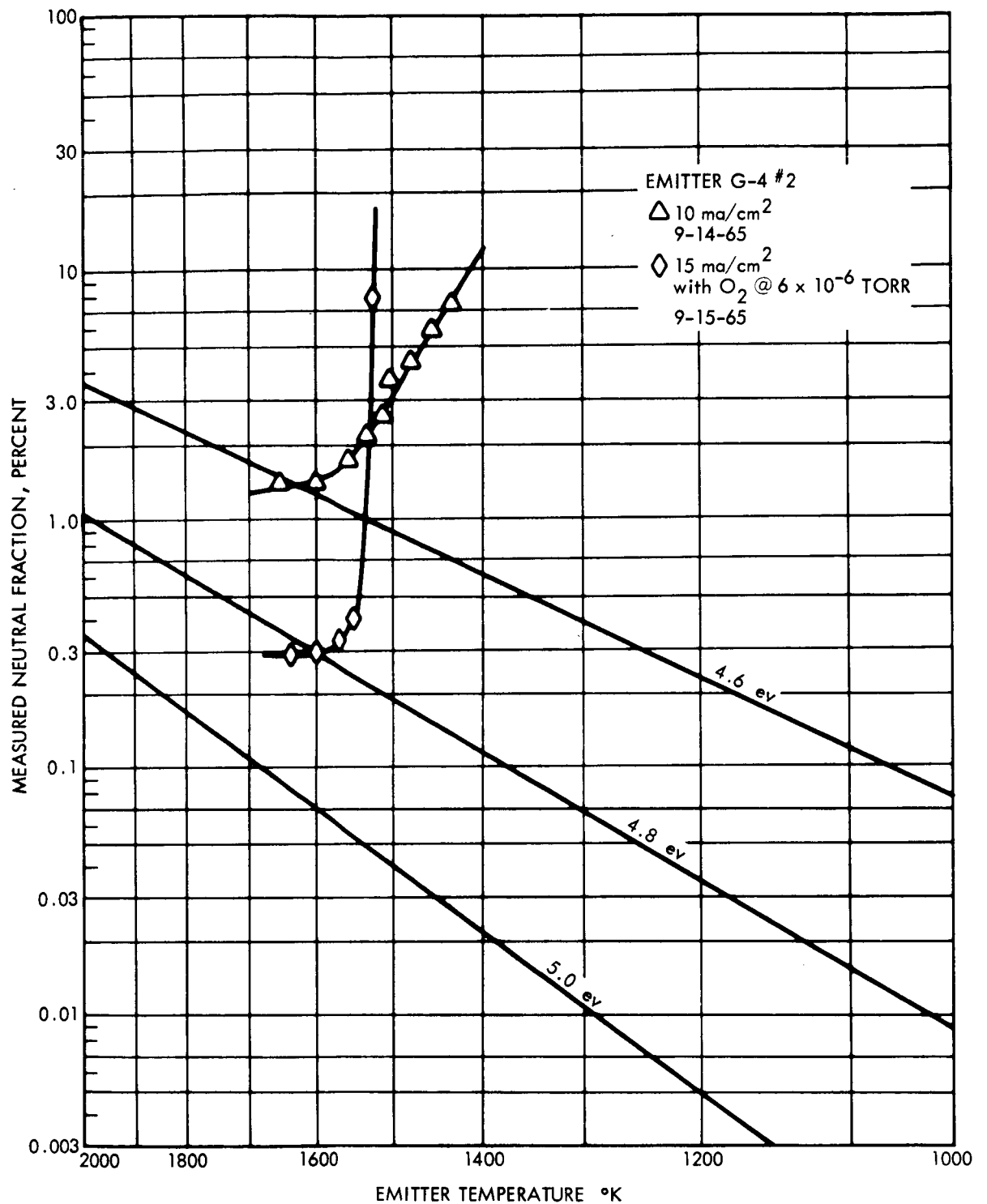
Figure 23. α_m vs T data for emitter G-4-2.
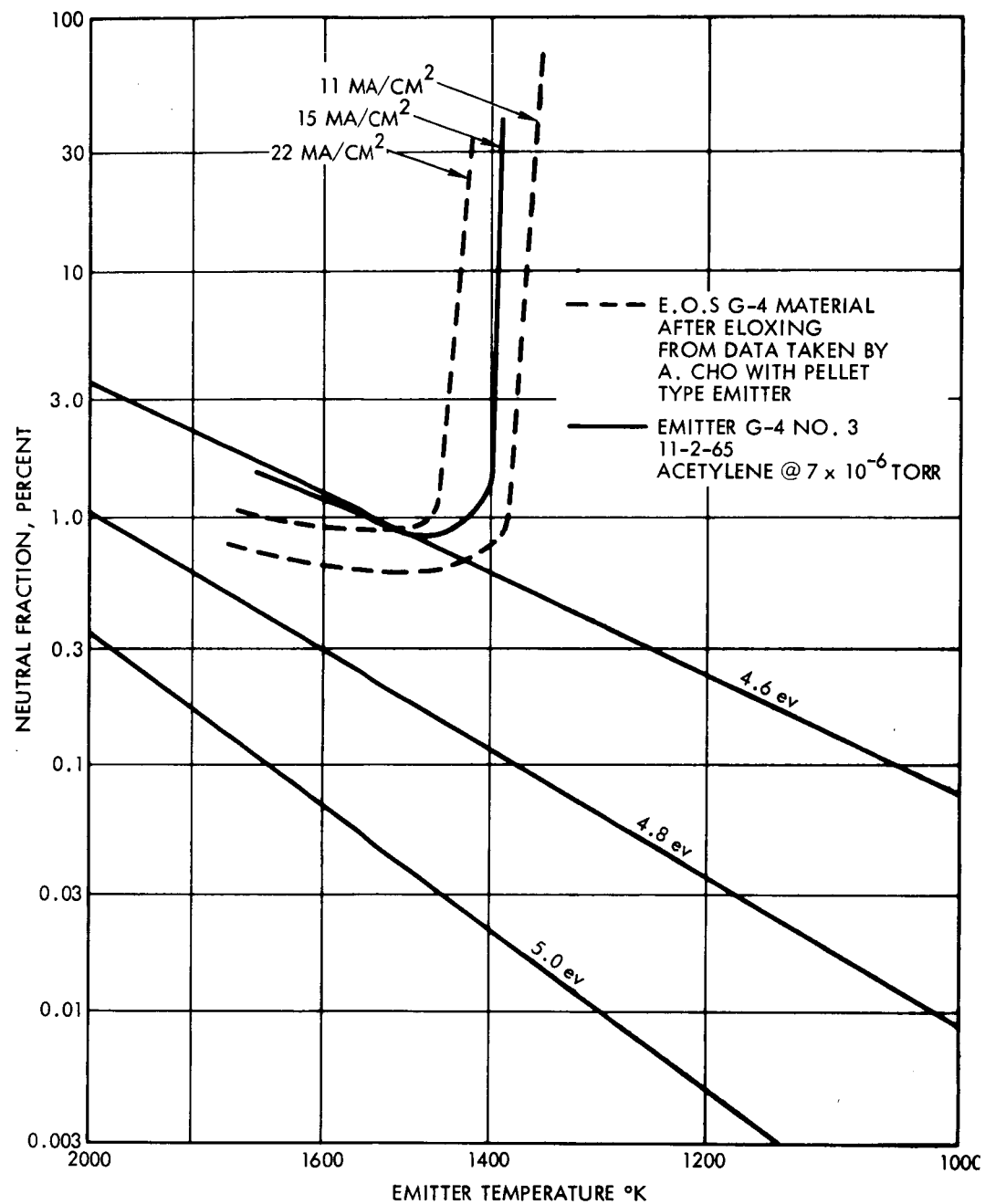
Figure 24. α vs T data for emitter G-4-3 at 11 and 22 ma/cm². Data from H. Shelton's and A. Cho's tests with G-4 material is included for comparison.

65

Emitter G-6

The initial tests of emitter G-6 which had been both sputtered and
electropolished following the E.D.M. contouring showed a strong "remnant-
oxygen" condition when first put into operation. This is not too surprising
since the vacuum at start-up was 1.4×10^{-5} torr with a high indicated water
vapor peak. The emitter was then subjected to 30 minutes of acetylene at
1.5×10^{-5} torr before a "clean" characteristic could be obtained. The
"before" and "after" characteristics are plotted in Figure 25. The "clean"
condition matches that of G-6(b). During the first 200 hours of operation
G-6 neutral fraction at 1500 to 1550°K gradually decreased to a low of .7%*
and averaged between .7 and 1.1% at this current density. Addition of ace-
tylene lowered the neutrals even further (.35%) but this was only temporary.

After the first boiler refill, however, G-6 neutral fraction increased
to the 2 to 4% (measured) level and could only be reduced temporarily by the
addition of acetylene. (For further details see Section 7.7).

5.5   THEORY OF THE "REMNANT-OXYGEN" EFFECT

Shelton et al[8] in measuring the influence and evaporative lifetimes
of various materials which were sputtered onto an emitter found that those
materials such as beryllium, chromium, titanium, niobium and tantalum were
particularly bad "poisons" in that they led to a severe "remnant-oxygen"
condition. Since these elements form refractory type oxides they cannot be
removed by high temperature firing — one method of emitter clean-up often
employed by Shelton. This leaves the surface with a partial oxygen coverage.
The adsorption energy of cesium is increased by the presence of these oxide
sites so that the cesium coverage in this area becomes excessive — lowering
the work function and raising the neutral fraction.

The effective area of each site shrinks with rising temperature causing
a gradual decrease in neutral fraction. The normal sharp critical temperature
characteristics is lacking.

*   Measured.

66
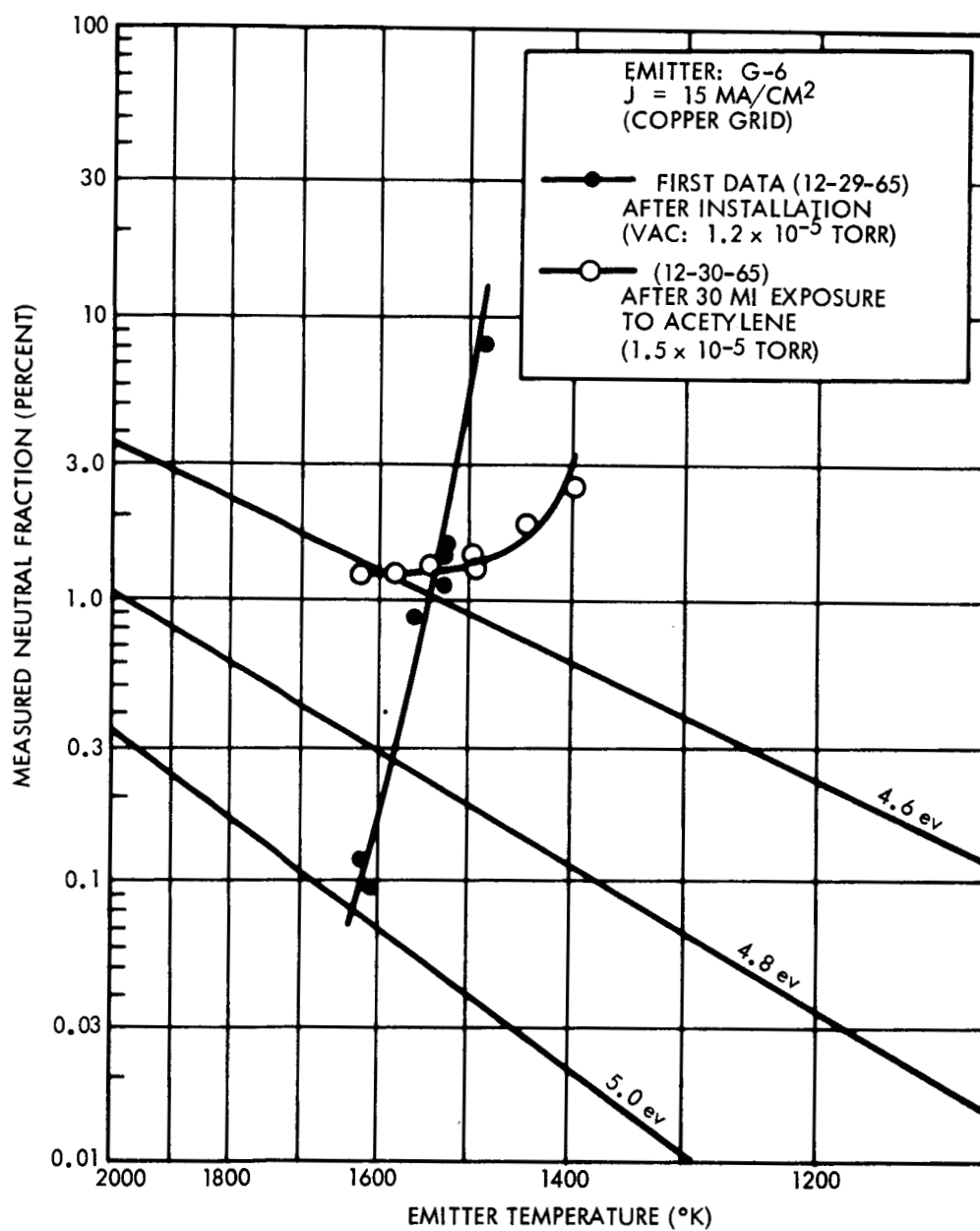
Figure 25. First α_m vs T measurements of emitter G-6 — using a copper grid.

The requirements for the remnant-oxygen condition are therefore:
(1) the presence of such material as Ti, Cr, Ta etc., on the surface and
(2) operation in a water vapor or O_2 environment for a sufficient length of time that oxidation of impurities on the surface is complete.

5.6 SOURCES OF CONTAMINATION

The removal of a colloidal substance from the plenum chamber of emitter G-6 after the contouring operating by E.D.M. (as discussed in Section 2.1.2) leads to the reasonable conclusion that this was the major source of emitter contamination. The elements chromium and titanium were identified in the analysis of the foreign matter.

Unfortunately final proof is lacking. Although several emitters were fabricated after this process had been corrected none were adequately tested (prior to the termination of this program). Emitter G-3-2, which had been plastic infiltrated prior to the E.D.M. operation was put into operation briefly. Initial neutral fraction measured .1% at about 1500°K and 15 ma/cm^2 density (after acetylene). A complete set of data had been planned for the following day. However, during the night a serious side leak developed and the test was terminated.

6. ACCELERATOR MATERIAL COMPATIBILITY AND FEASIBILITY STUDY

6.1 COPPER

Until recently copper was the only known electrode material which was compatible with the contact ion engine. Its electron work function is reasonably high (4.5 eV); its vapor pressure is high at emitter temperatures(so that material sputtered onto the emitter will volatilize quite rapidly); and, it has virtually no oxygen retention characteristics. It has the disadvantages of having virtually no strength at grid bar temperatures (800 to 1000°K) and a relatively high sputtering yield.

Nevertheless its performance in many respects has been remarkable. For example, Emitter G-6(b) developed a chipped flute during one of the life tests and as a result a grid bar was cut in half. The engine continued to function satisfactorily for many hours after this had occurred. Considering the cross-section of each bar (.018" x .035") this was quite remarkable.

In reviewing the multitudinous data with copper grids no deterioration in emitter performance has been noted which could be attributed directly to the presence of copper on the emitter surface. This includes cases of complete melt-down of the grid followed by adsorption of Cu into the pores of the emitter.

6.2 NICKEL

Until recently nickel was not even considered as an electrode material for contact engines. It was assumed that the sintering rate of the porous tungsten would be seriously accelerated if even trace quantities of nickel diffused onto the emitter surface.

By controlled sputtering or evaporation of nickel on ionizer buttons, H. Shelton, A. Cho and D. Hall[8] found that high Ni coverages ($\sim$ 1 monolayer) had no effect on neutral fraction, critical temperature or transmissivity. In addition there was no indication of nickel diffusion into the ionizers. Consequently nickel was selected as one material to be evaluated in this program.

Three separate tests have been made at 15 ma/cm^2 using Ni grids:
(1) a 15 hour test with Emitter G-6; (2) a hundred hour test with Emitter
G-6(b); and (3) a 524 hour test using G-6.

Figure 26 shows α_m vs T data taken during a fifteen hour test at
15 ma/cm^2. After 14 hours the minimum neutral fraction dropped from 1.3% to
0.9%. A brief exposure of the ionizer to acetylene returned the minimum to
1.3%. This indicated that the decrease was due to a slight oxygenation of
the ionizer (H_2O was the only detectable source of oxygen in the system at
the time and equalled 1 x 10^{-8} torr).

Figure 27 shows α_m vs T data taken at intervals during life test
No. 5 (see Section 7.6) with G-6(b) at 15 ma/cm^2. The 100 hour data point
required acetylene to eliminate a remnant-oxygen condition which had pre-
vailed for a considerable portion of the test. The measured neutral fraction
had increased from .7 to 1.9%.

Obviously the emitter properties had degraded with time. While this
could possibly have been caused by sputtered nickel on the surface (and this
sputtering rate was quite high in one area due to poor optics) the more likely
explanation is that surface sintering of the emitter is accelerated when
operated in a remnant-oxygen condition.

An almost identical change in the α vs T characteristic of this same
emitter had occurred when a copper grid was used prior to this test. The low
neutral characteristics was recovered by back-bombarding the emitter surface
with negative ions (zero-bias engine operation). This adds further credence
to the conclusion that emitter deterioration was caused by the remnant-oxygen
condition rather than sputtered nickel on its surface.

In the third experiment — a 524 hour life test — with a nickel grid
the emitter operated for 125 hours with generally improving characteristics.
At this point, after a cesium boiler refill, the engine reverted to a
remnant-oxygen condition. Measured α_m vs T characteristics at the 200
hour point are compared with the initial data in Figure 28. Once again, the
"clean" tungsten curve had deteriorated with time. In view of the history of

70
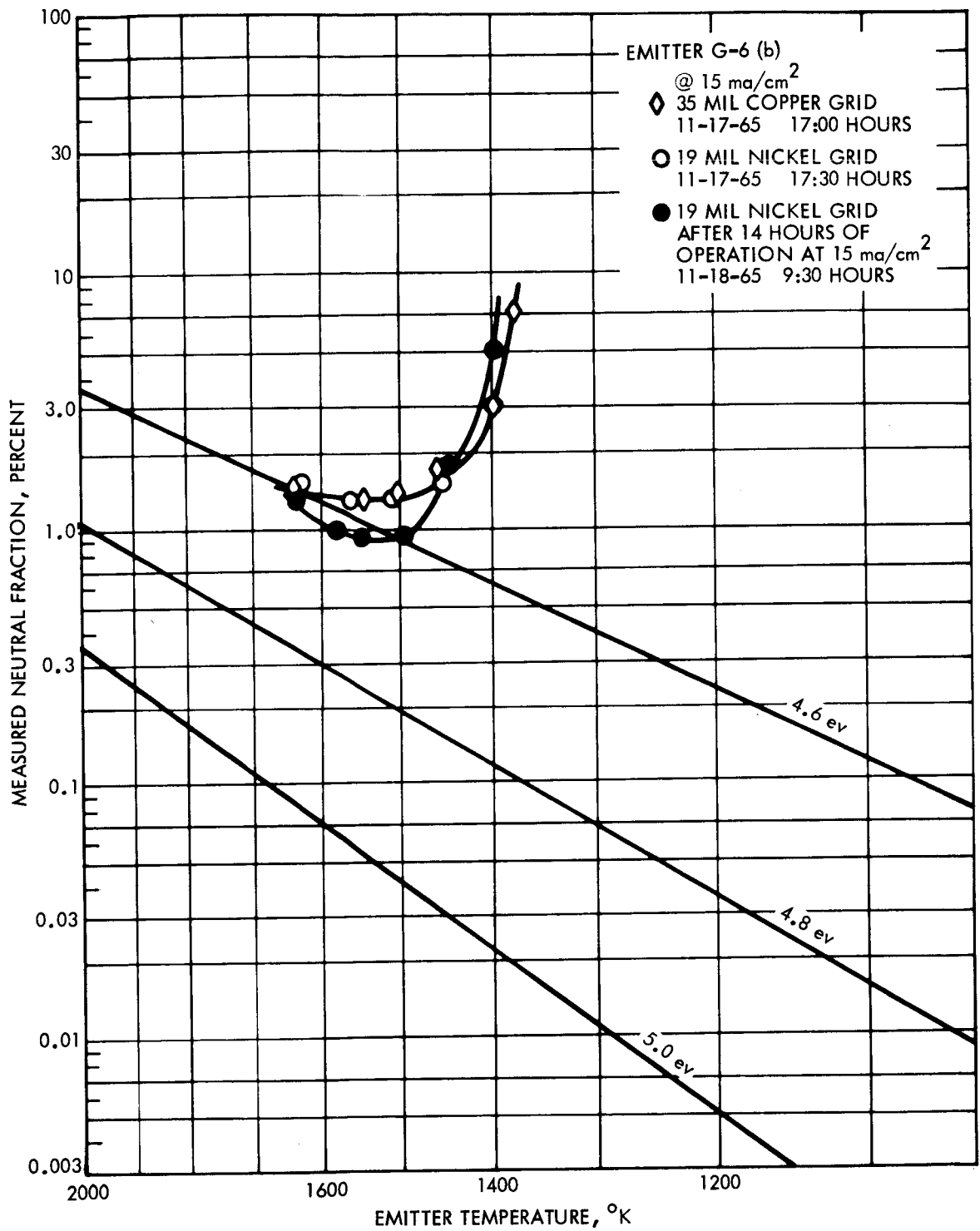
Figure 26. α_m vs T data at 15 ma/cm^2 for a nickel grid [G-6(b)]
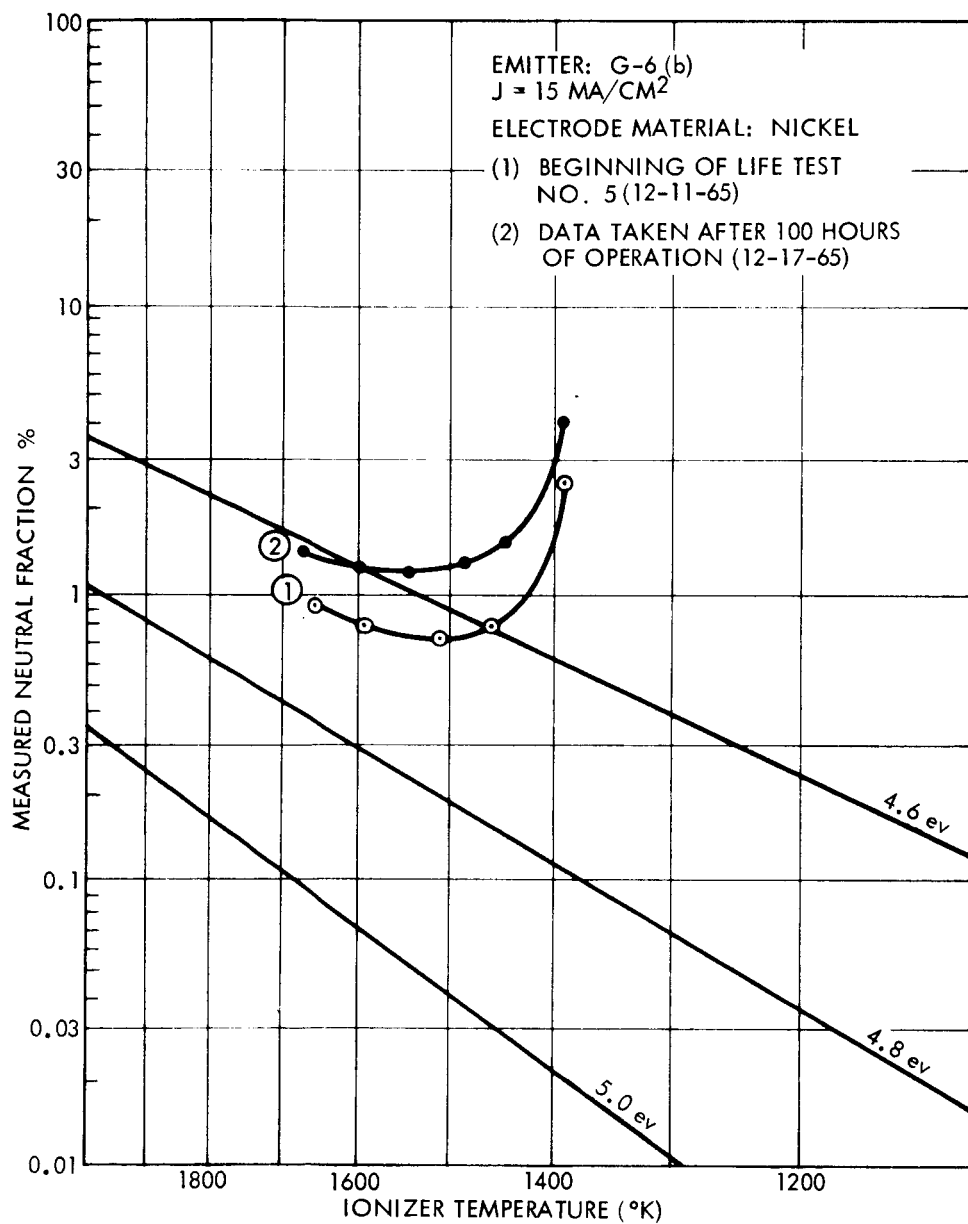
Figure 27. α_m vs T data prior to and after 100 hours of operation (Life Test No. 5).
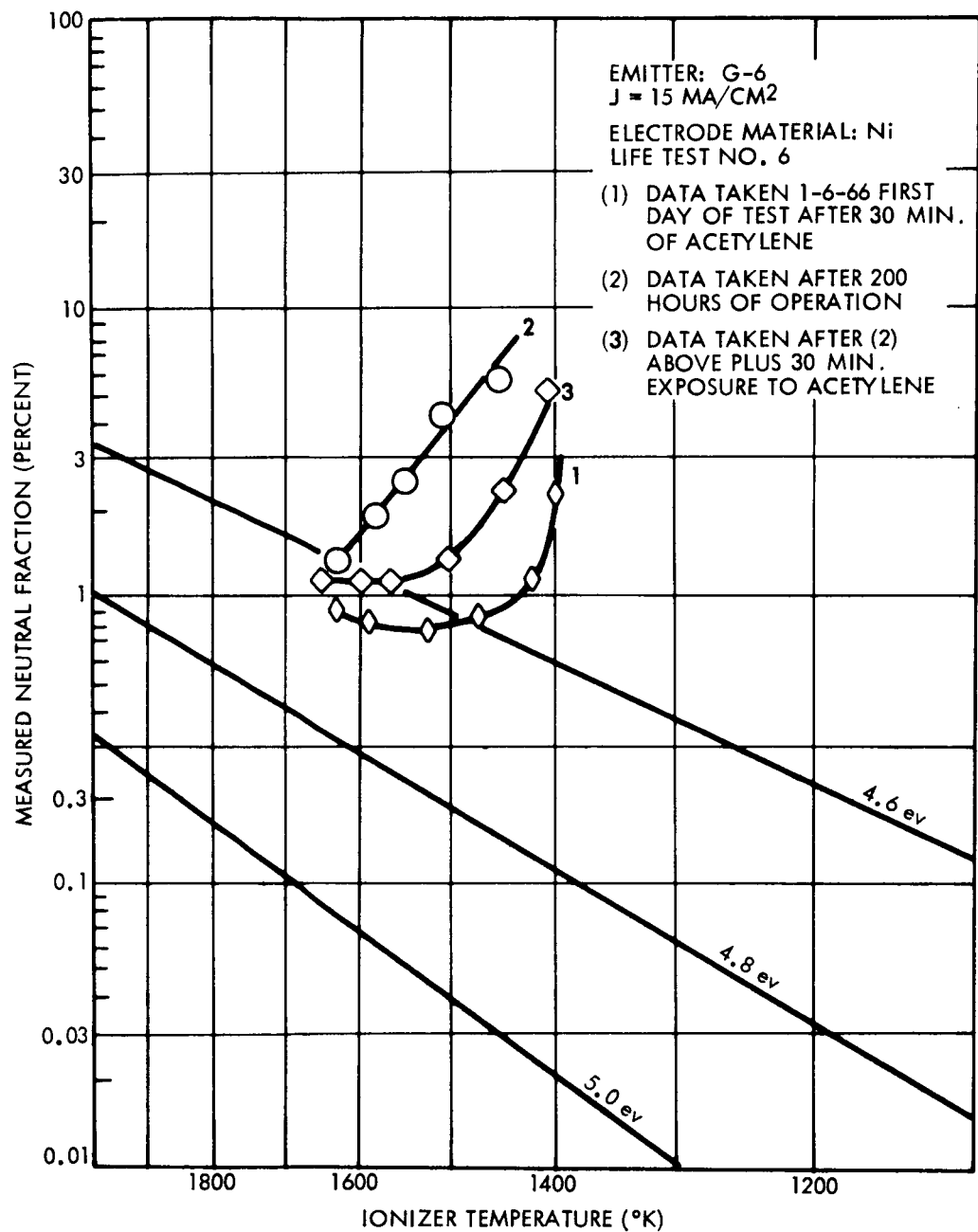
Figure 28. α_m vs T measurements at various stages of life test No. 6 using a nickel grid.

73

this deterioration, nickel is not considered the causative factor. During the first 100 hours there was considerable erosion of the nickel grid bars due to over-expansion of the grid frame — and hence direct interception. Yet during this period the emitter performance was generally improving. For further details of this test see Section 7.6.

From these measurements we conclude that nickel is a safe electrode material (although absolute proof is lacking). It has two important advantages:

1. It exhibits excellent structural stability, and
2. The sputtering yield is much less than that of copper (see Section 6.7 for actual measurement data).

6.3 CUPRO-NICKEL (70% Cu, 30% Ni)

The first test of a cupro-nickel grid lasted 20 hours at 15 ma/cm^2 and indicated compatibility with the TRW engine (see Figure 29). A second test lasted 85 hours at 15 ma/cm^2. There was no evidence of ionizer contamination during this test either. This life test failed because several grid bars had buckled into the beam and were eventually cut in two.

None of the grid bars were welded to the grid frame when the engine was removed for inspection. The conclusion was that cupron grid bars are less structurally stable than copper. However this might simply be caused by improper stress-relief during fabrication.

While cupro-nickel has a higher sputtering yield than nickel these experiments, as well as those of Section 6.7, indicate a much smoother surface results after operation as an electrode material, than either copper or nickel.

6.4 IRON

The Fe grids had a tendency to warp or buckle. Prior high temperature treatment (1000°C for four hours) did not appear to help. The longest continuous test was for a 20 hour period and was terminated when several grid bars had bent far enough into the beam to be almost cut in two. Figure 30 shows α_m vs T measurements at 10 ma/cm^2 indicating that no appreciable performance change occurred with an Fe grid during 15 hours of operation at 9 ma/cm^2 and with an ionizer temperature of 1500°K.
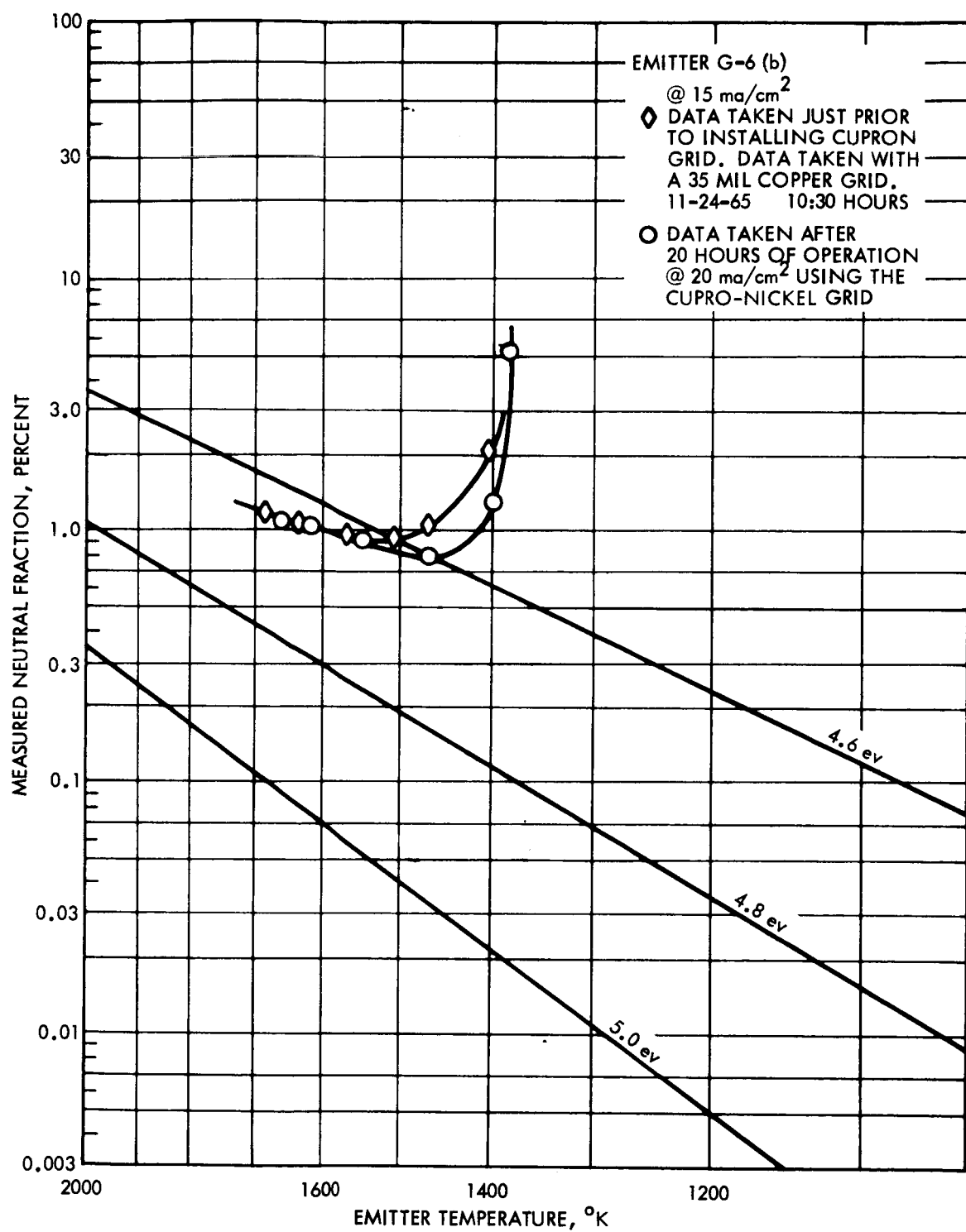
Figure 29. α_m vs T data at 15 ma/cm^2 for a cupro-nickel grid.
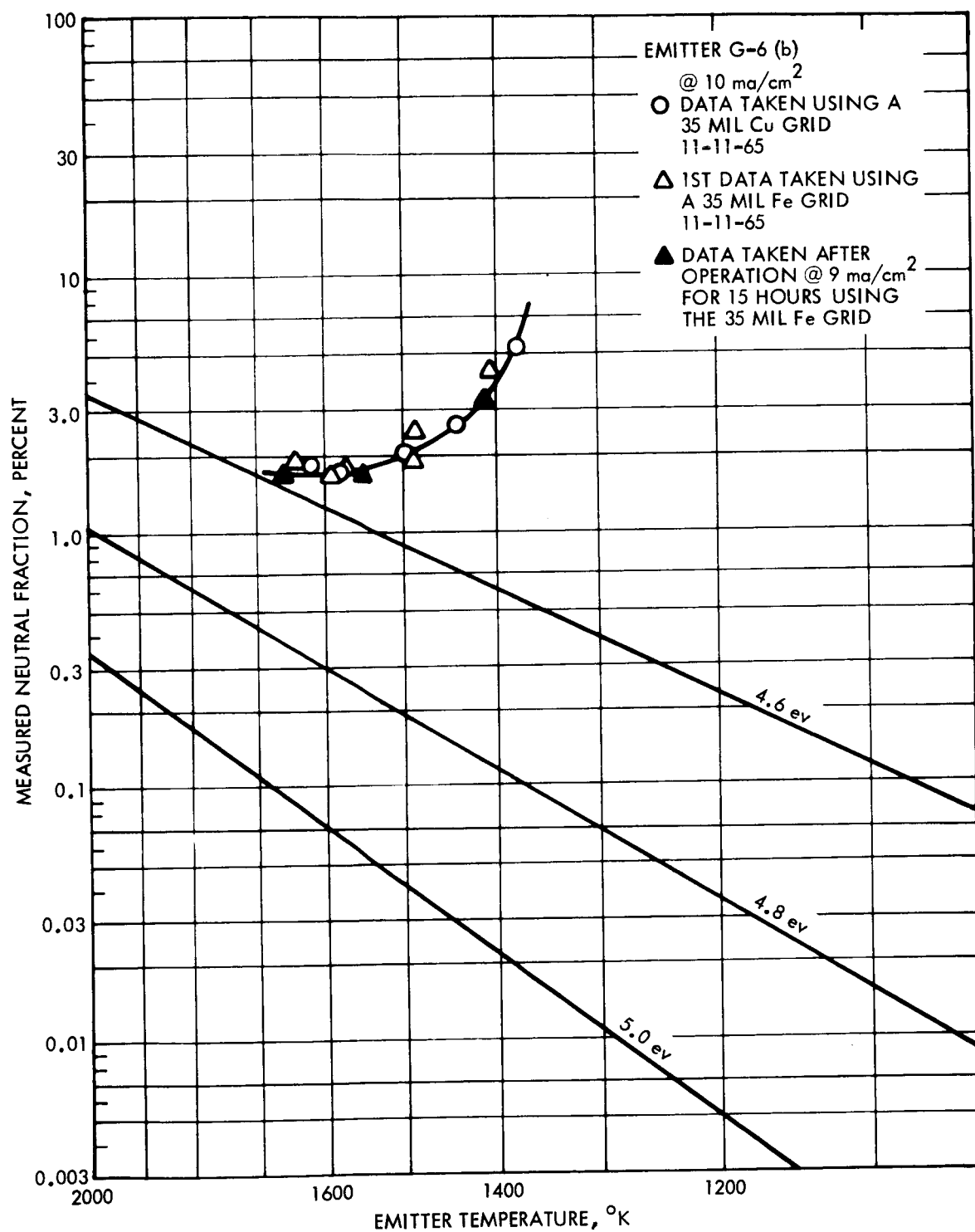
Figure 30. α_m vs T data at 10 ma/cm^2 for an Fe grid.

In other (shorter) tests at higher current densities no detectable change in emitter characteristics were noted. These experiments appear to justify the conclusion that iron would be somewhat superior to nickel (largely because of a lower sputtering yield) if good structural stability would be achieved by a more sophisticated heat treatment during fabrication.

6.5   BERYLLIUM

Five grids fabricated with beryllium grid bars* were tested. Each buckled and shorted out before any significant data could be obtained. However after the longest test which lasted two hours a copper grid was put immediately after the Be grid failed and no change in performance was noted.

Several of the test grids had individual bars stuck to the graphite grid frame. X-ray diffraction analysis indicated that the formation of Be_2C at points where the Be came in contact with the graphite grid frame was causing this sticking. However those grid bars which remained free still showed a tendency to warp despite all efforts to relieve internal stresses by various high temperature heat treatments. Further experiments with a nickel plated graphite frame revealed continued structural instability, without grid bar sticking however.

A joint effort with NASA-Lewis to obtain and test a better grade of beryllium grid bars was arranged as a continuation of the testing program. However, funding for this program was cancelled.

---

*   The first grid had no pre-operative heat treatment. The next two used Be bars that had been heated four hours in a vacuum furnace at 1000°C prior to being installed in the grid frame. All three used grid bars which were from Be sheets which had been fabricated by powder metallurgy techniques. The next two sets of grid bars were cut from flattened 19 mil Be wire. An attempt was made to stress relieve these processed bars by sandwiching them between two heavy ground and polished steel plates and heating this assembly in vacuum to 1000°C for a period of 4 hours.

6.6 COPPER IRIDIUM (Cu-Ir 1%)

Figure 31 shows α_m vs T data from the Cu-Ir grid test run. There was a small improvement in minimum neutral fraction (0.9% at start and 0.7% at finish for a 15 ma/cm^2 beam). When the grid was purposely misaligned so that the grid material would be sputtered back onto the ionizer, no change in neutral fraction was detected.*

Whenever the engine was operated with this Cu-Ir grid, a continuous series of minor arcs occurred which was not characteristic of any other grid materials tested in this program. From our previous experience with W grid bars, where similar arcing was prevalent, this characteristic is believed to reflect the low work function associated with the high binding energy of cesium to a high work function substrate.

6.7 SPUTTERING EXPERIMENTS

There is a fairly wide scatter in the available sputtering data. In order to obtain a more realistic evaluation of comparative sputtering rates for various potential grid materials, a simple experiment was devised.

An air-lock located on top of the No. 1 Test Facility (and approximately one foot in front of the collector) was installed earlier in the program so that emitters can be lowered into the ion beam for surface sputtering and later removed without interrupting engine life tests.

This air-lock also provides electrical isolation (from ground) for the sample in the ion beam. Our experiments have shown that an ammeter connected between a fairly large sample (e.g. 1 to 2 sq. inches) and ground will read within 10 to 20% of the true ion current incident upon it.

In a preliminary sputtering experiment several grid bars of various materials (copper, nickel, iron, cupro-nickel and beryllium) were clamped against a rectangular copper plate which, in turn was fixed to the tungsten rod. This assembly was lowered into the beam and sputtered for 18 hours.

---

* The intention of this misalignment was that of increasing the sputtering rate and hence the accumulation of iridium on the emitter surface. At that time it was believed that iridium coated tungsten had superior ionizer characteristics than that of pure tungsten.
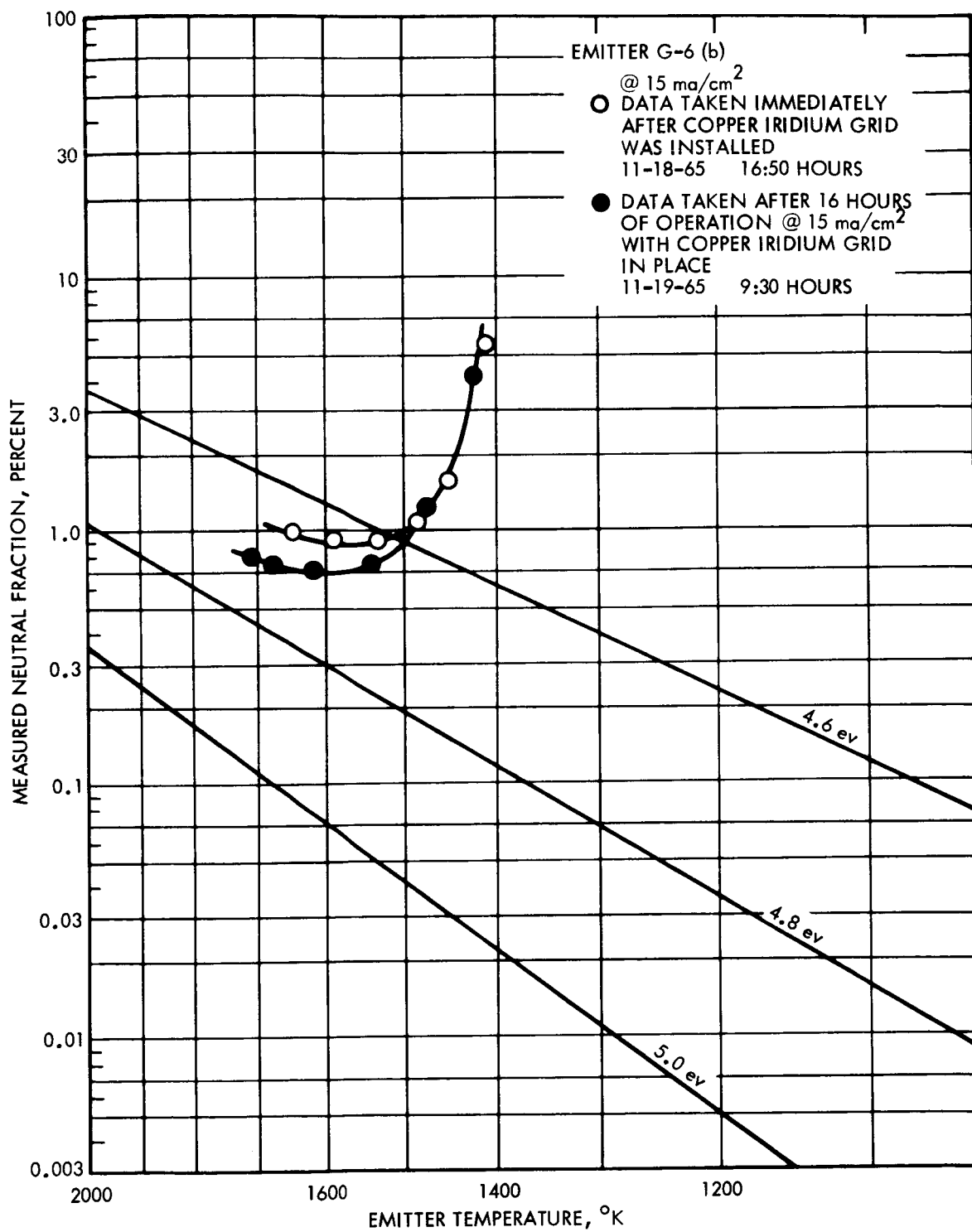
Figure 31. α_m vs T data at 15 ma/cm^2 for a copper-iridium grid (Cu 99%, Ir 1%).

79

After removal the following thickness decrease in the grid bars were measured: Cu, .0022"; Ni, .0011"; Fe, .001"; Be .0006" to .001"; and cupronickel, .0015". While these measurements were rather crude they did point the way toward more sophisticated experiments. A wide variation in sputtered surface condition was noted. The copper exhibited a coarse sputtered surface and in certain sites very non-uniform depth of penetration. The iron bar was quite shiny but when examined microscopically the surface was very jagged suggesting preferential sputtering at various crystal faces. The nickel and beryllium surfaces appeared relatively smooth and uniformly sputtered. The sputtered cupro-nickel surface was exceptionally smooth. However, copper, nickel and cupro-nickel exhibited a tendency to develop a sharp burr along the edges.

In the next experiment rectangular sheets of copper, silicon, beryllium and nickel were clamped between two flat sheets of copper and the assembly wired to a tungsten rod (used to slide the assembly in and out of the beam). This set-up can be visualized from the photograph of Figure 32 where the two copper sheets are placed in their original locations but with the samples removed. Left to right the samples were: copper, silicon, beryllium and nickel. The original assumption in making this assembly was that edge sputtering of the copper clamp which could cause redeposition on the front surfaces of the samples would be slight. After the experiment was completed it was found that this assumption was correct. There was virtually no removal of copper from the sides of the copper sheets. In fact a "burr" was left on many of the copper edges projecting toward the beam. Microscopic examination of these "burrs" revealed a series of microscopic needles. At the base of the copper was eroded deeper than the average over the flat surface of the copper.*

*   Such a result would be anticipated by the experiments of Chenev and Pitkin[9] which indicates essentially zero sputter yield from copper at glancing angles (for xenon ions below 10 Kev in energy). The reason for this drop as 90° is not clear, but the authors speculate that the ion has not imparted much of its energy to the target before being deflected out of it. If this is correct, the incident ion has not been stopped and further sputtering collisions have yet to occur. Since the scattering angle is expected to be small the deflected ion would proceed to the bottom of the "cliff" formed by the burr and excavate a trench by sputtering. This is exactly what is observed in sputtered copper samples which often show either deep holes or mesas surrounded by moats. This observation is believed to be experimental evidence that the scattering hypothesis for low sputtering yields at grazing incidence is correct.
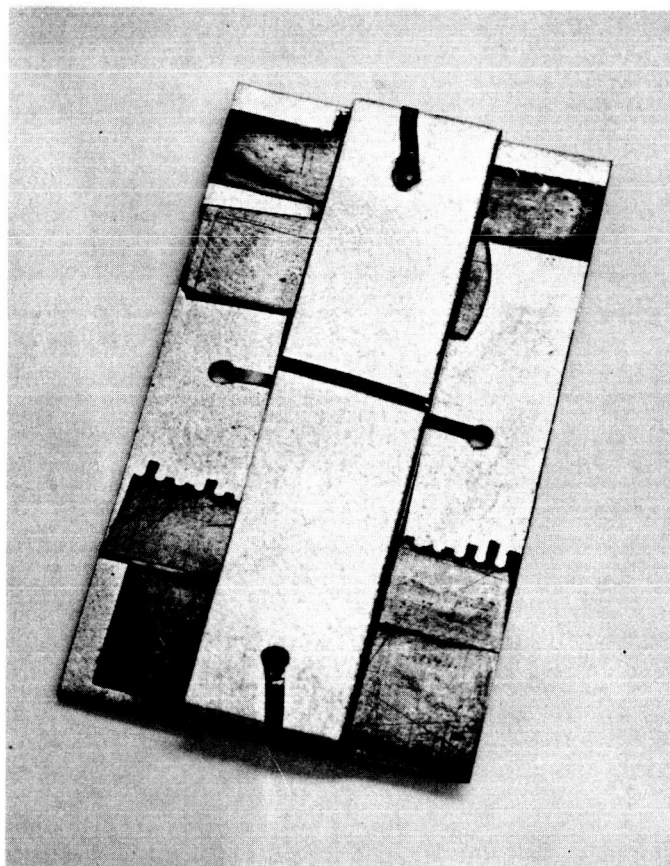
Figure 32. Sputtered shadow pattern illustrating
the arrangement used for the sputtering
experiment. Sample shadows top to bottom
— copper, silicon, beryllium, nickel.

Consequently the only sputtered copper which could redeposit on the flat surfaces of the sputtering samples would be that from the round copper wire used to tie the assembly to the tungsten rod. Since the samples were at a reasonable distance from this wire the relative coverage would be negligibly small. It is concluded then that measurements of thickness change in the central region of each flat strip is a good measure of relative sputtering rate.

Sixty-four hours exposure to 2000 volt ions with a measured average probe current of .27 ma/cm^2 yielded the following depths of sample erosion due to sputtering:

Copper	.008"
Nickel	.004"
Beryllium	.0018"
Silicon	.0022"

Assuming the probe current to be true ion current, the sputtering yield per incident ion would be

for Copper	4.35 per cesium ion	
" Ni	2.33 " " "	
" Be	1.41 " " "	
" Si	.74 " " "	

The sputtered copper surfaces showed various areas where sharp copper needles projected toward the beam. This is illustrated in Figure 33. Presumably these could be generated by a small speck of material with a low sputtering yield on the surface. The sputtered surface is quite rough as illustrated in the photomicrograph of Figure 34. The results with copper probably explain the whisker growth on copper grids which have been experienced in life testing.

The Nickel sample also exhibited some "burring" on the edges but to a lesser degree than copper. Zero sputtering cross-section is probably confined over a narrower range around the 90° angle of incidence. The surface is also smoother. Figure 35 is a photomicrograph of the sputtered nickel surface.

Figure 33.   Enlarged photograph of sputtered
             copper sample.

Figure 34. Photomicrograph of the sputtered
copper surface (.008" removed) 700X.

Figure 35.   Photomicrograph of nickel surface
             after sputtering (.004" removed) 700X.

The sputtered beryllium surface has a very peculiar structure. Figure 36 is a photomicrograph of a central region. It has the appearance of localized melting of the surface. Although the edges of the beryllium sample were quite rough there is some evidence from microscopic examination that the sputtering rate at low angles of incidence is sufficient to prevent the "burring" effect noted with nickel and copper.

The sputtering of silicon yielded an exceptionally smooth surface, almost equivalent to a mirror finish. The photomicrograph of Figure 37 shows the sputtered surface. This sample sheet was cut at right angles to the axis of a 1-1/8" dia. boule. The effect of sputtering on the edges was that of generating a chamfer.

6.8 SUMMARY AND CONCLUSIONS

The results of these experiments are summarized in Table XI. None of the grids showed any tendency to contaminate the ionizer. Be and Fe showed very poor structural stability despite the various high temperature treatments given them to relieve stresses. If these problems could be corrected by improved processing, these materials should make excellent grids. Nickel was the most promising grid material tested. Its structural stability was outstanding, its sputtering yield is 1/2 that of copper, and its physical strength at operating temperatures is high compared to copper.

An attempt was made to correlate grid drain currents with neutral fraction and emitter temperature. No specific difference between materials was noted with the exception of iridium-copper. For the other materials grid drain (in percent) ranged from .15 to .3 of measured neutrals at 10 ma/cm^2 and .5 to 1.2 at 15 ma/cm^2. In some cases, particularly iron and beryllium the drain current varied widely from experiment to experiment. This was attributed to misalignment of grid bars, and hence direct interception.

With either copper or nickel the grid drain is seldom above 1% if the grid is properly registered.

Within the limitations of the important properties of each material are summarized in Table XI below.
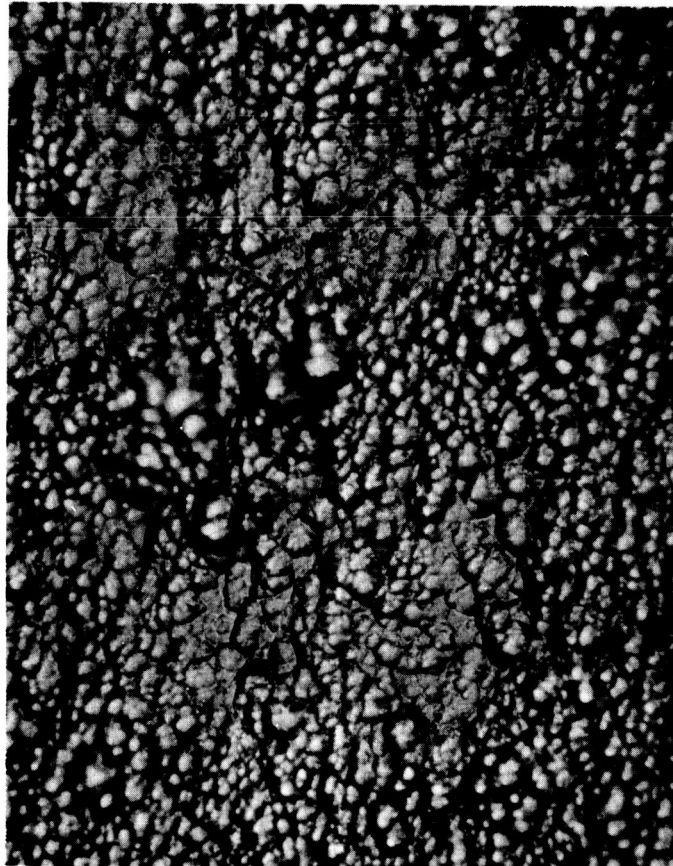
Figure 36.   Photomicrograph of beryllium
surface after sputtering (.008"
removed) 700X.
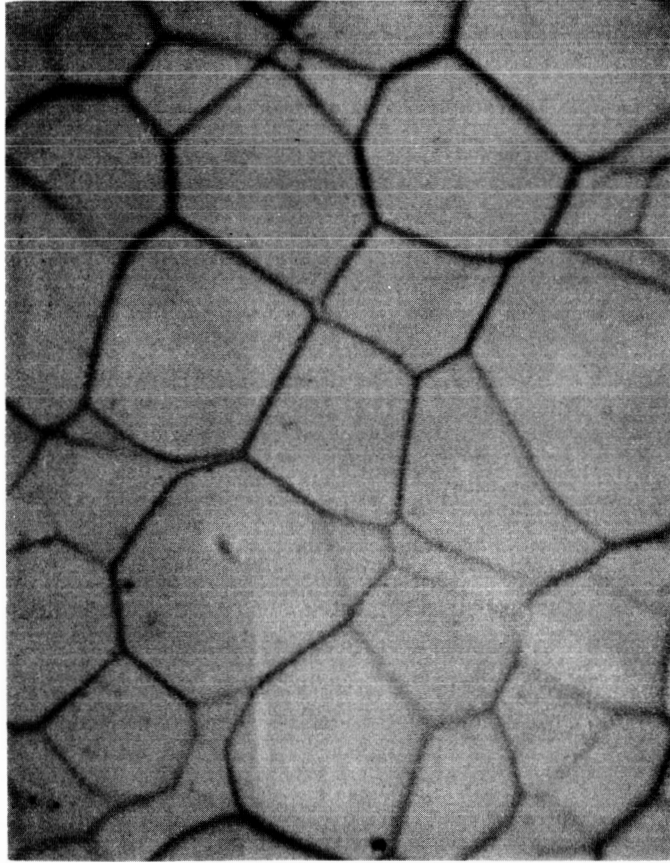
Figure 37. Photomicrograph of silicon surface
after sputtering (.002" removed) 700X.

TABLE XI.

SUMMARY OF GRID COMPATIBILITY TESTS

PLUS OTHER PERTINENT DATA

Grid Material	Be	Fe	Ni	Cupro-Nickel[a,c]	Cu-Ir[b]	Cu
Melting Point °K	1551	1808	1728	1445-1512	~1350	1356
Vapor Pressure[d] in Torr 1500°K	1.2×10^{-2}	1.3×10^{-4}	6.5×10^{-5}	---	---	4×10^{-3}
Mass Sputtering Yield Relative to Cu (Sec.6.7)	0.23	(0.50)[e]	0.50	0.85	1.00	1.0
Drain Currents	Med	Low	Low	Low	High	Low
Effective Contamination at 15 ma/cm² & 2% Measured Neutrals	No Data	None (20 hr Test)	None (524 hr Test)	None	None (15 hr Test)	None (Many)
Structural Stability	Very Bad	Poor	Excellent	Good	Good	Excellent

a. 68.9% Cu, 30% Ni, 0.5% Fe, 0.6% Mn.

b. 99% Cu, 1% Ir.

c. Materials in Design Engineering. Mid Oct. 1965, Vol. 62, No. 5.

d. Vapor pressure data from R. E. Honing, R.C.A. Review, 18, 195-204, (June 1957).

e. The sputtering data for Fe in Sec. 6.7 is not as accurate as that for other grid materials because it was only tested during the first experiment. Other experimenters report a 0.2 sputtering ratio for Fe compared to copper (Wehner Proc. 5th International Conference on Ionization Phenomena in Gas, Munich, Germany, 1961); Stuart, 1961 Trans. 8th Vacuum Symp. and 2nd International Congress, N.Y. Pergamon, 1962.)

7. LIFE TESTS - ELECTRODE &
EMITTER DURABILITY

7.1 INTRODUCTION

The detailed results of 6 life tests ranging from 100 to 524 hours in duration are reported in sections 7.2 thru 7.7 and summarized in section 7.8.

7.2 LIFE TEST NO. 1

SUMMARY: 477 hours at 15 ma/cm^2 using a copper grid, ionizer G-4 No. 2 (E.O.S.), and the TRW Systems' thermal gradient vaporizer feed system.

After 117 hours, the engine was removed to straighten 3 grid bars. These bars had been pushed together when the grid was moved sideways to remove a short that developed between the grid and emitter. After the bars were straightened, the engine was put back into operation for another 360 hours. The test was finally stopped when a cesium leak caused a short to develop across a high voltage insulator. Total operation time on the copper grid was 477 hours.

G-4 No. 2 has solid flute peaks but was not electropolished. A graphic summary of this life test is illustrated in Figure 38. The measured neutral fraction at the start of the test was 4.4% (1480°K)* for a 225 ma (15 ma/cm^2) beam. During the first two days of operation the measured neutral fraction rose to 10% (1560°K)*. From that time on the neutral fraction gradually decreased. During the last 50 hours of test the measured neutral fraction varied between 2.5 and 5% (1520°K).*

The initial grid drain was 1.5 ma and remained below 5 ma until a cesium leak developed after 130 hours. This leak evidenced by an increase in the cesium consumption gradually increased until the consumption was 3 times that of the beam requirements. As a result of the high cesium coverage the grid drain rose to a high and fluctuating level. At the 420 hours point in the life test the grid current was oscillating between 25 and 50 ma with a periodicity of approximately 20 seconds. The fact

* Emitter temperature

90
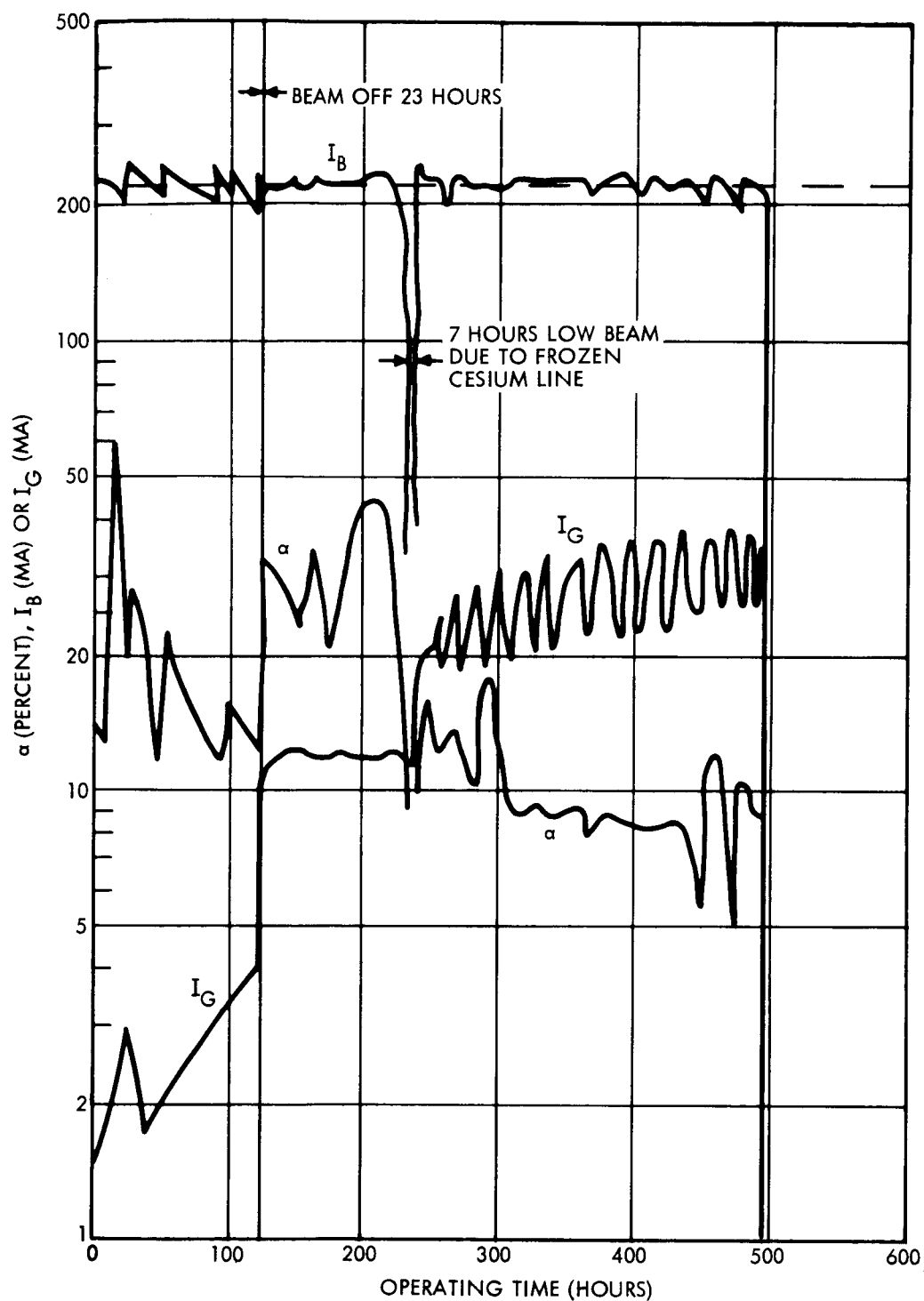
Figure 38. A graphic summary of Life Test
No. 1 [Emitter G-4-2, copper grid].

that the engine could be operated at all in such an environment is rather surprising.

The grid was photographed (see Fig. 39) immediately after removal from the engine.

Inspection of Figure 39 shows that the grid was badly eroded, 3 grid bars were severed, and several have much of their width eroded away by direct interception. Despite that the engine continued to function.

It was found that those grid bars with the greatest erosion were welded to the grid frame at both ends (i.e. to the metal U-channels retaining the assembly). Under such constraint the bars would tend to draw upon cooling and buckle upon heating. In subsequent tests this sticking problem was alleviated by adding a thin graphite strip between the grid bars and the U-channel.

The erosion pattern also indicates an uneven thoughput in beam current density from the emitter. This uneveness in beam current density could be visually observed from the side viewport of the vacuum tank.

The extrapolated electrode life for an engine with a constant neutral fraction α can be calculated by numerical integration of the data of Figure 38. If it is assumed that the end life was 480 hours and that this failure was entirely due to charge exchange erosion then the electrode life (L) associated with an emitter operating at a given current density (J) and a true neutral fraction (α) would be given by the relation.

$$L = \frac{\int_{o}^{480} \alpha_m(t) \frac{(1 + G)}{(1 - G)} J(t)^2 \, dt}{\alpha \, J^2} \quad \text{hours}$$

where $J(t)$ = current density at time t for this life test

$\alpha_m(t)$ = measured neutral fraction at time t

dt = time increment in hours

92
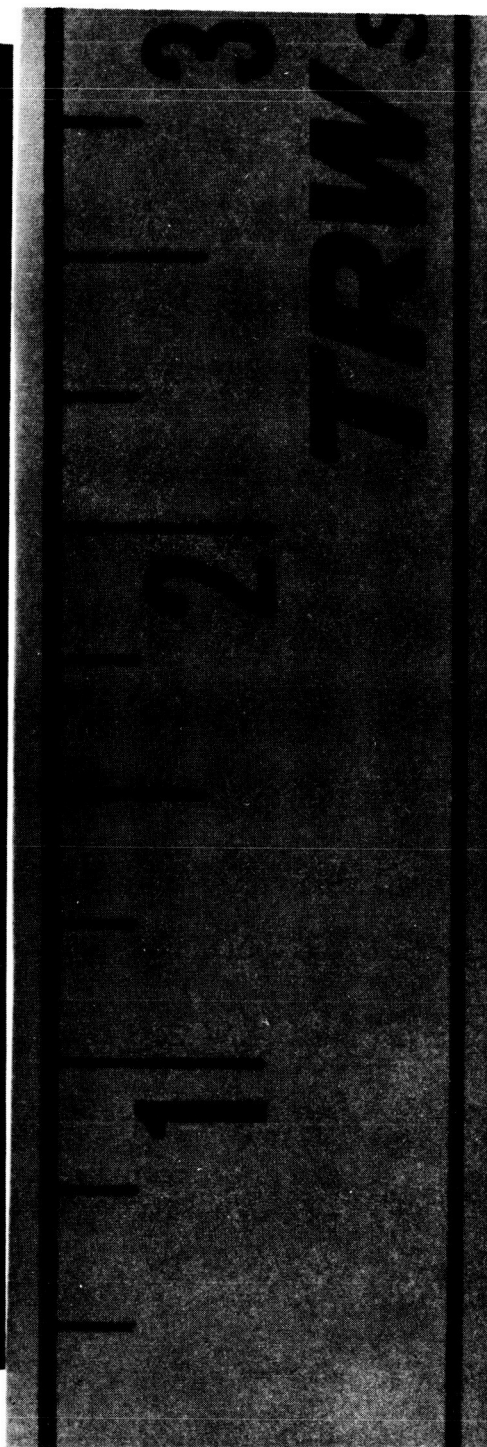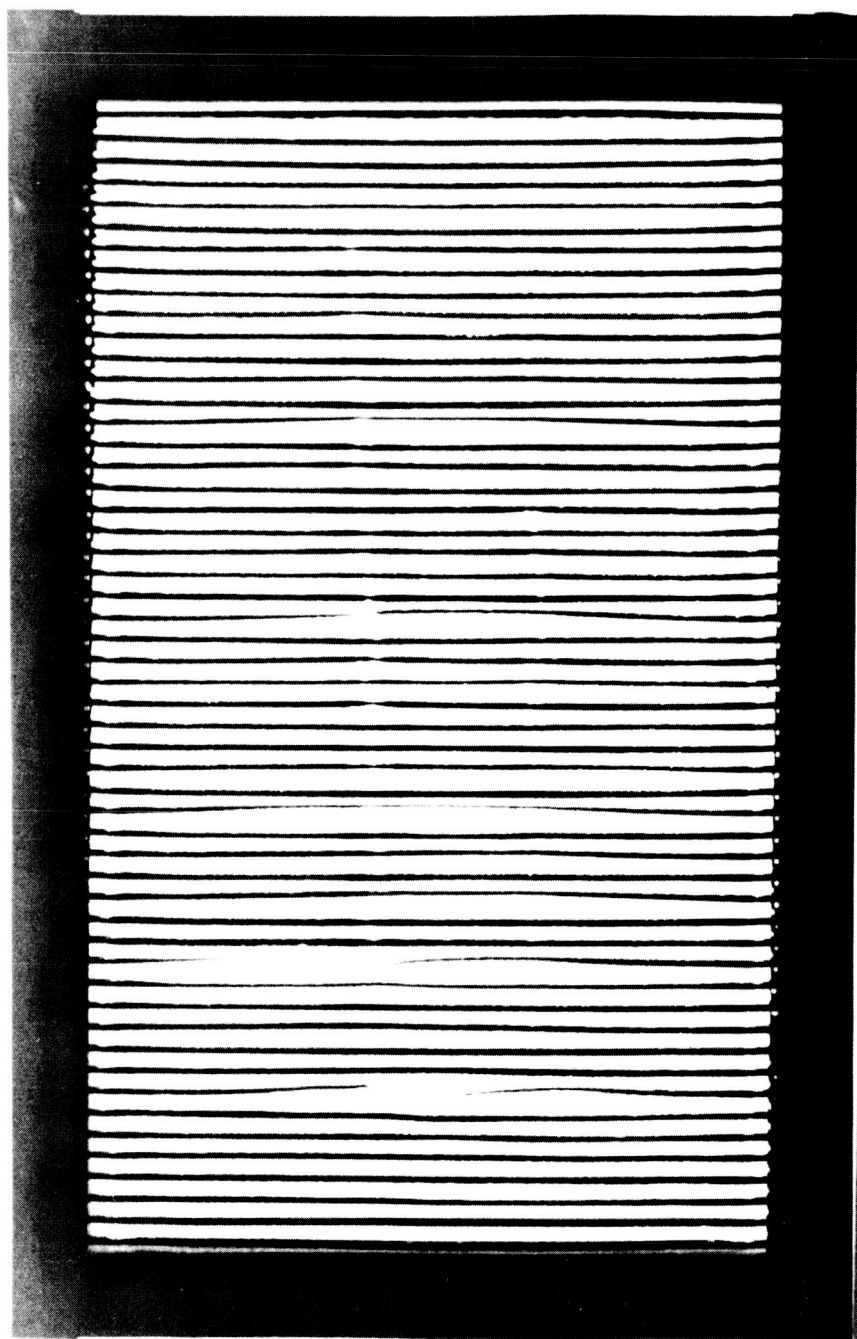
Figure 39. Photograph of the copper grid used in Life Test No. 1.

For example, when $J = 15$ ma/cm^2 and $\alpha = .5\%$. This integration yields an electrode life in excess of 16,000 hours. The rapid erosion of the grid during this test is due to a true neutral fraction 30 times that expected from a good emitter.

7.3 LIFE TEST NO. 2

Summary: 172 hours at 15 ma/cm^2:
          Copper grid:
          Copper boiler:
          Emitter G-6(b)

Emitter G-6(b) was installed into an engine directly after completion of the vacuum cleanup following electric discharge machining. It had been neither sputtered nor electropolished. After installation in the #2 Facility the engine was not operated until the water vapor content within the tank was so low as to be barely detectable.

The conventional (TRW Systems) thermogradient vaporizer type feed system had been replaced by a 500 gram capacity copper boiler so as to eliminate possible contamination of the cesium due to the previous arrangement. This boiler had a separate line connected through the baseplate of the engine flange to an external Nupro all stainless steel welded valve to allow refilling the boiler as necessary. Cesium was transferred from the manufacturer's container directly into a precalibrated pyrex vacuum flask and then through the Nupro valve into the boiler. During transfer the boiler and the emitter were maintained at a low temperature but not less than 100°C.

The startup of this engine was smooth and virtually arc-free. During the first 119 hours the neutrals remained essentially constant at approximately 4% (measured). The grid drain remained below 10 ma total (4%) during this period.

At the end of 119 hours the head gate was closed. With the head gate closed all the external vacuum pumps are removed from the vacuum tank. Gas pressure is maintained at a low level by the pumping action of the ion engine itself. This is partially due to the gettering action of cesium on

94

the tank liners and also the effect of copper sputtering from the collector burying the gas. Under these conditions a vacuum pressure in the 10^{-7} torr range was maintained.

This change did not appear to influence the engine performance in any significant way. The reason for closing the head gate was primarily to prevent diffusion pump vapors from reaching the engine and possibly carbiding of the emitter. Figures 40 and 41 illustrate the variation of neutral fraction with temperature before and after the head gate was closed respectively. As illustrated there is no significant change.

Unfortunately at the end of 172 hours and with the head gate closed the power to the refrigerator used to cool one of the tank liners was accidentally turned off. This caused a pressure rise and eventially an arc developed between the emitter and the grid. Several grid bars were melted and the entire system shut down automatically terminating the test.

Figure 42 shows a graphic summary of the life test. The grid drain and neutral fraction remained essentially constant throughout this period. There was no evidence of any remnant oxygen effect. The higher neutrals (compared to the button data) are believed to be caused by the rough uneven surface associated with electric discharge machining. In later tests after sputtering emitter G-6(b) the measured neutral fraction was reduced by a factor of 3. The corrected neutral fraction then agreed with Shelton's button data. It should be noted that the critical temperatures of the ionizer did correspond to that of the button test during this life test.

Although a spare copper grid was in the grid rack the melt-down accident inhibited removal of the prior grid and it was necessary to remove the engine from the vacuum system. Examination of the emitter surface indicated that it was in good condition.
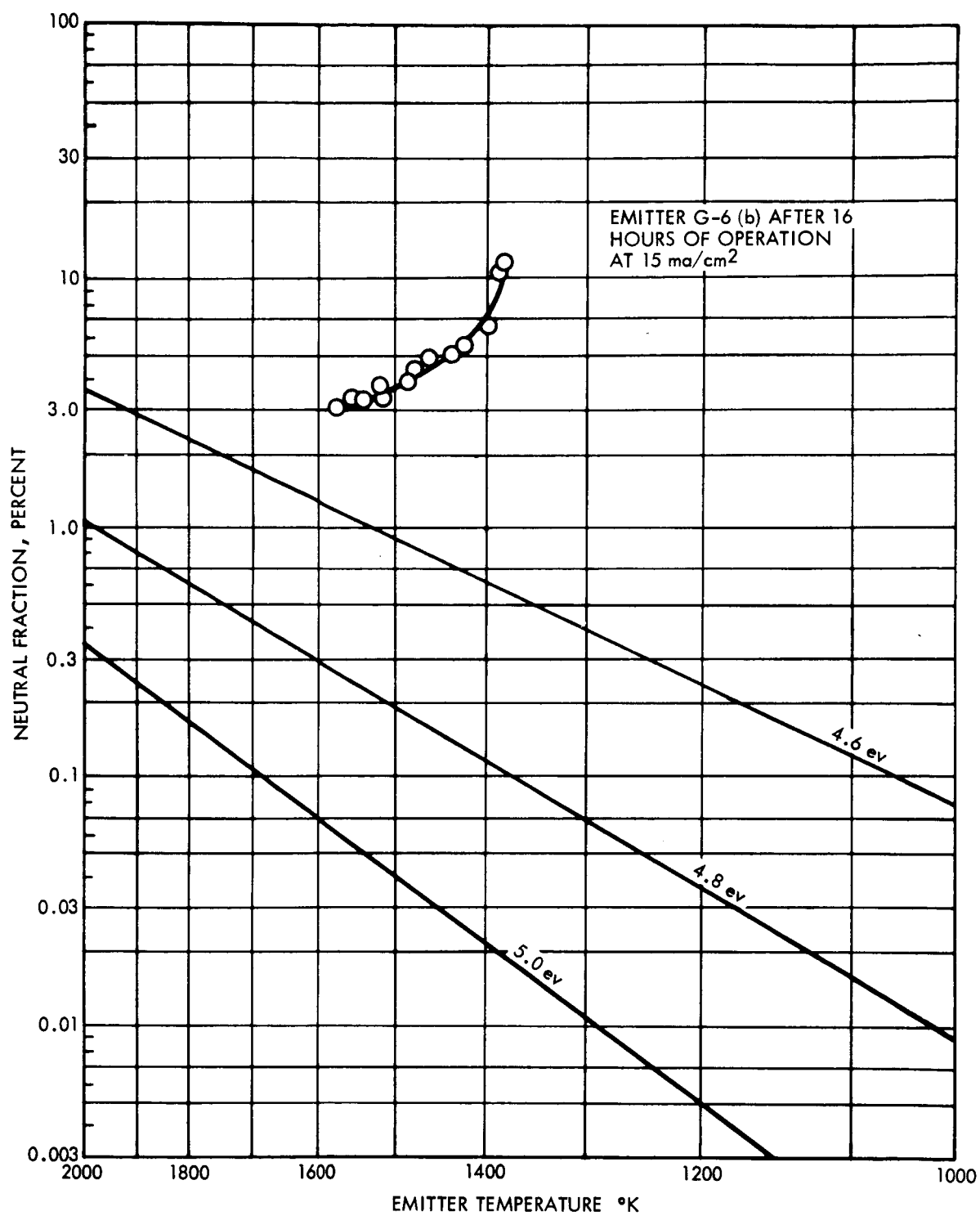
Figure 40. Life Test No. 2. α_m vs T data for emitter G-6(b) after 16 hours of operation.
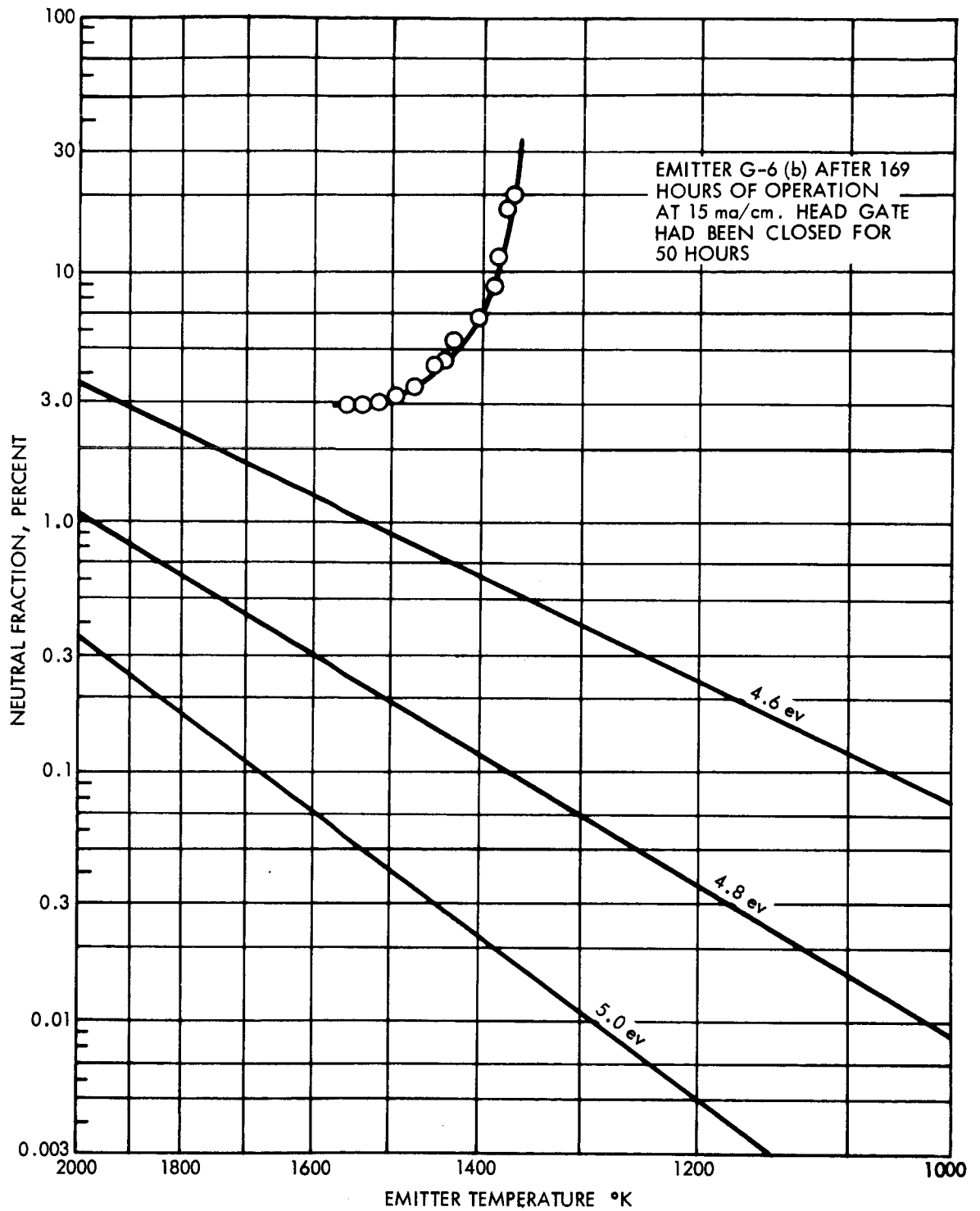
Figure 41. Life Test No. 2. α_m vs T data for emitter G-6(b) after 50 hours of operating with headgate closed.
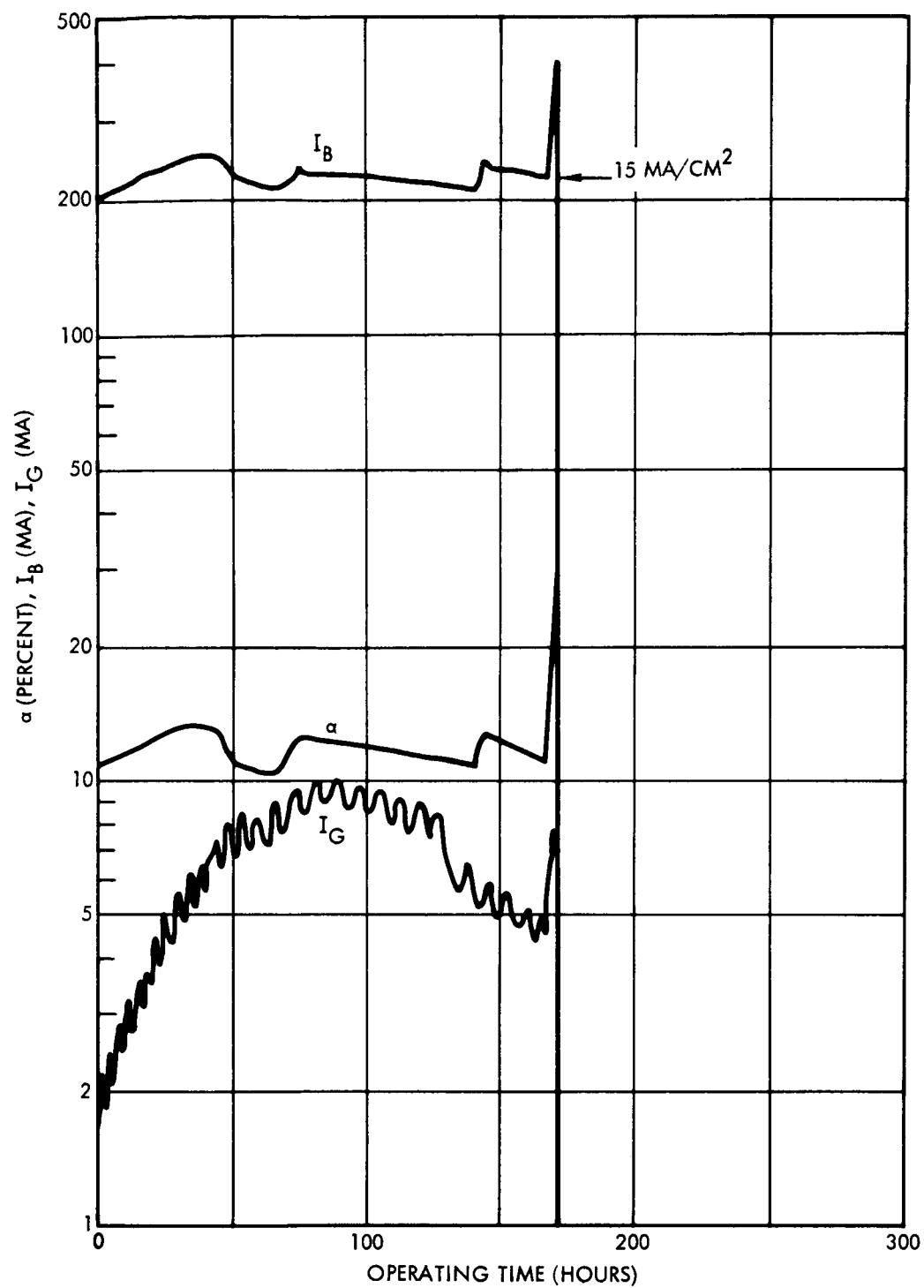
Figure 42. Graphic summary of Life Test
No. 2 [Emitter G-6(b); copper
grid].

7.4 LIFE TEST NO. 3

Summary: 287 hours at 15 ma/cm^2
Copper grid:
Copper boiler:
Emitter G-6(b)

This test was initiated immediately after the engine has been removed, the grid change mechanism repaired, the emitter examined and the engine replaced in the vacuum tank.

The performance was quite stable during this test period, neutral fraction vs temperature data was essentially the same as it was during Life Test No. 2 except that it showed a very slight remnant oxygen ion effect (slightly higher neutrals). This may have been due to the effect of exposing the emitter to atmosphere with a slight amount of cesium retained in the porous region. Figure 43 shows a typical neutral fraction vs temperature curve. The characteristic obtained during Test No. 2 is also included. Figure 44 plots neutral fraction, beam current, and grid drain as a function of time.

This test ended when the grid bar shorted to the emitter. Because the handle to the viewport had been broken during the test it was impossible to visually examine the engine. By racking the grid partially in and out of its normal position it was possible to remove the short and the engine was restarted. Unfortunately the short occurred again before full beam density had been achieved. This process was repeated several times before the test was finally terminated.

The emitter and engine was once more removed from the vacuum station and examined. Once more the emitter appeared to be in generally good condition even though the surface was relatively rough (this condition was consistent with the as-received emitter after electric discharge machining).
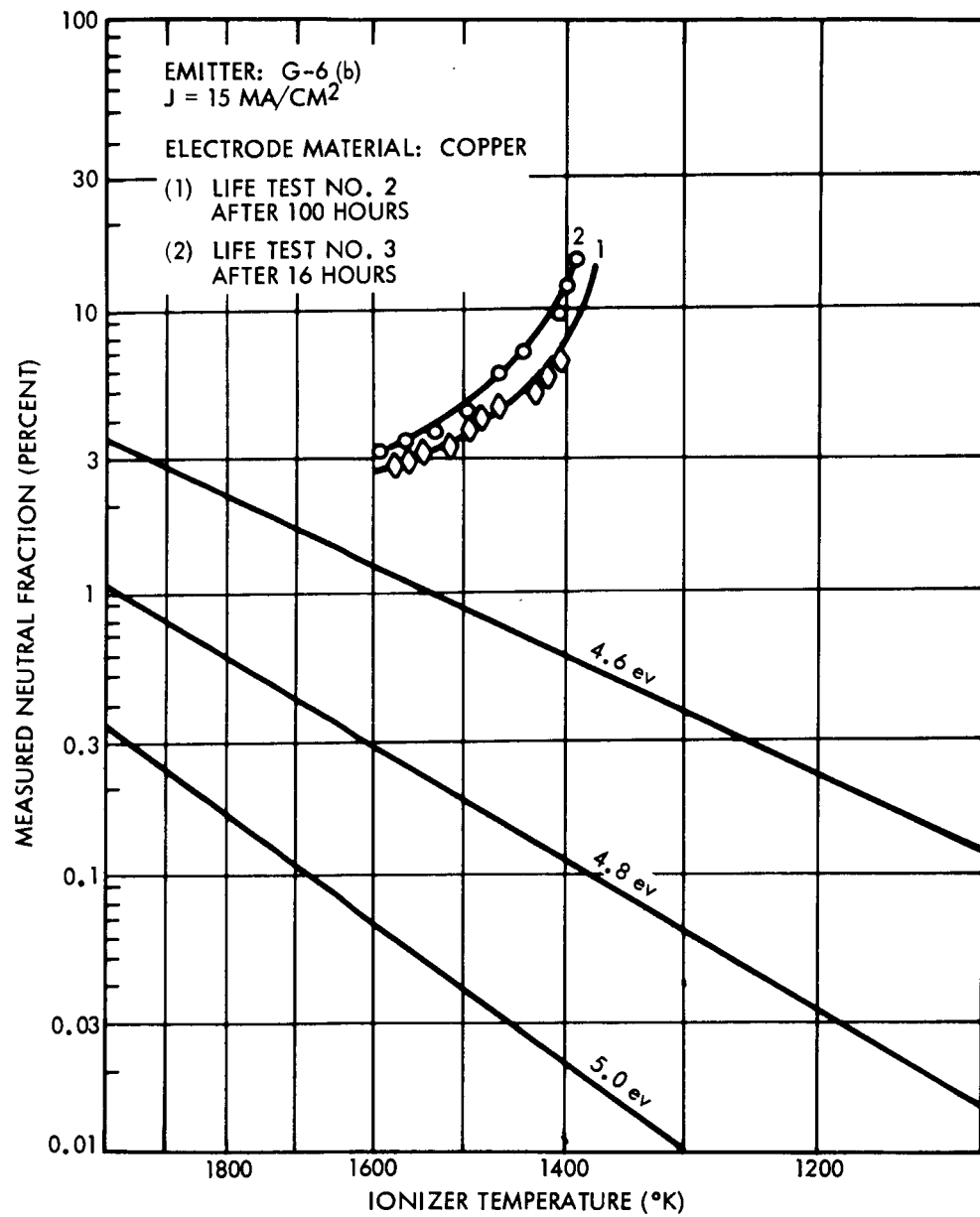
Figure 43. Evidence of a partial remnant-
oxygen condition during the early
stages of Life Test No. 3.
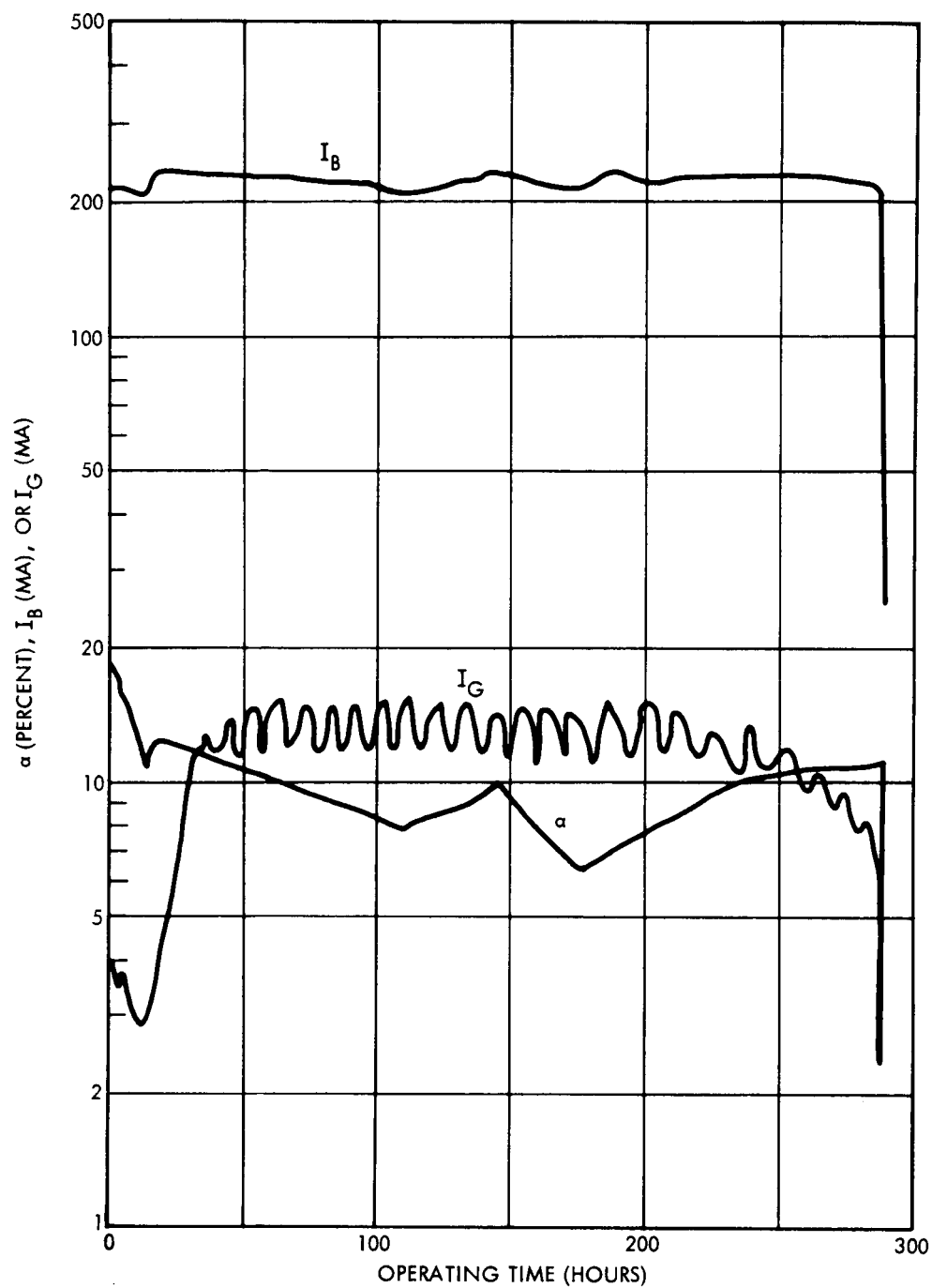
Figure 44. Graphic summary of Life Test
No. 3 [Emitter G-6(b); copper grid].

7.5 LIFE TEST NO. 4

Summary: 313 hours at 15 ma/cm^2
Copper grid:
Copper boiler feed system:
Emitter G-6(b) (after sputtering)

After Life Test No. 3 the engine was removed from the vacuum station for post examination. After being reinstalled in the vacuum test station No. 2 it exhibited a typical remnant oxygen condition as was illustrated in curve No. (2) of Figure 18. Subsequent oxygen-acetylene cycling returned the emitter essentially to its condition of the two previous tests. It was decided however that the sputtering operation which was now a standard part of the fabrication procedure should be performed prior to the next life test in the hope of achieving improved performance. The engine was dis-assembled and the emitter was sputtered by lowering it into the ion beam from Emitter G-4-3 which was then operating in the tank #1 vacuum station. After removal of between 75 to 100 millionths of an inch from the emitter surface it was examined superficially, reinstalled in the engine which was in turn placed in vacuum station #2 and Life Test No. 4 was begun.

The initial neutral fraction vs T measurements made during this life test showed an improvement in neutral fraction by almost a factor of 3 following the sputtering (sec. 5.3). During the first 185 hours of operation the neutral fraction decreased from an initial 1.3% to as low as .4% and averaged approximately 1%. At this time a leak developed in the feed line connection to the boiler, the engine was removed and the boiler returned and the system replaced in the vacuum station. During the first 20 to 30 hours of operation following this repair the emitter exhibited an oxygenated characteristic with neutrals as low as .1%. They gradually increased to 1 1/2% and then tended to improve. At the 300 hour period the neutral fraction was 1% (measured).

102

At the end of 250 hours total test time it became obvious that one grid bar was intercepting the ion beam. At the 300 hour mark this bar was completely cut in half. The engine continued to function for an additional 13 hours at which time the upper portion of the grid bar slipped down and shorted to the emitter.

The grid was replaced in the grid storage rack and the engine removed from the vacuum tank under an argon bag so that the grid could be removed and examined. The engine was then replaced in the vacuum system. Figure 45 is a photograph of this grid taken from the upstream side; Figure 46 is a photograph of the grid taken from the downstream side. Both of these photographs (Figure 46 in particular) show the evidence of localized poor optics. It was decided therefore, to remove the engine once more from the vacuum station and examine the emitter surface. It was found that the emitter surface had several irregularities mostly characterized by ball or wart-like protrusions from the regular contour. The largest of these was about 2 thousandths of an inch in diameter. By comparing the location of these irregularities with the eroded grid a perfect match was found.

Although these platelets had not been observed after the sputtering operation other emitters have exhibited similar effects especially when an excessive amount of material has been sputtered. Presumably then this was the causitive factor for the protrusions.

The surface condition was partially corrected by means of a specially shaped broach which was used to scrape one flute contour at a time. In the area matching that where the grid bar had been cut in half one solid tungsten flute was actually broken away. This might have happened during the latter portion of test #3 when the grid was racked in and out several times.

In summary this emitter performed very well for a period of 313 hours. The graphic summary is plotted in Figure 47. The fact that a low neutral fraction matching and even surpassing the equivalent button test data for this period of time and without further addition of acetylene proved that indeed the long term stability of an emitter could be achieved.
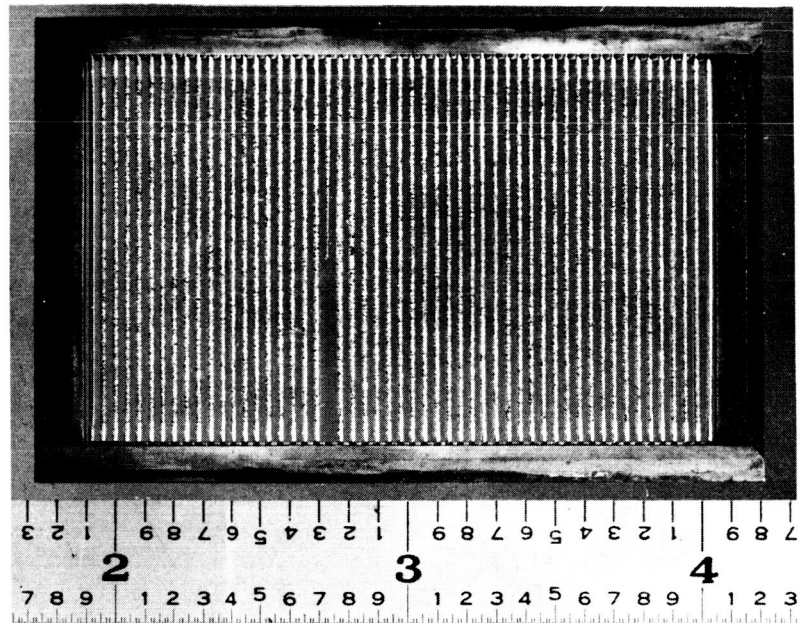
Figure 45.   Photograph of the 35 mil copper grid
             used in Life Test No. 4 (upstream view).
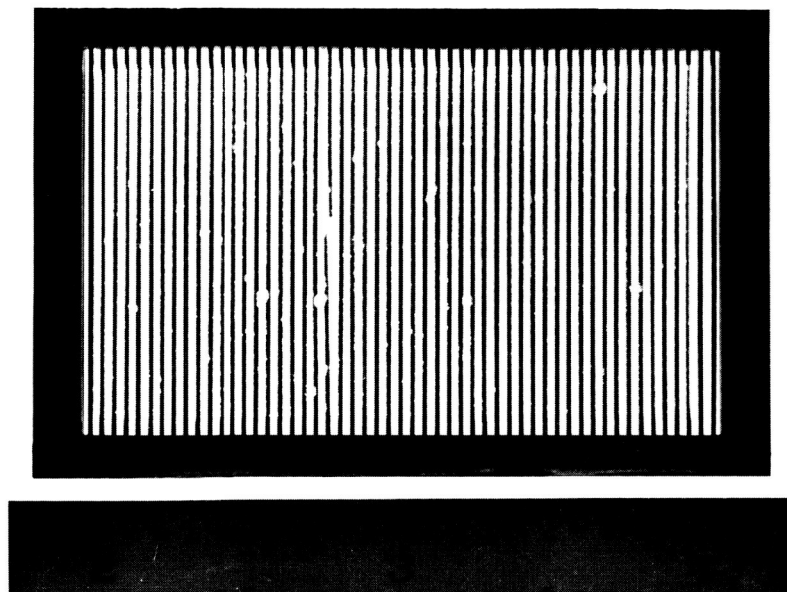
Figure 46.   Photograph of the copper grid used
   in Life Test No. 4 (downstream side).
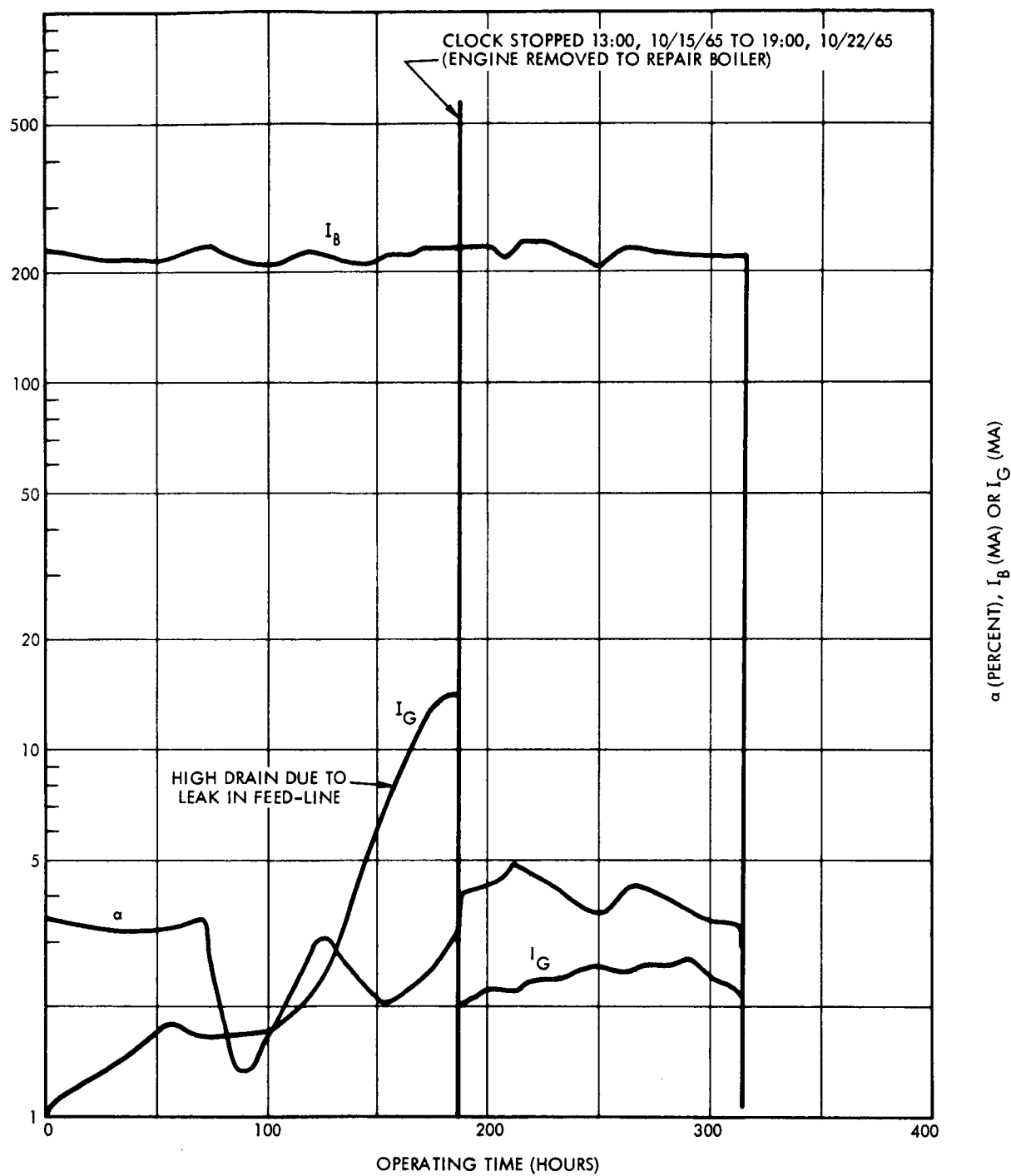
Figure 47. Graph summary of Life Test No. 4
[Emitter G-6(b); copper grid].

7.6 LIFE TEST NO. 5

Summary: 100 hours at 15 ma/cm^2
Nickel grid:
Copper boiler feed system:
Emitter G-6(b)

Although the emitter surface was considerably improved after scraping the contours with a broach, the broken flute made it obvious that any life test would be terminated eventually by a grid bar being cut in two. It was decided however, that this emitter could be used to check the long term stability of an engine employing a nickel grid and a test was initiated.

As the test proceeded the emitter became gradually oxygenated as indicated by the remnant oxygen type α vs T data and increased grid drain (see Figure 48 for a graphic summary of this life test). The oxygen contamination was caused by a high partial pressure of water vapor (i.e. 5 x 10^{-7} torr) during the first 30 hours of operation. The neutral fraction increased from .7% initially to 2.5% at the end of the test. After a short period of acetylene exposure however the neutral fraction decreased to 1.19%. The "clean" α vs T characteristics at the beginning and end of the test were discussed in Sec. 6.2 and illustrated in Figure 28.

The grid drain remained low throughout the test, never rising above 4 ma ($\sim$ 1.6% of the beam current) even in the remnent oxygen condition. The grid performed well and, like our copper grids, the bars remained perfectly straight throughout the test.

7.7 LIFE TEST NO. 6

Summary: 524 hours (operating time) @ 15 ma/cm^2
Nickel grid:
Copper boiler:
Emitter G-6 (electropolished):
Emitter temperature: 1550°K

This section summarizes our most successful life test during this series. The nickel grid which was used for this test was installed at 0800 hours January 5, 1966 and operation with the full ion beam commenced at 0950 hours of the same day. 581 hours later (1445 hours January 29, 1966) this test was terminated due to a short which developed between the ionizer baffle and the grid rail (post examination showed that this was caused by peeling of sputtered material on the ionizer baffle). The grid itself was in good condition at the end of the test and in no way contributed to the termination of this test.
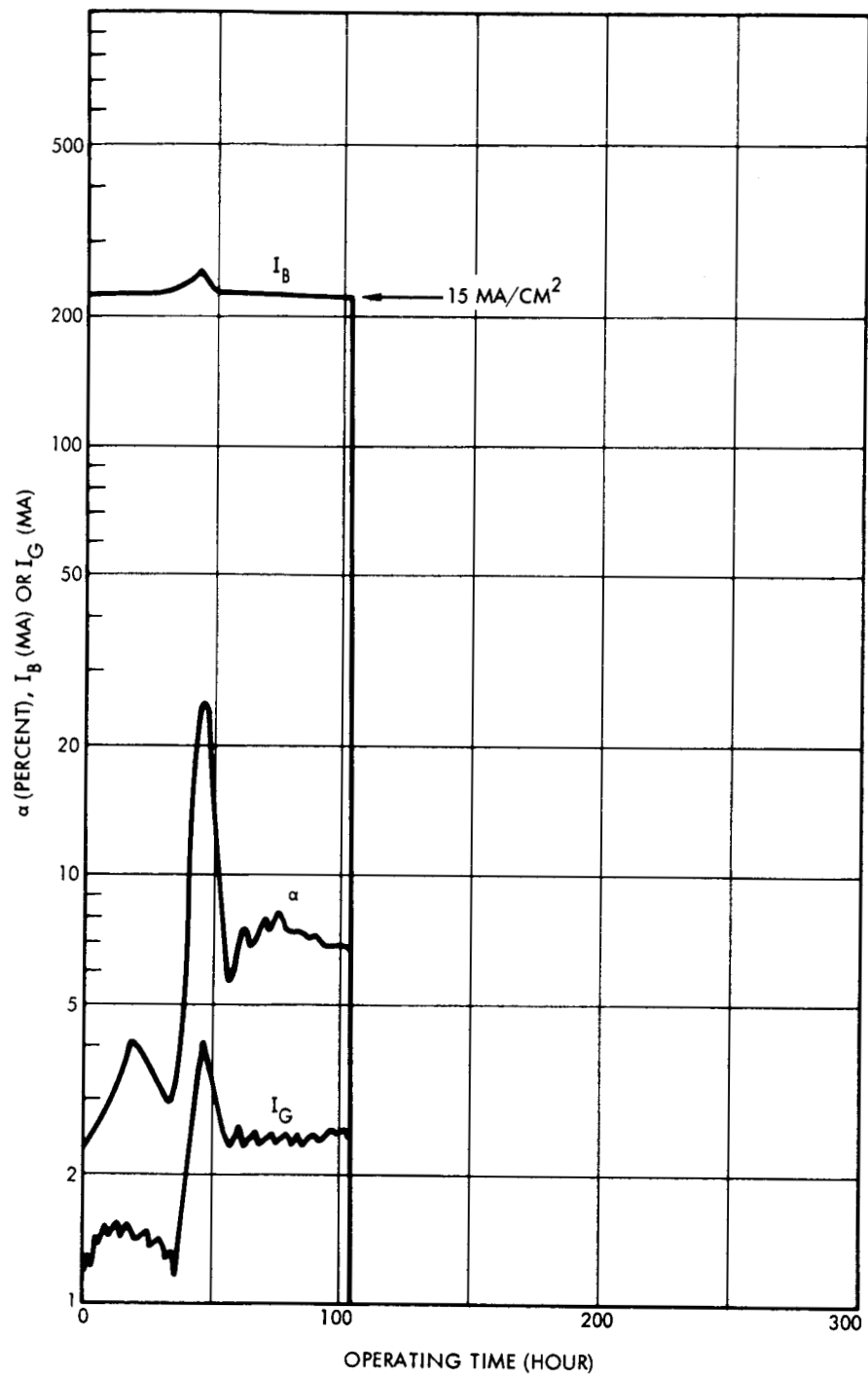
Figure 48. Graphic summary of Life Test No. 5
[Emitter G-6(b); nickel grid].

107

Emitter G-6 was installed on December 27, 1965 in vacuum facility No. 2 together with several grids, in the storage cartridge (1 copper, 1 cupro-nickel, 1 iron, 1 nickel and 1 tungsten heat shield grid). On December 28 the emitter was brought up to temperature for the first time and emissivity measurements were made. An emittance of $0.2 \pm .01$ @ 1500°K was measured.

The cesium boiler was filled, a copper grid installed, and α vs T measurements made for the first time. These are summarized in Figure 25 showing the initial remnant oxygen condition and the "clean tungsten" curve obtained by adding acetylene.

An iron grid was installed for life testing. Measured neutrals were 1.55 to 1.65% @ 1480°K and 15 ma/cm^2. Unfortunately the grid buckled during the first hour's operation.

It was then decided that the life test would be initiated using a cupro-nickel grid and test undertaken at 1705 hours December 30, 1965. This test failed due to a buckled grid bar after 85 hours of operation so the nickel grid was installed and Life Test No. 6 was begun.

During the next 581 hours engine operation was interupted twice for boiler refill and three times because of a faulty ballast resistor in the external control circuitry. The test, which was finally terminated when a short developed between one of the grid frame guide rails and the ionizer baffle, yielded a net operating time of 524 hours at full beam current.

Figure 49 illustrates the variation of beam current, grid drain current and neutral fraction with time during the test. The results are unusual in two respects: (1) the drain current which ranged between 3 and 9% (averaging 4.8%) was much higher than that for any other life test; and (2) the neutral fraction which remained quite low during the first 120 hours of operation, increased quite significantly after the first boiler refill and remained high during the remainder of the test. Possible explanations for these characteristics are discussed at the end of this section.
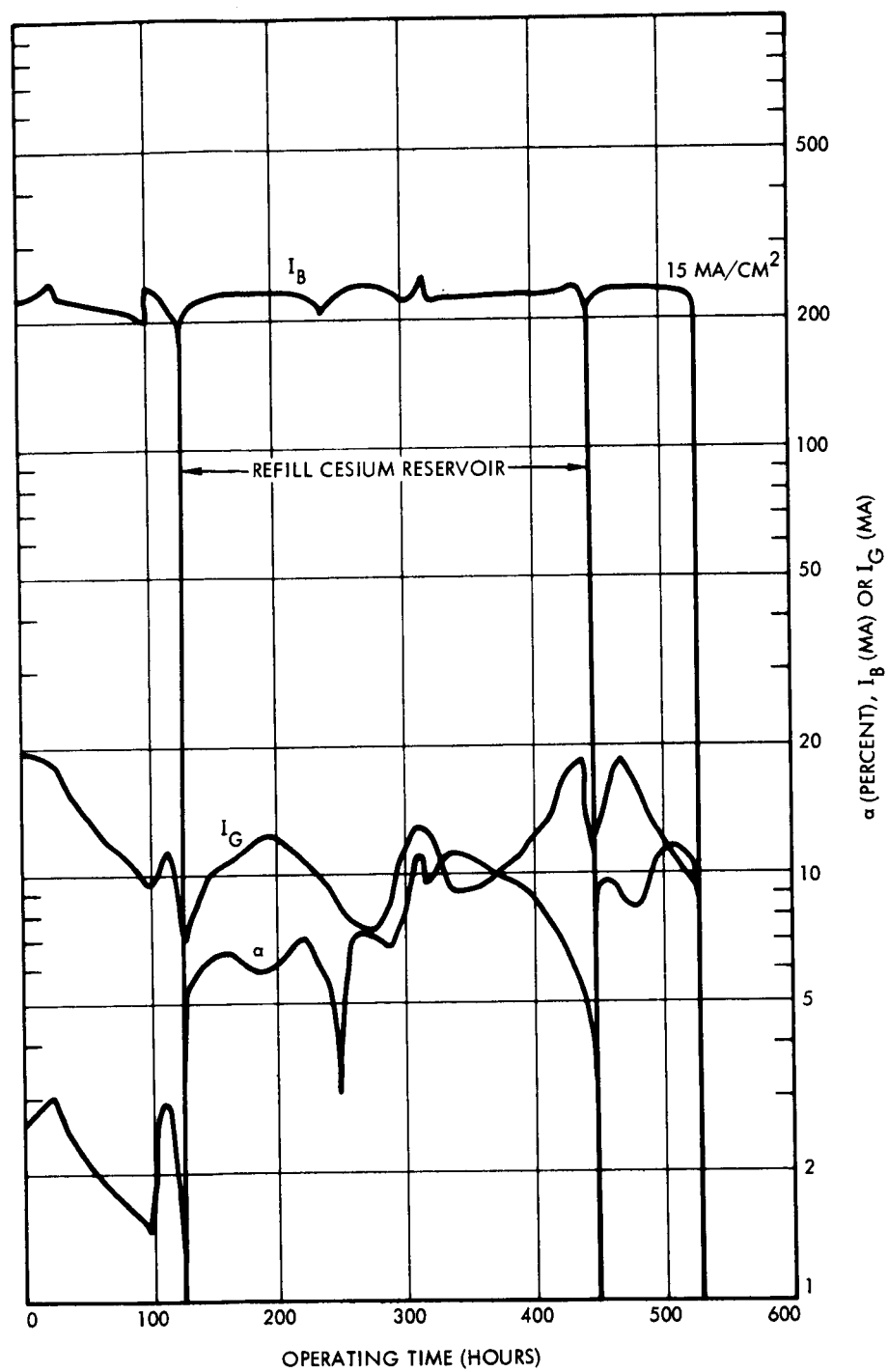
Figure 49. Graphic summary of Life Test No. 6
[Emitter G-6; nickel grid].

Immediately after removal of the engine from the vacuum facility after the termination of this test, photographs were taken of the nickel grid. Figure 50 is an enlarged view of the upstream side; Figure 51 is a similar view of the downstream side. Grid erosion is slight on the upstream side, while there is evidence of considerable erosion on the downstream side. Note that this erosion took place on the outer edges of the grid bars (away from center) indicating over-expansion of the grid frame. This is the first time that this type of mis-registration has been observed. The majority of the erosion took place during the first 100 hours of operation.[*] Because of it, the true charge exchange erosion is diffisult to assess.

The operation of the engine throughout this test was generally smooth and arc free. During the first 60 hours small arcs as evidenced by grid drain current pulses on the strip chart recorder, occurred at the approximate rate 1 per hour. (These were usually undetectable on the ion beam current chart). After 60 hours of operation this rate was down to approximately one arc in 4 hours.

During the major portion of the test, the engine was operated with the head-gate closed. The oxygen or water vapor content of the vacuum gases was usually below the detectability limit of the gas analyzer (1×10^{-8} torr). Nevertheless, the emitter exhibited a strong tendency to return to the remnant oxygen condition after acetylene exposure.

The engine was exposed to thirty minutes of acetylene gas (at a pressure level ranging from 5 to 9×10^{-6} torr) at the 5, 30 and 200 hours points. At the 30 hour interval a temporary decrease in neutrals to 1.15% was noted. This however increased to 2.1% within 1 hour and remained at this average level until after the first boiler refill. An α vs T measurement prior to the addition of the acetylene at the 200 hours interval showed a typical remnant oxygen condition. Some of these α vs T curves were illustrated in Figure 28.

[*] as determined by visual observation through the side view port of the tank (see Figure 11)

110
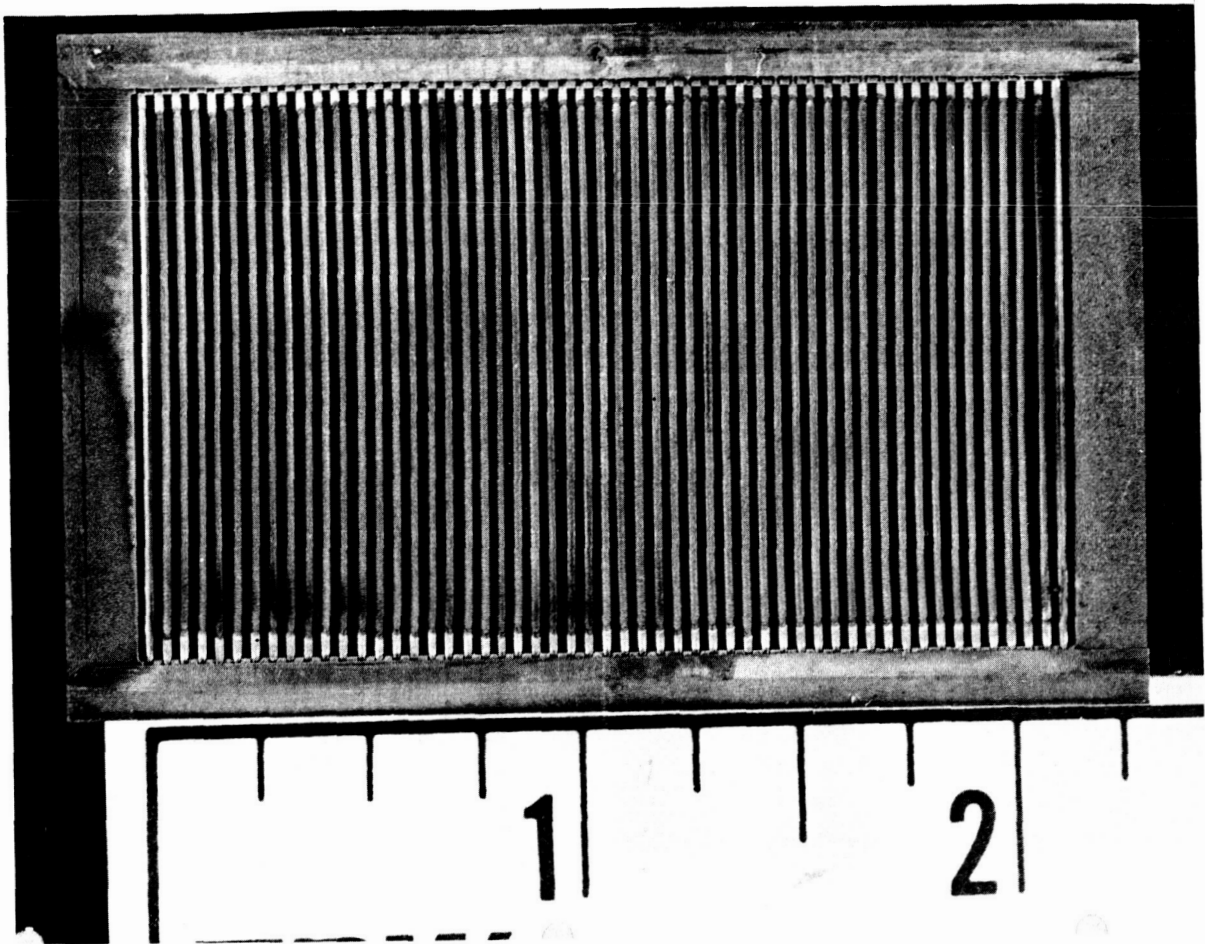
Figure 50. Nickel grid used in Life Test
No. 6 (upstream side).
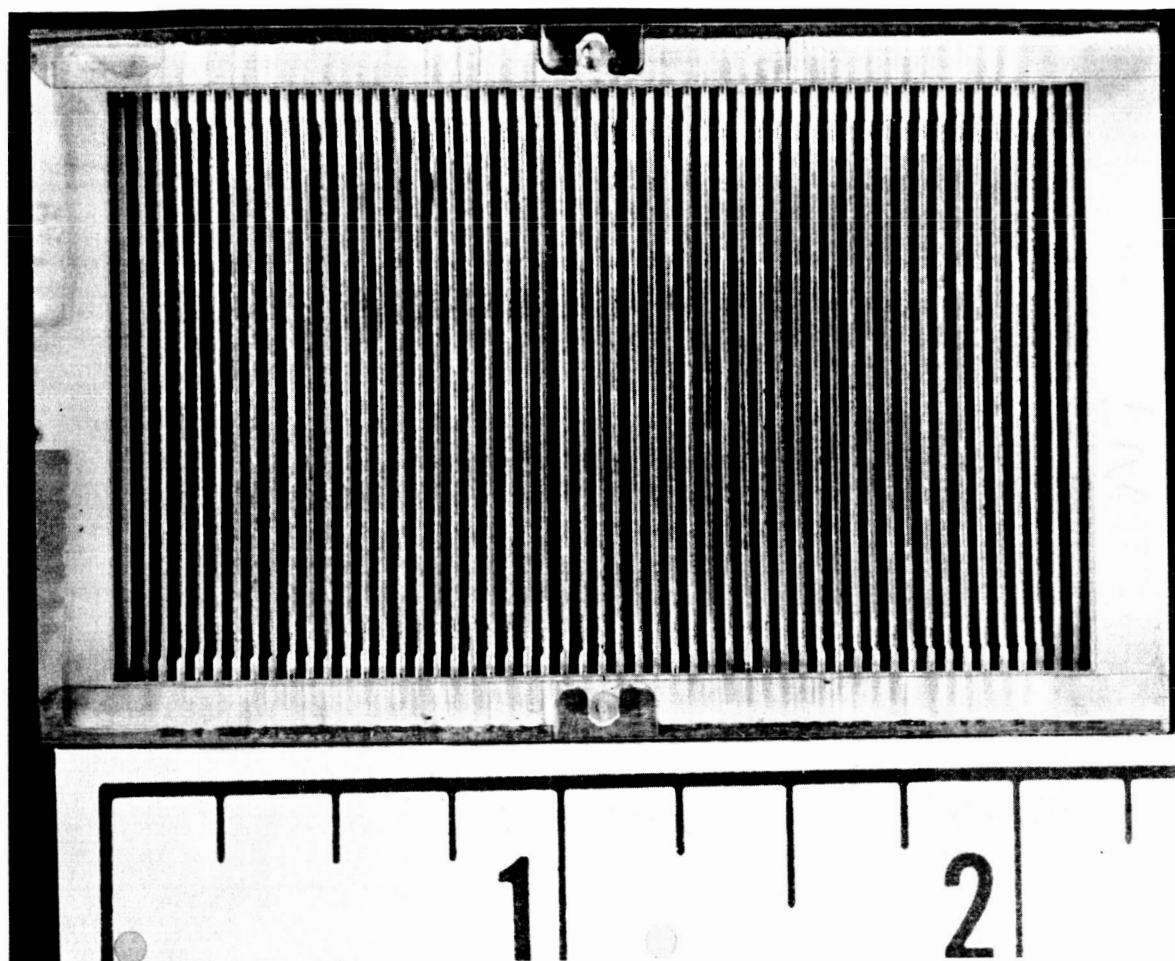
Figure 51. Nickel grid used in Life Test
No. 6 (downstream side).

It is difficult to explain the degradation in emitter performance associated with the boiler refills since both were carried out in exactly the same manner as in the fill prior to initial testing. One explanation might be that as the boiler ran dry the concentration of cesium oxide increased. At the same time the boiler temperature was raised well above its normal average – perhaps to a level where the vapor pressure of cesium oxide becomes significant. This would cause a slow oxygen feed through emitter and giving rise to the remnent oxygen condition.

The unusually high drain current throughout the test remains something of a mystery. Electron emission from the nickel itself of this amount would require grid bar temperatures in the neighborhood of 1300°K according to Wilson's[10] measurements of electron emission of cesiated nickel. This temperature could only be achieved by a large direct interception of the beam. While it is indeed true that the erosion pattern of the grid would indicate over-expansion due to an extremely high grid frame temperature this explanation hardly seems credible in the light of prior measurements of both grid frame and grid bar temperatures.[2] A more likely explanation appears to be simply the accumulation of a low work function substrate on the grid rails.

7.8 SUMMARY OF LIFE TEST DATA

Table XII summarizes the important data associated with these life tests. The first ten rows of this table essentially duplicate the information obtainable from Figure 38, 42, 44, 47, 48 and 49. The last three provide an insight into the integrated performance.

The significant drop in average neutral fraction from 7.15% (corrected) in Life Test No. 3 to 3.3% in during Life Test No. 4 demonstrates the fact that sputtering (or electropolishing) the surface to improve the microstructure can be permanently beneficial.

The high average neutral fraction during Life Test No. 6 should not be compared unfavorably with that of Life Test No. 4. The fact that neutrals averaged 2.1% during the first 120 hours proves that contaminents if present can be basically harmless as long as oxygen is absent.

113

TABLE XII

Performance Summary of Life Tests

Life Test No.:	1	2	3	4	5	6
Emitter:	G-4-2	G-6(b)	G-6(b)	G-6(b)	G-6(b)	G-6
Grid Mat'l:	Cu	Cu	Cu	Cu	Ni	Ni
I_{beam} Ave*, MA:	225	225	220	220	230	225
I_{drain}, MA:	5**	2-10	12.5	1-13***	1-4	5.25
Measured ⎧ START:	4.5	3.5	6.3	1.3	.68	.8
Neutrals ⎪ MAX:	23	4.5	6.3	1.5	10(@250MA)	3.7
(Percent) ⎨ MIN:	2.0	3.5	2.1	.35	.68	.45
⎩ FINISH:	4.2	4.2	3.6	1.0	2.4 (1.19 after acetylene)	3.7
Average Corrected Neutral fraction (%)	16	12.4	7.15	3.3	7.4	6.7
Duration of Average (hours)	486	172	387	313	104	524
Equivalent hours @ 1% neutrals	7800	2140	2760	1040	770	3517
Condition of Grid	Worn Out	----	----	Ireg. Optic Erosion	Good	V. Good

REMARKS   Test No. 1 - Most of test conducted with leak in feed line

             Test No. 2 - Very stable operation

             Test No. 3 - Very stable operation

             Test No. 4 - Failure due to poor optics

             Test No. 5 - Very stable operation

             Test No. 6 - Excellent electrode and emitter performance. Neutrals increased after each refill of boiler.

* I_{beam} = 225 MA yields J = 15 MA/CM^2

**   Drain increased to 37 ma (ave) after leak in feed line developed.

*** Increased to 13 MA after leak dev. in boiler. After repair drain did not exceed 2.8 MA.

The contamination problem led to one important advantage here. These are basically accelerated life tests because of the high neutral fraction. This is most forcefully demonstrated by Life Test No. 1 where the average corrected neutral fraction was 16%. Had the contaminants not been present, presumably the neutral fraction of G-4-3 (see Figure 24) would have been obtained. At this level (.9%) Life Test No. 1 is equivalent to 17,300 hours operation with a nickel grid (assuming that the measured sputtering yeild or nickel* is one-half that of copper).

7.9   CALCULATION OF ELECTRODE LIFE FOR THE TRW-CONTACT ENGINE

In appendix I the basic relationships are derived for calculating the electrode life of an ion engine with either accel-decel, space-charge limited, or emission limited operation. The intention here is to calculate electrode life for the TRW-Systems optics for the perveance limited (i.e. space charge limited case) using the equations and computed curves of appendix I. The constants selected yield a conservative - or minimum estimated electrode life which is useful in correlating and projecting the life test data.

Using the following respective charge exchange cross section and sputtering yield of nickel:

$$\sigma = 7.11 \times 10^{-14} \, V^{-.125} \, cm^2$$
$$S = .00195V^{.825} \, gmsNi/gmCs$$

(where V is the accel voltage)

and using a value for ψ_0 of .3 which is twice that which is obtained using Brewers[11] computer calculating of charge exchange ion escape probability, equations 11, 31, and 38 of Appendix I yield the expression for electrode

*   see sputtering data in sec. 8.2.

115

life, L, of

$$L = \frac{1.6}{\alpha J^2 V_p^7 (1 + 9.85w/J)} \text{ hours}$$

assuming 30% erosion as the end life.

V_p = accel voltage

α = true neutral fraction

J = ion current density in amps/cm^2

w = equivalent width of a flat across each flute peak accounting for machining tolerances

Life calculations for emission limited operation at 15 ma/cm^2 and a Ni grid are plotted in Figure 52 for two cases of imperfect optics, w = .0005" and .0001". These two values roughly represent present and projected state of the art in emitter fabrication accuracy.

A more general set of curves is plotted in Figure 53 where the maximum allowable neutral fraction to guarantee various specified life times is plotted as a function of current density with an accel voltage of 2000 volts. In this case no accel-decel is required at current densities at or below .025 amp/cm^2 with the TRW-System engine.

These estimates are probably conservative for the following reasons:

(1) Neutral distribution peaks in the forward direction should yield 50% less erosion.

(2) The charge exchange cross-section used is probably 1.5 times the true value.

(3) The factor ψ_0 is probably much closer to the .15 value than the .3 which was used in this calculation.

(4) A considerable fraction of the sputtered grid material is redeposited on the grid by being re-evaporated from the emitter.

(5) Our life tests have repeatedly demonstrated that much more than 30% of the grid than can be eroded before failure.

The life test data summarized in Table XII can be used as a cross-check upon the accuracy of these calculations. For example if we consider the equivalent erosion from the first life test and assume that it would

116
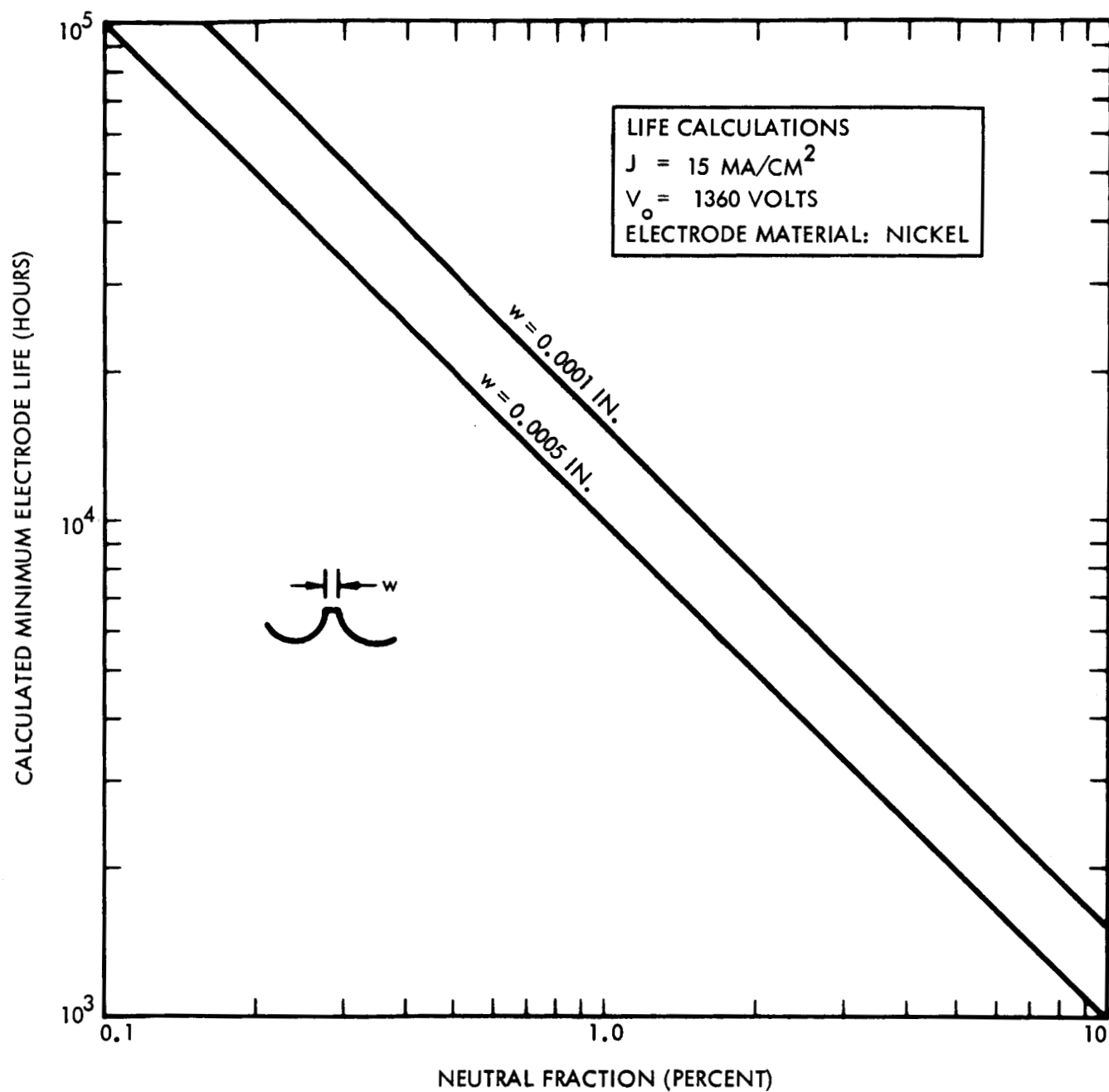
Figure 52. Calculated electrode life (at 15 ma/cm^2) vs neutral fraction for the TRW Systems engine (two cases of imperfect optics).
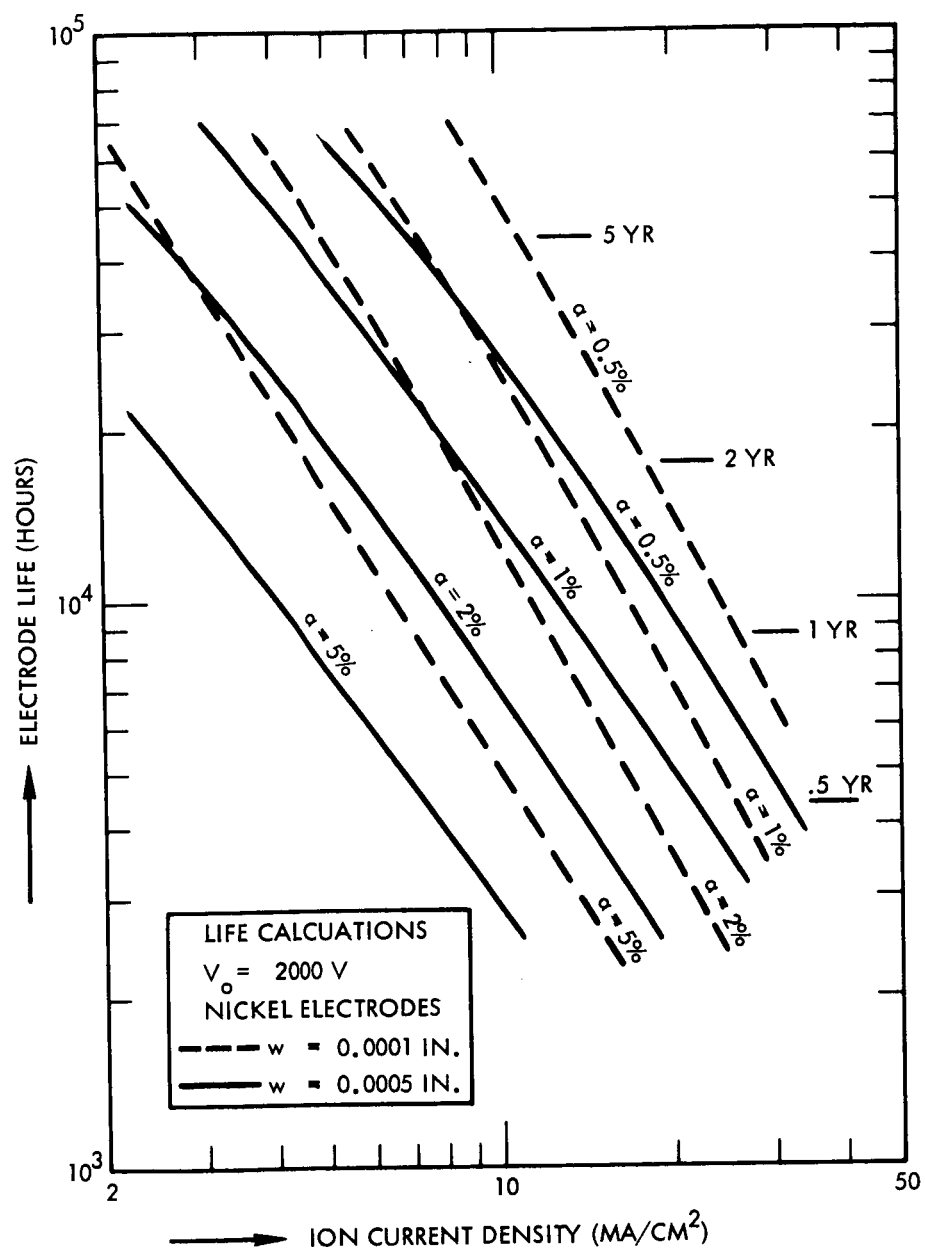
Figure 53. Minimum estimated electrode life as
a function of current density for two
cases of imperfect optics and various
α's.

118

have functioned twice as long with a nickel grid the equivalent operating time at .3% neutrals is 53,000 hours. This is in fairly good agreement with the calculated life curves of Figures 49 and 50.

7.10 IONIZER DURABILITY

The useful life of an emitter can be limited by any one or all of the following:

1. Volumetric sintering (gradually reducing the permeability);
2. Surface sintering (leading to a reduced pore count);
3. Etching of the emitter surface by oxygen or water vapor; and
4. Emitter erosion by back bombardment of negative ions.

The first 3 effects are vastly influenced by the presence of impurities in the tungsten and/or gases evolved from the cesium.

Sintering rates vs temperature have been measured at high temperatures and extrapolating to the normal operating values by Kirkpatrick[4] and others[12]. They assume a straight line relationship in a log time vs 1/T plot. Kirkpatrick's results for various size powder lots are illustrated in Figure 54. As is to be expected the smaller the powder size the shorter the life at a given operating temperature. The 3.7 micron powder curve would be a good approximation of Hughes' 324-S material. It should be noted this particular end life is calculated on the bases of a 50% reduction in permeability and is therefore quite conservative.

The post examination of emitter G-6 showed some evidence of surface sintering but nevertheless a good general overall appearance after 650 hours of operation. The photo of the emitter surface is illustrated in Figure 55. By way of contrast a photo of a early emitter operated for some length of time in a water vapor environment is included in Figure 55 (inset).

The back bombardment of the emitter surface by negative ions can be a life limiting factor for the emitter. Early in 1962 Krohn[13] measured negative ion formation from cesium ion bombardment of copper, beryllium, and several other materials.

119
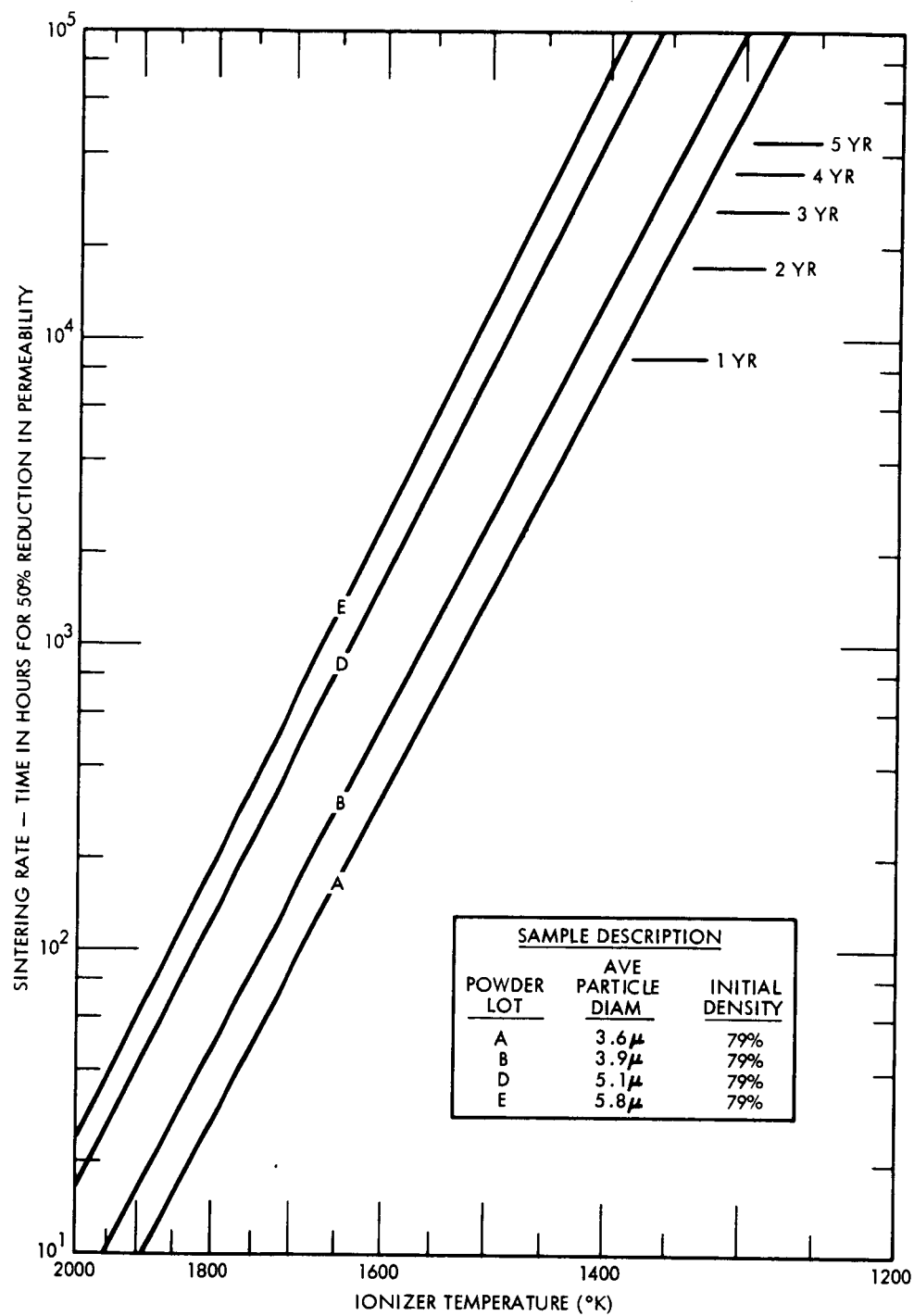
Figure 54. Relationship between ionizer lifetime and temperature for various spherical tungsten powder lots.
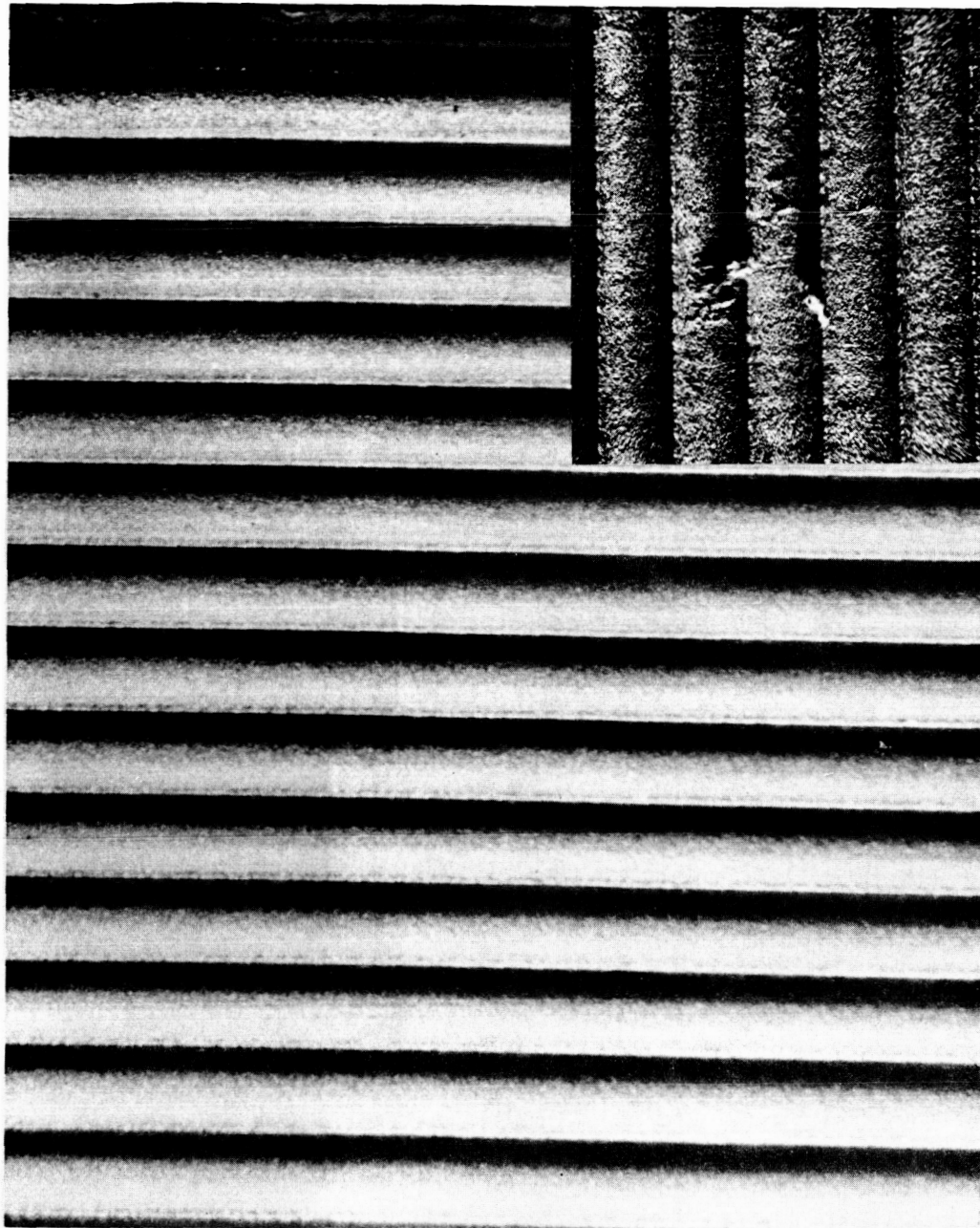
Figure 55. Emitter G-6 after 650 hours of operation (including Life Test No. 6). Inset: 1964 emitter after approximately 200 hours of operation.

Krohn found that the cesium coverage of the bombarded material was an important factor. In fact he found that negative ions from the copper disappeared as the copper temperature was raised above a certain point. This discovery was preceded by several cases of noticeable emitter erosion in an engine configuration using copper grids which were cooled by conduction to a base plate.

The grid bar temperature associated with the present grid structure has been measured on several occasions and found to be in the 800 to 1000°K range. There has been no evidence of negative ion erosion with this grid. It is, in fact, interesting to note that the "remnant-oxygen" characteristic of the contaminated emitters has shown quite conclusively that negative ions are not generated at the grid. On several occasions "clean" emitter operation could be recovered by reducing the grid bias to zero. The only mechanism for this type of clean-up is that of negative ions generated at the collector (or downstream in the beam) drifting back to the engine and bombarding the emitter surface. Obviously if negative ions were being formed on the grid this type of bombardment would be going on continuously and the "remnant-oxygen" condition would not occur.

There is a good possibility that other engine designs have been subject to negative ion erosion due to operating the electrodes at too low a temperature. In general, high drain currents (excepting a direct interception problem) indicate a high probability of negative ion erosion.

122

8. LIFE VERSUS EFFICIENCY – PRESENT POTENTIAL OF THE CONTACT ION ENGINE

8.1 INTRODUCTION

The mission duration for a given electric propulsion application is generally either specified or flexible within fairly narrow limits. Consequently the electrode durability requirement is known and from the known characteristics of an ionizer a maximum allowable current density is selected. Engine efficiency of the contact engine will then be largely determined by the ionizer heating requirement. In this section recent improvements in the thermal efficiency of the TRW-Systems engine are described. The efficiency potential of this design is estimated using several of the better ionizer materials as an example.

8.2 THERMAL EMITTANCE AND SHIELDING EFFICIENCY MEASUREMENTS

During the life test of G-6 which have been electropolished according to the methods described above, the heating requirements was 190 watts at 1500°K. This remained constant during 560 hours of operation and compares with 270 watts required for emitter G-6(b) tested earlier and which had not been electropolished.

The emissivity of G-6 was determined by measuring the heating requirement of the emitter, first with no grid in place and secondly with a grid containing a single tungsten sheet spaced .02" from the emitter, and having the same dimensions as the emitter (1.2 x 2.08 inches). By measuring the temperature of the tungsten sheet the frontal radiation can be calculated assuming the tungsten sheet has an emissivity as published in the literature.

The method of calculating emissivity from this data is discussed ref. (1). The results from the G-6 data indicated an emissivity of .2. The published emissivity of tungsten is .192 at this temperature.

These calculations also show that, with a nickel grid in place, the frontal radiation was 87 watts or 5.7 watts per cm^2 of projected ion beam. The thermal shielding efficiency, defined as the ratio of frontal to total radiation loss, was therefore only 46%.

123

Because of the significance of these measurements in terms of power efficiency for the ion emitter, TRW Systems undertook an in-house investigation to check the reliability of the data and determine where shielding efficiency could be improved.

These experiments were conducted with a reject emitter whose heating requirements were measured before and after electropolishing. A total of 32 different measurements with different shielding configurations reconfirmed the emissivity measurements above for freshly electropolished porous tungsten. Further, it was found that thermal efficiency could be increased to 60% fairly easily.

A more definitive experiment was performed by electropolishing emitter G-7-3 (Hughes 324-S material) and using a shielding configuration consisting of rhodium heat shield boxes close to the emitter plus a 1/4" thick layer of fibrafrax and a final outer covering of molybdenum. The measured heating requirement was 137 watts at $1500°K$.

This power requirement is plotted as a function of temperature in Figure 56 and labelled "present heating requirement". Comparing this with the power requirements of the various emitters tested under this contract (also plotted in Figure 56) shows the significant improvement which has been achieved. Further improvements should lead to the "future heating requirement" curve which represents a thermal shielding efficiency of 72% (i.e. frontal radiation accounts for 72% of the total loss).

The heat shielding experiments also isolated various sources of heat loss. Table XIII contains power inventories for the cases of:
(1) the engine configuration used for Life Test #6;
(2) the present improved design; and
(3) a projected future design which should be fairly easily achieved.
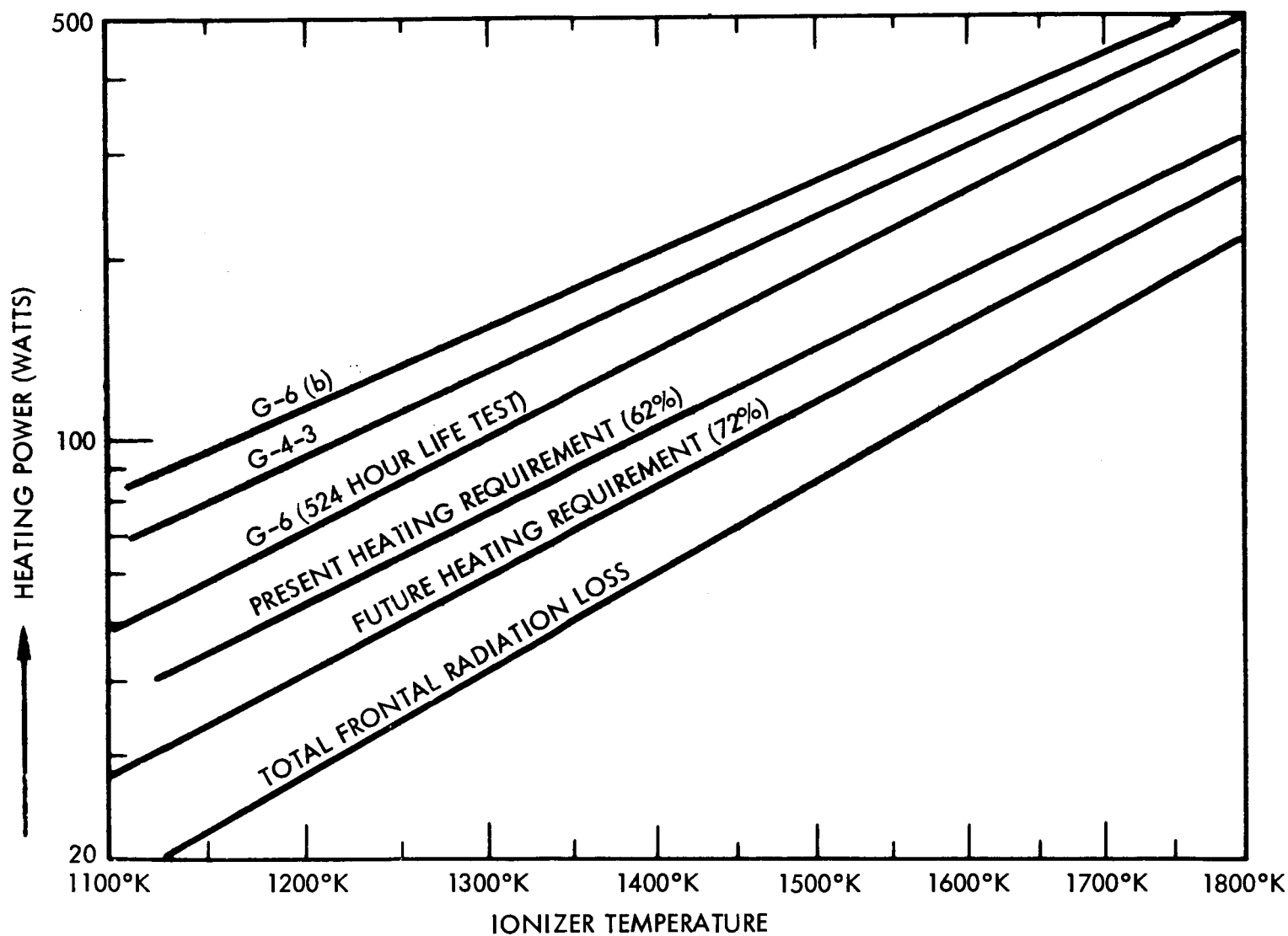
Figure 56. Past present and future heating requirements for the TRW Systems 1" x 2" contact engine (15.3 cm^2).

TABLE XIII

TOTAL HEATING REQUIREMENTS OF 3 ENGINE DESIGNS (at 1500°K)

THRUSTOR DESIGN	1) G-6 Engine	2) Present	3) Future
Frontal Radiation (with nickel grid)	87 watts	87 watts	87 watts
Unshielded side Rad.	25 watts	0 watts	0 watts
Conduction thru supports	15	5	5
Feed Tube Conduction	15	5	5
Heater end losses	9	8	5
Radiation thru shields	39	32	10
Total	190	137	112
Shielding Efficiency	46%	63%	71.5%
Watts/cm^2 of ion beam	12.4	9.8	7.35

We have selected three examples in order to further emphasize the influence of the latest improvements in shielding efficiency, lower emissivity of the emitter and lower critical temperatures (due to the electropolish operation) on the engine efficiency.

In all cases the "present heating requirement" shown in Figure 56 is assumed. Current densities such as that αJ^2 is constant are selected to provide a constant electrode life. Finally a flat along a flute peak of .0001" is assumed. This is definitely within the state of the art even though our present electropolishing procedure does not meet this specification.

126

The results of these calculations are summarized in Table XIV.
In case (1) the "remnant-oxygen" characteristics of G-4-1 are used in
an operating temperature current density and neutral fraction are
selected so as to yield a minimum electrode life of 15,000 hours. In
order to achieve this, an operating temperature of 1600°K is required
and a current density of not more than .01 amps/cm^2.

In case (2) the engine data of G-4-3 is used where the corrected
neutral fraction is less than 1% @ .015 A/cm^2. Thus the same (or greater)
electrode life is obtained (compared with G-4-1) at 50% higher current
density. Because of the lower operating temperature requirements an even
lower heating requirement is necessary. This data basically represents
present engine data.

In case (3) we assume the low neutral fraction and operating
temperature of the button measurements for 324-S material.

Table XIV is dramatic evidence of the improvements in emitter
efficiency resulting from: (1),elimination of the remnant-oxygen effect;
(2), reduction of neutral fraction by improving the surface micro-
structure by either the sputtering or electropolishing the surface; and
(3) the improved emissivity associated with the electropolishing
operation.

Case (2) shows a doubling of electrical efficiency over that of
case (1). This is due to the elimination of the remnant-oxygen contam-
ination. In both cases we have used engine data for α vs T character-
istics of G-4 material. Case (3) shows the additional efficiency
improvement obtainable if the low neutrals and operating temperatures
of the button data can be duplicated by a large emitter such as G-7-3.
Note that the electrical efficiency has increased from 67 to 80.6% and
the electrode life has also increased by almost 15%.

8.4 DURABILITY VERSUS EFFICIENCY FOR VARIOUS SELECTED IONIZER MATERIALS

In order to estimate the present state of the art of contact ion
engines we have calculated the ev/ion requirement for several of the better
materials which have been tested in the past two years. The present

TABLE XIV

PRESENT EFFICIENCY AND ESTIMATED ELECTRODE LIFE
FOR THE TRW-SYSTEMS
CONTACT ION ENGINE

CASE NO.	(1)	(2)	(3)
Emitter No.:	G-4-1	G-4-3	G-7-3
Ionizer Temperature	1600°K	1450°K[1]	1425°K[3]
Heater Requirement	350[4]	119 watts[4]	110 watts[4]
Beam Current	115	230 MA	306 MA
Grid Drain	2	3 MA	3 MA
V_o	1200V	1200V	1800V
V_g	160V	160V	200V
Power Inventory			
Beam	186	276	549
Ionizer Heater	350	119	110
Drain Power	2	4	6
Neutralizer (including injection losses)	8	12	16
TOTAL	546	411	681
Loss in E/V per ion	2320	586	431
Electrical Efficiency(%)	34	67	80.6
Thrust (lb)	2.02×10^{-3}	3×10^{-3}	4.8×10^{-3}
P/T (Kw/lb thrust)	270kw	137	141.5
I_{sp} of beam (seconds)	4260	4260	5200
I_{50} (seconds)	5940	3040 seconds	2560 seconds
P/T min. (KW/lb thrust)	255	131	110
Neutral fraction (%)	3.0%[1]	1.0[2]	.3[3]
Electrode Life	15000 to 45000hrs	15000 to 45000hrs.	22-66,000hrs.

Notes: (1) From engine data of Figure (17). – Neutral fraction = 3 x measured value

(2) From engine data of Figure (24) – Neutral fraction = 3 x measured value.

(3) Button data for Hughes 324-S material (see Figure 15).

(4) "Present heating requirement" Figure 56.

efficiency is used and operating temperatures are selected well above critical temperature. The results are plotted in Figure 57. The ev per ion includes 1% drain current allowance and 52 ev/ion for a neutralizer in addition to the heating requirement.

Neutral fraction is plotted as a function of current density in Figure 57 for these materials. This figure also shows minimum electrode life curves of .5, 1.0, 2.0, and 5.0 years when the emitter has .0001" flats on the flute peaks.'

Examination of these curves shows that if operating current density is selected so as to yield a one year electrode life then Astromet (1-10), G-1, G-4, E-4 and 324-S materials would have an ev/ion requirement substantially below 600ev/ion. This 600 ev/ion figure is equivalent to the present efficiency of the cesium bombardment engine[14].

The variation of engine efficiency as a function of ion beam specific impulse is plotted in Figure 58 for two cases believed to represent present and future technology. With a nickel grid, thrustor durability would be sufficient for most missions even at this high level of current density - and efficiency.

IONIZATION EFFICIENCY

LIFE VERSUS J

1 ASTROMET
2 G6
3 E4
4 G1
5 324-S (SPUTTERED)
6 324-S (POLISHED)
7 G4
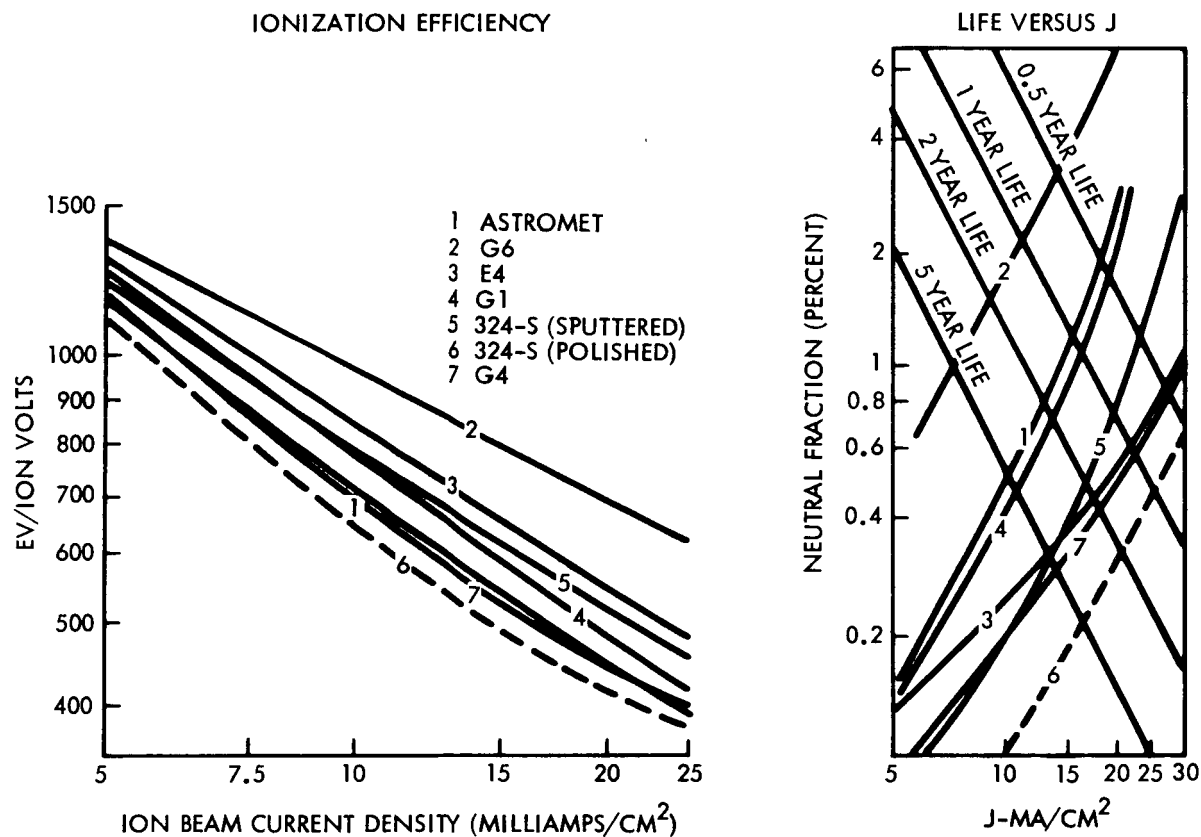
Figure 57. Efficiency and electrode life for
the TRW Systems engine as a function
of current density for various emitter
materials. Ev/ion calculations assume
the present heating efficiency, a 1%
drain durrent, and 52 ev/ion for neu-
tralization. Life curves assume
w = .0001" and a nickel electrode.

129
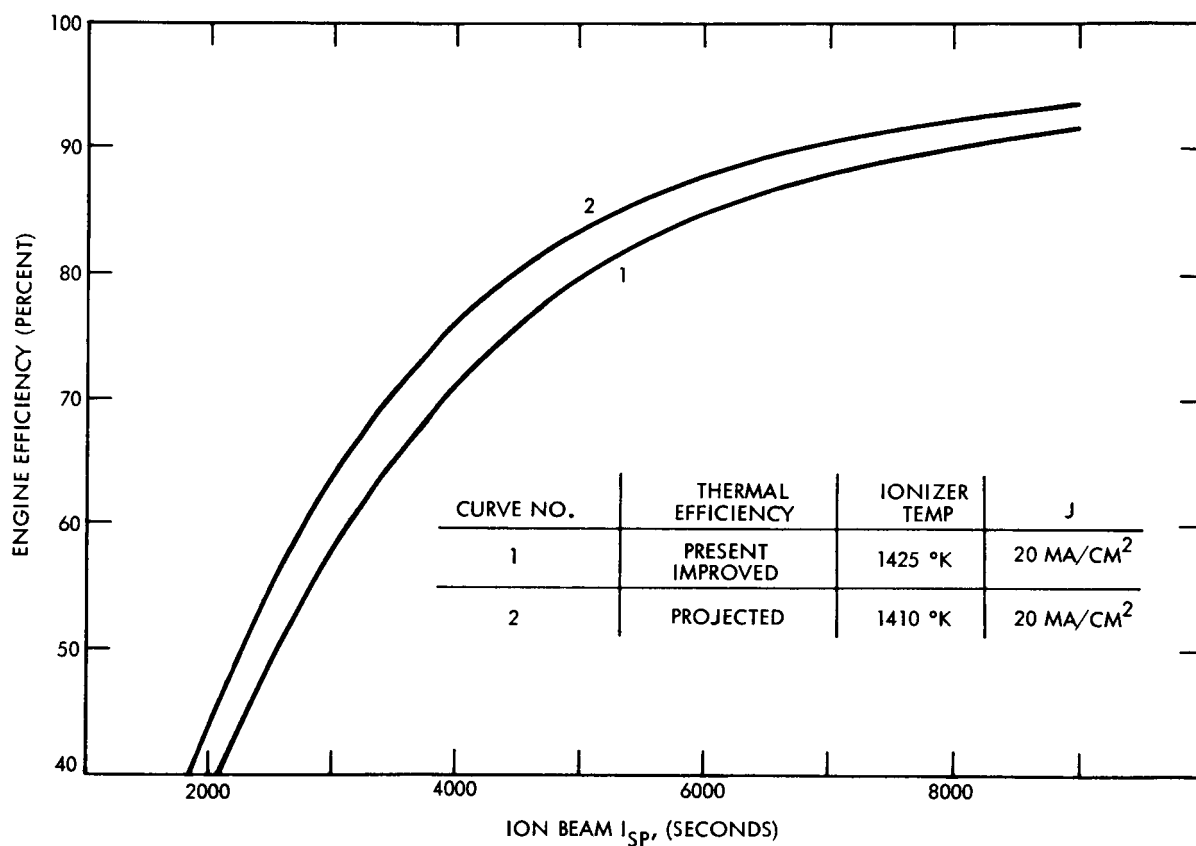
Figure 58. Present and projected efficiency of
the TRW Systems contact ion engine based
on the button ionizer data for Hughes 324-S
material. Electrode life should be 1 to 3
years at 20 ma/cm^2.

APPENDIX I.

ELECTRODE LIFE CALCULATIONS FOR
ION ENGINE OPERATION IN ANY OF THE FOLLOWING MODES:
ACCEL-DECEL, SPACE CHARGE LIMITED, AND EMISSION
LIMITED

1.   INTRODUCTION

The accelerator electrode of an ion engine is life limited by charge exchange erosion even when the focussing optics are perfect — i.e. there is no direct interception of the primary ion beam. In fact, thruster durability is largely a function of this element's lifetime in present day ion engines.*

Given a choice of scaling the physical size of thruster up or down to improve electrode life one instinctively selects the larger structure as the more durable. Surprisingly, this is usually the wrong choice. In fact, the design equations developed in this Appendix show that increasing the electrode size by a factor of three can lead to a decrease in electrode life by a factor of eight!

Proper engine scale for a particular ion engine mission is a relatively simple matter once the ground rules have been established. The most important rule is:

> "Maximum electrode life is achieved when the thruster is operated
> in the space-charge limited mode. Depending to some extent upon
> the choice of electrode material shifting the specific impulse down
> by using accel-decel or up by emission limited operation is usually
> accompanied with a severe reduction in electrode life."

While the basic equations developed in this Appendix specifically refer to the contact engine they can also be used for estimating the electrode life of the bombardment type engine. Only the rules regarding imperfect optics need a slight modification.

*   Until recently the neutralizer electron sources were comparably life
limited. However, Electro-Optical Systems' development of a "Plasma
Bridge Neutralizer"(15) has yielded efficient neutralizers with a much
greater durability potential.

The present state of the art for the contact engine is such that in the range of practical diode spacings (.5 mm and up) contour optics can be generated with sufficient accuracy that all ions leaving the emitter are directed past the accelerator electrode system with zero interception with the exception of those leaving the very tips of the contour flutes (where the optics fail). The presently accepted method of minimizing erosion from this source — at least in the parallel slit geometry — is that of having this region fabricated from solid rather than porous tungsten. Consequently the only ions originating here are due to neutral cesium reflected back by the accel electrode. Attempts to eliminate ion emission from this region by cooling the tips or doping them with low work function material have, so far, proved unsuccessful.

In the first portion of this analysis (Section 2 through 9) we calculate electrode life relative to engine scale with the smallest engine operating in the space charge limited simple diode mode and the larger models operating in the accel-decel mode (which is necessary to achieve the same current density and beam I_{sp} as the small engine).

When the electrode life of a particular engine is defined in terms of its operational specific impulse (Section 11) the penalty for either accel-decel or emission limited operation is accurately identified. At the same time it is obvious that the life penalty for the larger engine would be less severe if it were also operated emission limited.

Since this required a higher specific impulse of the ion beam the final section (Section 12) briefly reviews the penalties associated with operating an engine at other than the optimum I_{sp} of the mission.

2. THE SCALING MODEL

Two engine modules are illustrated in Figure 59. The larger unit with an accel spacing x_a requires an accel-decel ratio D in order to achieve the same ion current density (and net ion velocity) as the smaller model which has a spacing x_o. Other dimensions are assumed to scale in the same proportion as the spacing ratio, R, so that the ion optics are the same for either case.

For space charge limited flow we have (for cesium)

$$J = 4.7 \times 10^{-9} V_a^{3/2}/x_a^2$$
$$= 4.7 \times 10^{-9} V_o^{3/2}/x_o^2 \tag{1}$$

From (1) we obtain

$$D = V_a/V_o = (x_a/x_o)^{4/3} = R^{4/3} \tag{2}$$

The location of the decel electrode is defined as x_d further downstream from the accel electrode. Since all charge exchange ions created in this region cannot escape and hence will strike the accel electrode x_d will also be minimized to yield space charge limited flow. Thus

$$V_d/V_o = (V_a - V_o)/V_o = D - 1$$
$$x_d/x_o = (D - 1)^{3/4} = (R^{4/3} - 1)^{3/4} \tag{3}$$

The potential distributions for these two engines are plotted as a function of x in Figure 60. The dashed curve represents the small engine where D = R = 1. In practice such a potential distribution allows electrons from the neutralizer to stream back to the emitter. To prevent this a minimal negative (bias) voltage on the accel electrode with respect to the

133
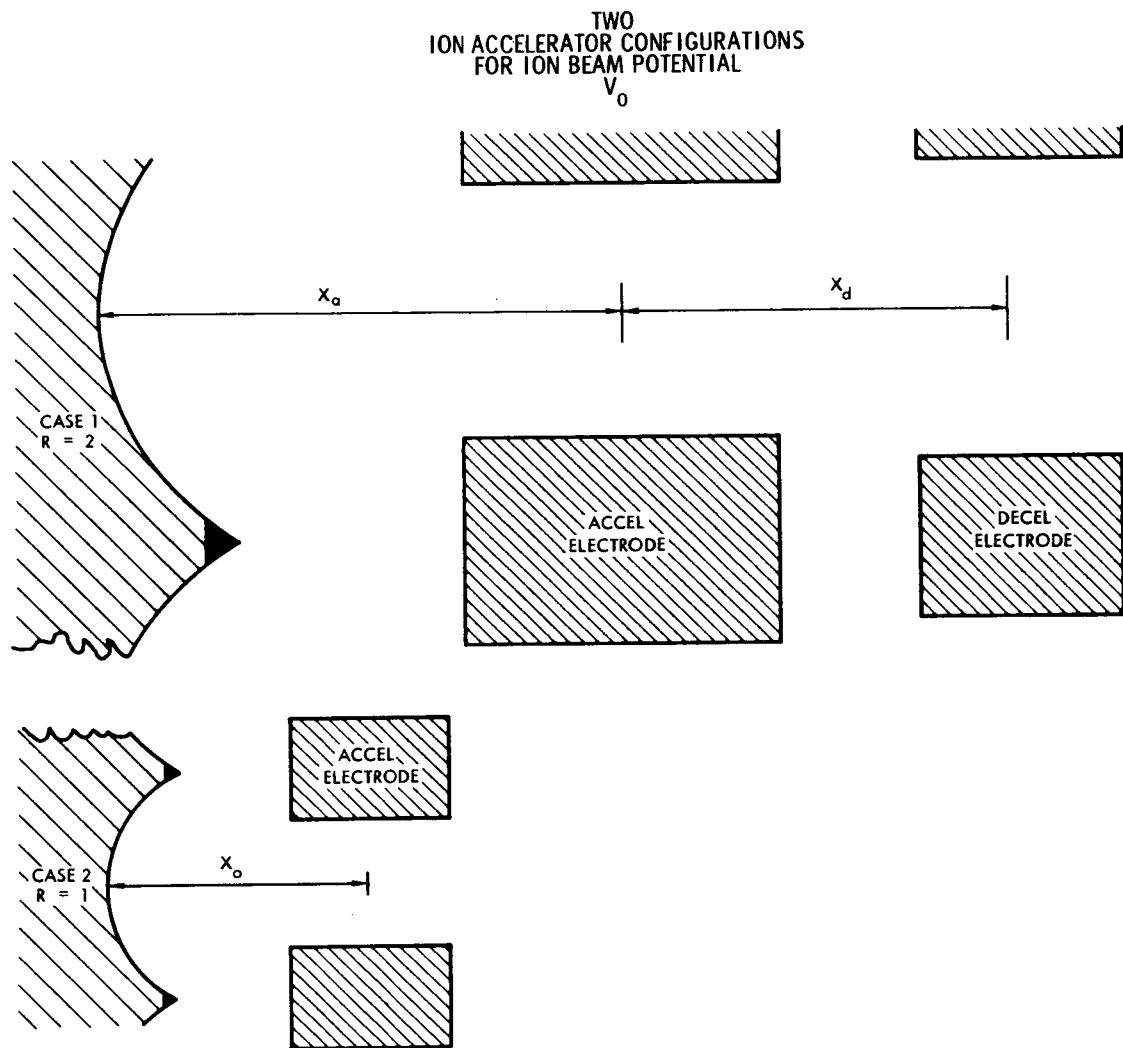
Figure 59. Engine models illustrating the
scaling law.

POTENTIAL DISTRIBUTION

$$\frac{V_a}{V_o} = D \qquad (D = R^{4/3})$$

	CASE 1	CASE 2
V_a	$2.52\,V_o$	V_o
V_d	$1.52\,V_o$	O

CASE 2 (R=1)

CASE 1 (R = 2)
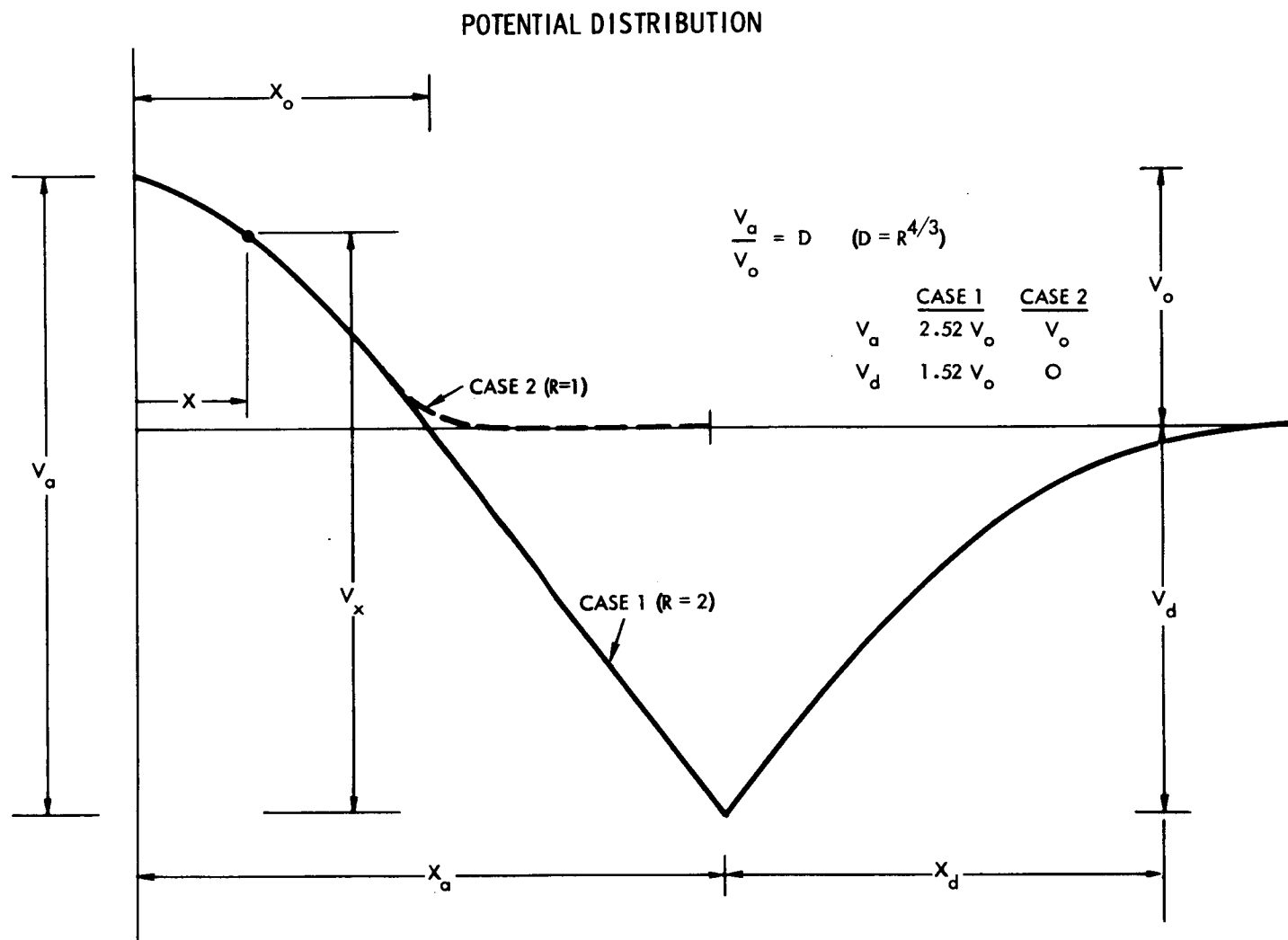
Figure 60. Potential distribution in the accel
and decel regions.

135

neutralizer (and ship) potential is required. For the TRW Systems ion optics
this must be 5 to 10% of the accel voltage which corresponds to

$$1.05 \lesssim D \lesssim 1.1$$

Experience has shown that fairly high accel-decel ratios can be used
without the requirement of a decel electrode. The upper limit is reached
when the beam divergence becomes excessive or the beam becomes unstable because
of neutralization problems. Experimental data indicates this limit to be

$$D_{max} \simeq 3$$

For the purposes of this analysis, we will assume that when decel
electrodes must be added to increase D beyond D_{max} the only change which will
occur will be an increase in neutral density.* Theoretical considerations
tend to confirm the conclusion that the potential distribution will be effectively
the same with or without a decel electrode.

---

*   Neutrals which would normally escape are intercepted by the decel
     electrode and reflected back towards the engine thus raising the
     neutral density.

136

3. ION ENERGY RELATIONSHIPS IN TERMS OF x

The probability that a primary (beam) ion will transfer its charge to a neutral atom at position x is a function of the primary ion energy, $V_b(x)$. The sputtering damage which the charge exchange ion can do if it strikes the accel electrode is a function of its energy at impact.

If we define the potential at x as V_x such that it obeys Child's law (for space charge limited flow)

$$V_x = bx^{4/3} \tag{4}$$

where   b = constant for a given current density and ion mass

$$= (J/4.7 \times 10^{-9})^{2/3} \text{ for cesium ions.}$$

As illustrated in Figure 60, V_x is the potential at x referred to the source in the accel region and referred to the decel electrode (or ship) potential in the decel region. In both cases x increases in the direction of the accel electrode.

The primary ion energy at x is then

$$\left. \begin{array}{l} V_b(x) = V_x = bx^{4/3} \text{ in the accel region} \\ \\ = V_0 + V_x = b(x_0^{4/3} + x^{4/3}) \text{ in the decel region} \end{array} \right\} \tag{5}$$

The charge exchange ion will have an energy $V_c(x)$ when it has been accelerated into the accel region (or the electrode itself), where

$$\left. \begin{array}{l} V_c(x) = (V_a - V_x) \\ \\ = b(x_a^{4/3} - x^{4/3}) \text{ in the accel region} \\ \\ = b(x_d^{4/3} - x^{4/3}) \text{ in the decel region.} \end{array} \right\} \tag{6}$$

4.   CHARGE EXCHANGE EROSION

The sputtering damage — or mass erosion rate — from ions created in the region between x and x + dx will be

$$d\dot{m}_x = J\ (1 - P_x)\ \sigma_x\ n_x\ S_x\ dx/(e/m) \tag{7}$$

in grams per second when

P_x = probability that a charge exchange ion created at x can be accelerated into the ion beam without striking the accel electrode.

σ_x = charge exchange cross-section for primary ion energy measured in cm^2.

n_x = neutral density at x in atoms/cm^3.

S_x = grams of electrode material removed per gram of interception ions.

And e/m = charge to mass ratio in coulombs per gram

= 722 for cesium.

Integration of (7) over all values of x where P_x is less than unity will determine the mass erosion rate (and life) of the accel electrode. This requires knowledge of the values of P, σ, n and S as a function of x. The escape probability, P_x, is high for small values of x in the accel region and decreases to zero at approximately $x = x_o$. The escape probability in the decel region is zero. Brewer's[11] computer calculations of the escape probability for H.R.L.'s parallel slit geometry can be used here.

The sputtering yield varies with both ion energy and electrode material. Published data for copper[16,17,18] are plotted in Figure 61. Note that while there is disagreement concerning the magnitude of the sputtering yield the slopes of the curves are approximately the same up to the energies of about 3 1/2 KV. From the dashed curve in Figure 61, we observe that sputtering yield can be represented reasonably accurately over a wide energy range as a power function of voltage. That is

$$S_x = S_o V_c^{\ q} \tag{8}$$

SPUTTERING YIELD, Y, (ATOMS/ION)
VS
ION POTENTIAL
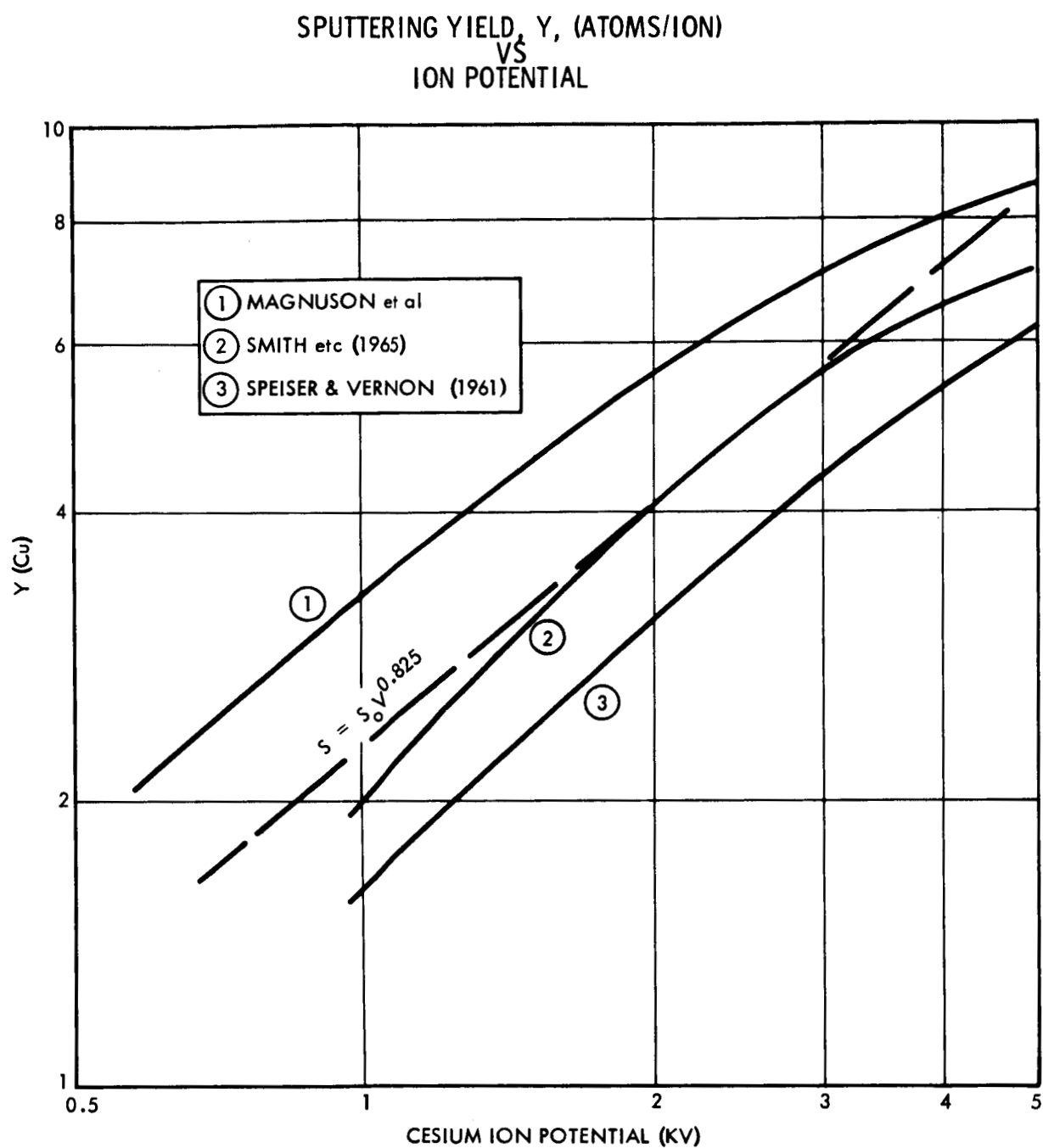
Figure 61. Sputtering yield of copper as a
function of ion energy.

139

The charge-exchange cross-section data can also be expressed as a power function of voltage as evidenced by the published data[18,19] curves of Figure 62. Thus we write

$$\sigma_x = \sigma_o \, V_b^{\,p} \tag{9}$$

The neutral density can be considered essentially constant within either the accel region or the decel region. The latter ($\dot{n}_d$) will be smaller in value than the former (n_o) due to the reflection factor of the accel electrode.

Defining $\dot{m}_a$ as the mass removal rate of the electrode due to charge exchange ions formed in the accel region, and $\dot{m}_d$ as that due to charge exchange ions from the decel region, we have from (7), (8) and (9)

$$\dot{m}_a = \int_o^{x_a} d\,\dot{m}_x = k_o \int_o^{x_a} (1 - P_x) \, V_b^{\,p} \, V_c^{\,q} \, dx \tag{10a}$$

and

$$\dot{m}_d = \int_o^{x_d} d\dot{m}_x = k_d \int_o^{x_d} V_b^{\,p} \, V_c^{\,q} \, dx \tag{10b}$$

where

$$k_o = J \, \sigma_o \, n_o \, S_o / (e/m) \tag{11}$$

and

$$k_d = k_o (n_d / n_o) \tag{12}$$

140

CHARGE EXCHANGE CROSS-SECTION, σ^-
FOR Cs
VS
ION ENERGY

$$\sigma = 7.11 \times 10^{-14} V^{-0.125} CM^2$$

$$\sigma = 13.05 \times 10^{-14} V^{-0.26}$$

① SPEISER & VERNON (1961)

② MARINO et al (1962)

$\sigma \; (cm^2 \times 10^{14})$

V - CESIUM ION POTENTIAL (KV)

Figure 62. Charge exchange cross-section as
a function of ion energy.

141

5. MASS REMOVAL RATE BY CHARGE EXCHANGE IONS FORMED IN THE ACCEL REGION

Equation (10a) can be evaluated by substituting the appropriate functions of x for V_b and V_c as defined by Eq. (5) and (6). That is

$$\dot{m}_a = k_o \int_o^{x_a} (1 - P_x)(b \, x^{4/3})^P (b \, x_a^{4/3} - b \, x^{4/3})^q \, dx$$

$$= (b \, x_a^{4/3})^{p+q} \cdot k_o \int_o^{x_a} (1 - P_x)(x/x_a)^{(4/3)P}[1 - (x/x_a)^{4/3}]^q \quad (13)$$

Substitution of $y = x/x_a$ into (13) and from the definitions of Eqs. (2) and (4), (13) yields
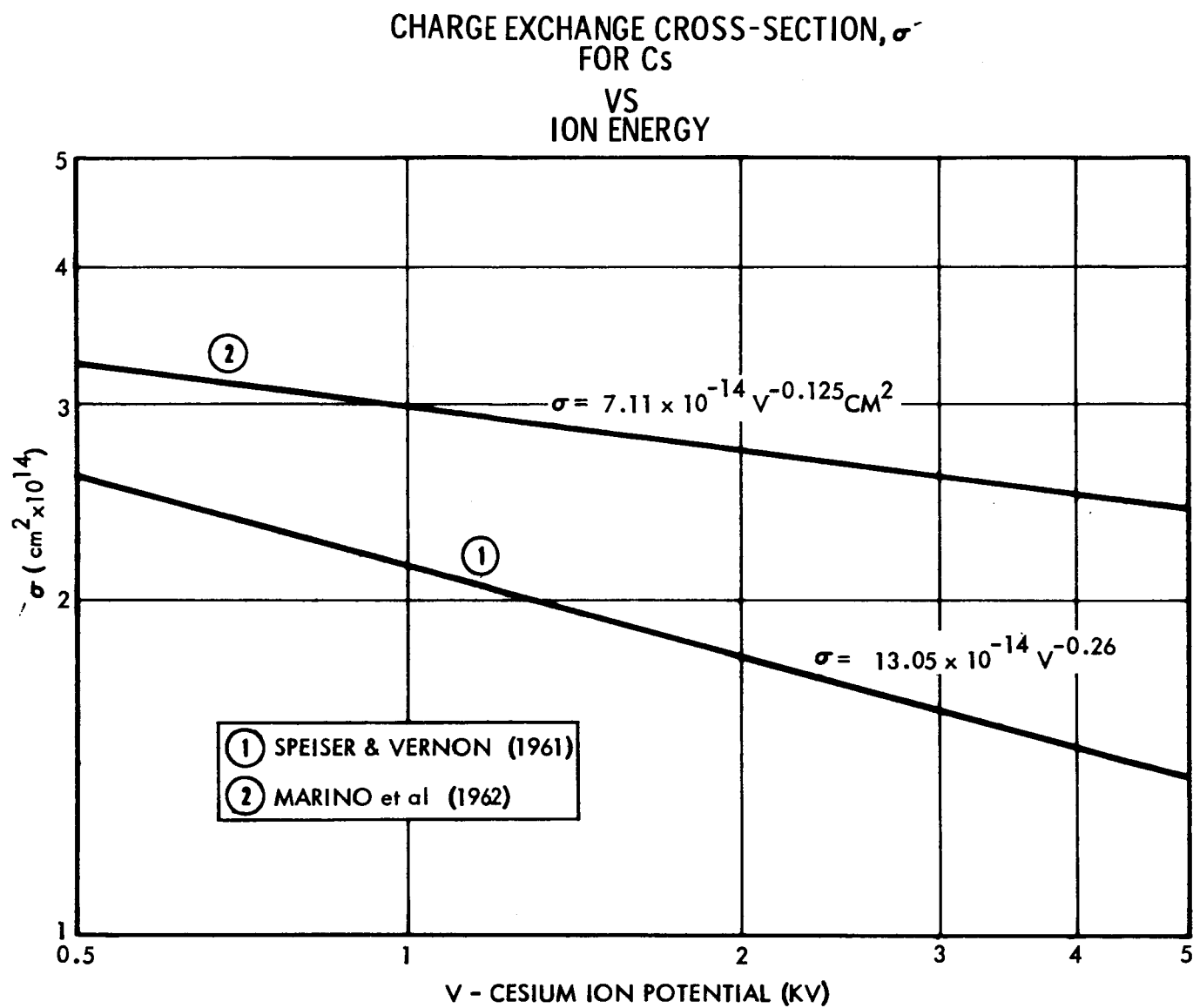
$$\dot{m}_a = k_o \, V_o^{(p+q)} \cdot D^{(p+q)} \cdot x_a \cdot \psi_a \qquad (14)$$

where

$$\psi_a = \int_o^1 (1 - P_y) \, y^{4/3(p+q)} \, [y^{-4/3} - 1]^q \, dy \qquad (15)$$

where P_y equals P_x for each value of y corresponding to x.

This conversion yields an integral which is a definite integral and not a function of x. However, the escape probability is a function of decel ratio at any given value of y. Consequently Eq. (15) must be evaluated as a function of accel ratio before the relative erosion rate can be determined.

Brewer's[11] computer program for calculating the escape probability for charge exchange ions in a Hughes Research Laboratory parallel slit design yields results which are plotted in the normalized curves of Figure 63. By using these values for P_y Eq. (15) can be evaluated by numerical integration.

In order to accomplish this we first plot F(y) as a function of y where

$$F(y) = y^{4/3(p+q)} \, [y^{-4/3} - 1]^q \qquad (16)$$

Eq. (16) is plotted as a function of y for the case of p = -.125 and q = +.825 in Figure 64. From these two graphs (Figures 63 and 64) ψ_a can be calculated for various values of D. The results are plotted in Figure 65.
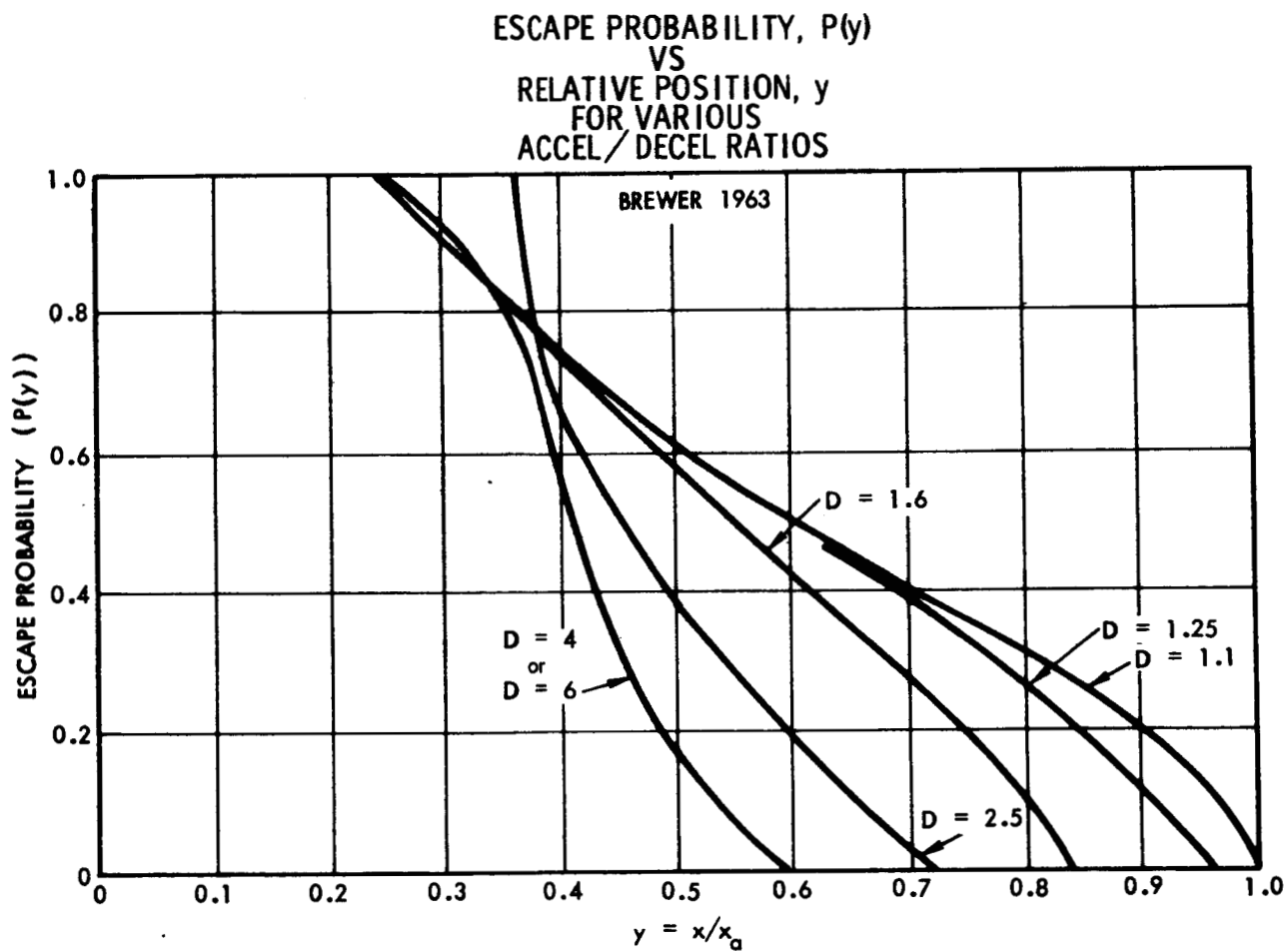
Figure 63. Computer plot of escape probability
in the accel region for various accel-
decel ratios (Brewer[11]).

$$F(y) \text{ vs } y$$

$$F(y) = y^{(4/3)(p+q)} \cdot \left| y^{-4/3} - 1 \right|^q$$

$$p = -0.125, \quad q = +0.825$$
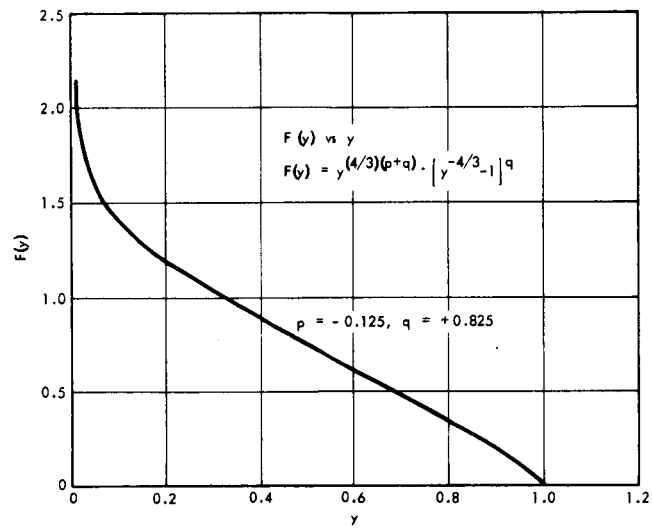
Figure 64. F(y) vs y.
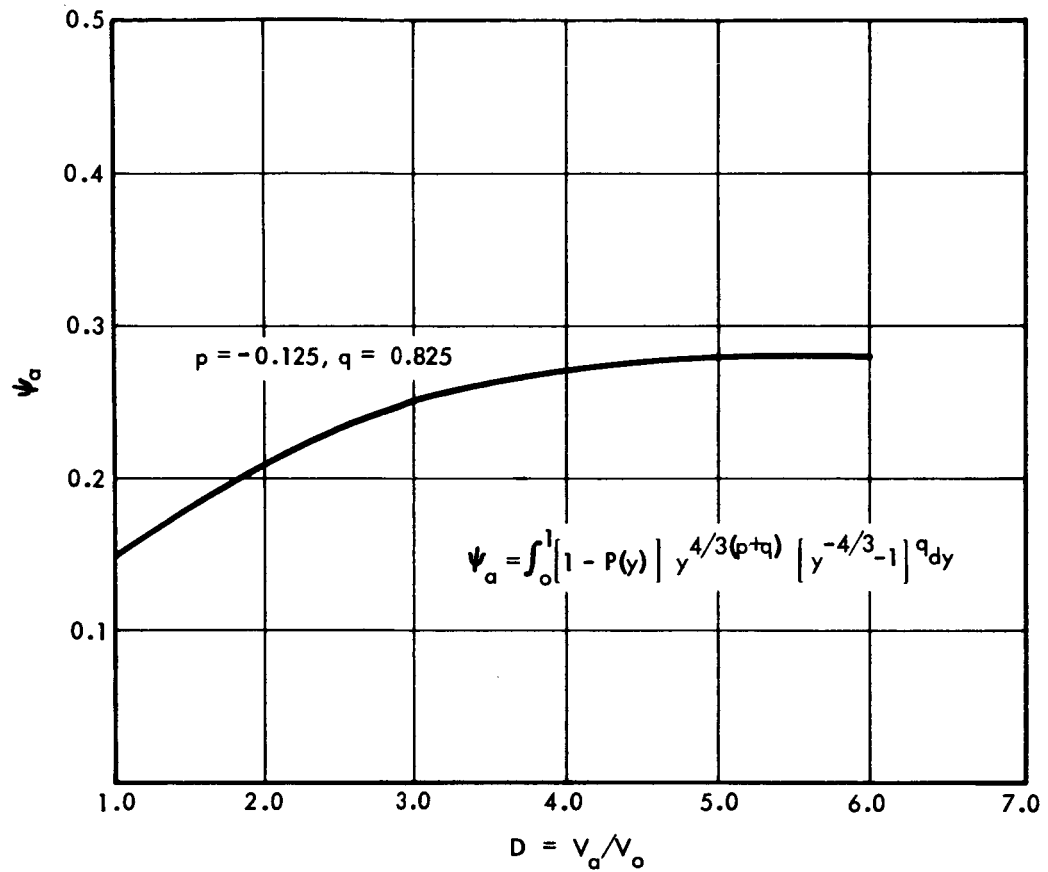
Figure 65. The function ψ_a vs D.

Figure 65 illustrates two important facts: (1) the erosion rate due to charge exchange ions formed in the accel region increases by almost a factor of 2 as the accel-decel ratio, D, is increased; and (2) the relatively low value of ψ_a for all values of D indicates a significant reduction in erosion rate because of the finite escape probability. If P_y were zero for all values of y in Eq. (15), the value of ψ_a would be .79* which is 3 to 5 times higher than the values of Figure 65.

Such a result could also be anticipated from a purely qualitative argument. Because the charge exchange cross-section decreases with ion energy the greatest density of cesium ions will occur in the near vicinity of the ionizer (small values of x or y). These ions will also do the most damage because of their high final velocity. Fortunately, they are formed in a region close to the beam forming optics and hence have a high escape probability.

* In this case (15) can be evaluated exactly. It can be shown that

$$\psi_a \ (P_y = 0) = 3/4 \ \Gamma \ (N) \ \Gamma \ (M) \ / \ \Gamma \ (M + N)$$

where

$$M = q + 3/4, \quad N = q + 1$$

146

6.   MASS REMOVAL RATES DUE TO CHARGE EXCHANGE IONS FORMED IN THE DECEL REGION

Mass erosion rates due to charge exchange ions formed in the decel region can be calculated by evaluation of Eq. (10b).

Substituting the appropriate values of V_b and V_c [from Eqs. (5) and (6)] into (10b) yields

$$\dot{m}_d = b^{(p+q)} k_d \int_0^{x_d} (x_o^{4/3} + x^{4/3})^p (x_d^{4/3} - x^{4/3})^q \, dx$$

$$= (b x_d^{4/3})^{p+q} \cdot k_d \int_0^{x_d} [(x_o/x_d)^{4/3} + (x/x_d)^{4/3}]^p \cdot [1 - (x/x_d)^{4/3}]^q \, dx$$

(17)

From the definitions of Eqs. (3) and (4) Eq. (17) can be written

$$\dot{m}_d = V_d^{p+q} \cdot k_d \int_0^{x_d} [1/(D-1) + (x/x_d)^{4/3}]^p [1 - (x/x_d)^{4/3}]^q \cdot dx \qquad (18)$$

By transforming to $z = x/x_d$ and after converting from V_d and x_d terms to V_o and x_a [by means of (2) and (3)] Eq. (18) becomes:

$$\dot{m}_d = V_o^{p+q} \cdot x_a \cdot k_d \cdot \frac{(D-1)^{q+3/4}}{D^{3/4}} \cdot \psi d \qquad (19)$$

where

$$\psi_d = \int_0^1 [1 + (D-1) z^{4/3}]^p [1 - z^{4/3}]^q \, dz \qquad (20)$$

Eq. (20) has been computed for the case of $p = -.125$ and $q = .825$. The results are plotted in Figure 66. Note that ψ_d is relatively insensitive to accel ratio, but generally _decreases_ as D increases.

147

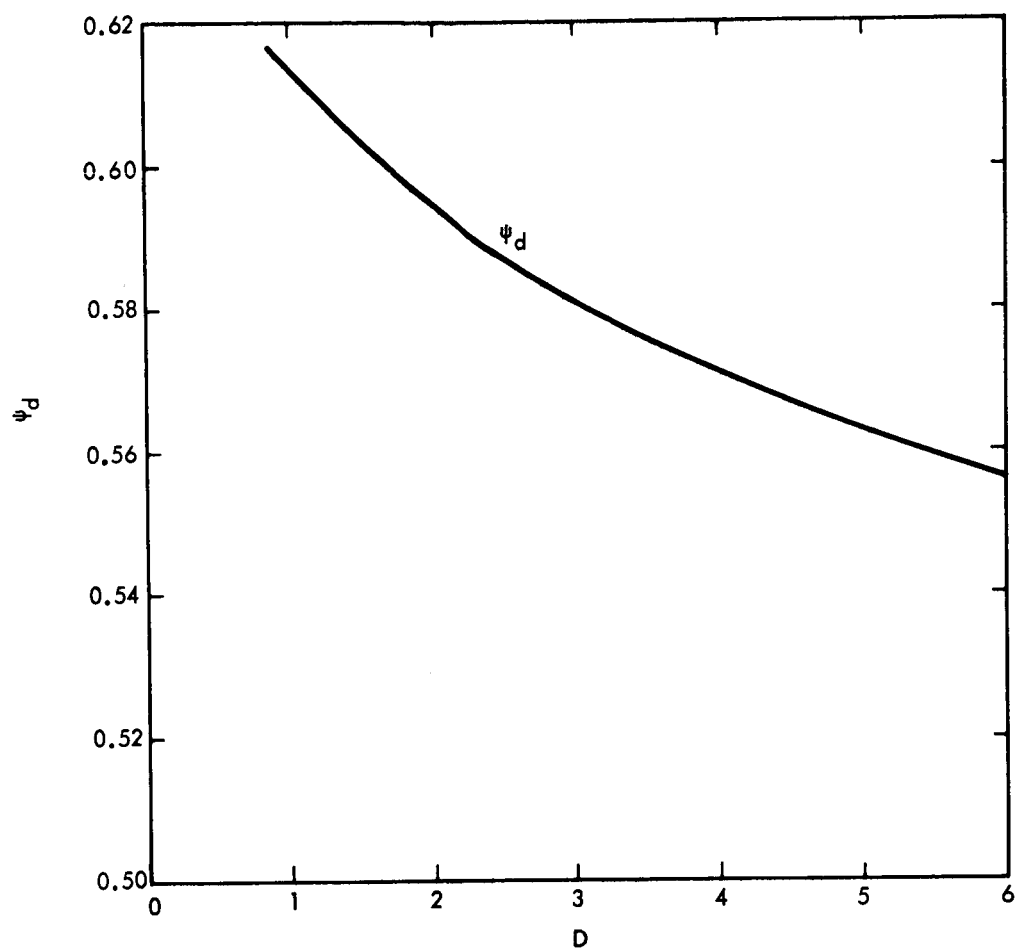Figure 66. The function ψ_d vs D.

7. EROSION DUE TO IMPERFECT OPTICS

For the model for direct impingement it will be assumed there is a region of area w which produces ion emission that is not focussed by the optical system and hence leads to direct erosion of the accel electrode. As an example w might be thought of as a small equivalent flat area along the ridge of a focussing electrode. It is assumed that this area exists because of limitations on fabrication tolerances and that the magnitude of w is independent of engine scaling. As the scale of other parts of the system are reduced the relative importance of w increases until eventually it dominates the electrode geometry. Clearly this sets a lower limit to the usable accelerator distance. The question is what is this lower limit? The procedure again is to find the scaling law for ridge erosion so that this process can be included in the model. Only two factors need be considered; the fraction of the total area represented by w as x_a is changed and the change in sputtering yield as V_a is changed. Increasing scale will reduce the relative importance of w but will increase the sputtering yield due to the higher V_a required to maintain the current density constant.

It will be assumed that w is nonporous so that propellent feed to it occurs only because of the backscattering of neutral atoms from the electrode. (Other models for nonscalable effects leading to direct impingement such as grid alignment tolerances or imperfections in shaping the ion optical surfaces lead to similar scaling relationships but different dependences on neutral emission.) The feed rate will be dependent on the electrode backscattering factor G and the neutral current $\alpha J/(q/m)$. This model is illustrated in Figure 67.

The fraction of the backscattering neutrals that strike w and hence strike the electrodes is w/x, where x is the spacing between adjacent ridges and is assumed proportional to the accel distance. Hence, the erosion rate will be

$$\dot{m}_s = \frac{J\alpha G \ S_o V_a^q}{(e/m)} \cdot \frac{w}{x_a} \tag{21}$$

149

EROSION DUE TO IMPERFECT OPTICS

$$\dot{m}_i = \frac{J a_o GS_o V_a^q}{(e/m)} \cdot \frac{w}{x_a}$$
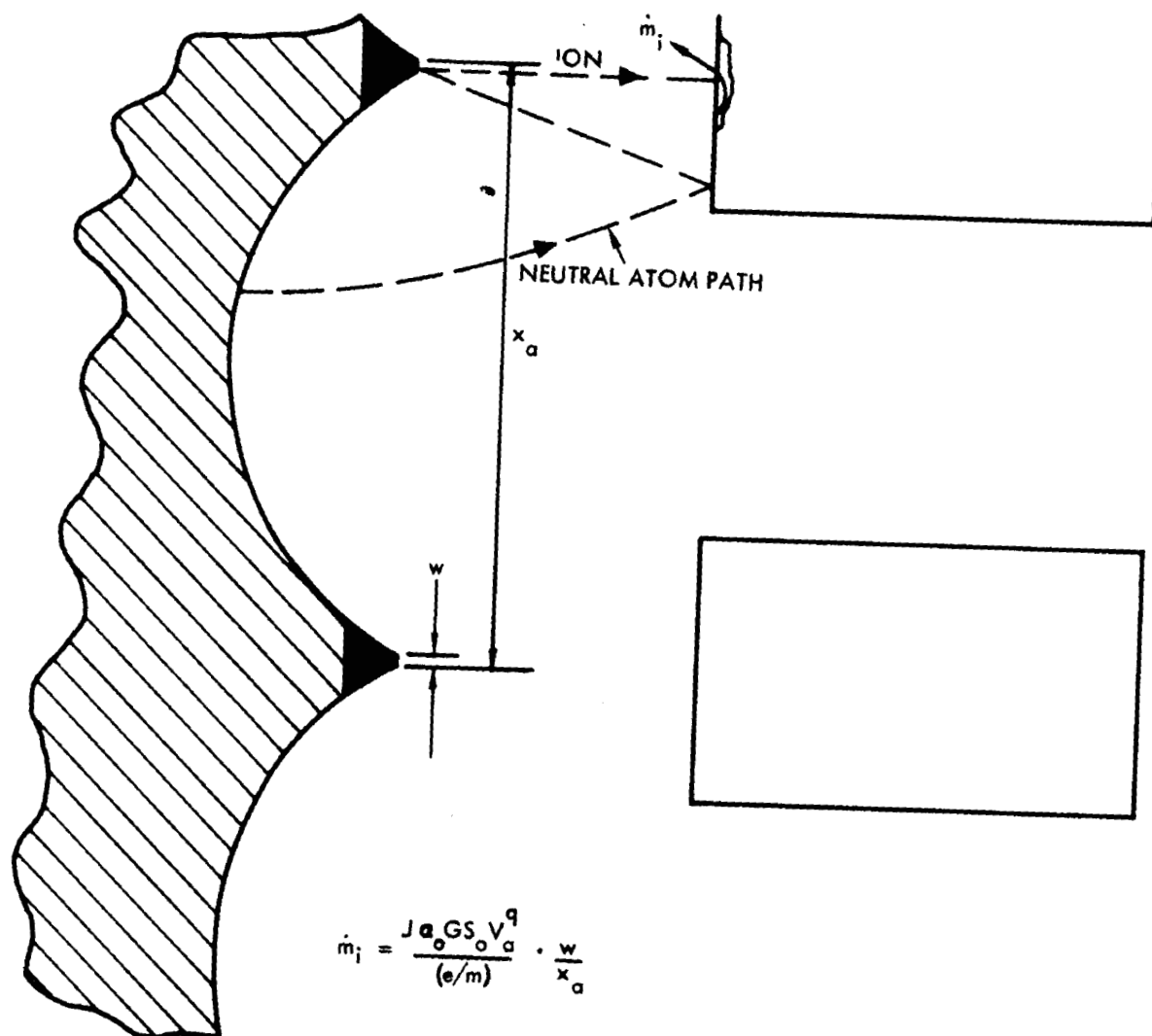
Figure 67.   Imperfect optics as a source of
electrode erosion (model).

As will be apparent in the next section it is convenient to write Eq. (21) as follows:

$$\dot{m}_s = k_s \; V_o^{\;q} \; D^{(q-3/2)} \cdot x_a \qquad (22)$$

where

$$k_s = \frac{J\alpha G \; S_o w}{(e/m) \; x_o^{\;2}} \qquad (23)$$

Eq. (22) follows from the relationships between V_a, x_a and D as defined in Eq. (2).

8. RELATIVE ELECTRODE LIFE AS A FUNCTION OF ACCEL RATIO

Eqs. (14), (19) and (22) represent en toto, the mass erosion rate of the accel electrode due to both charge exchange ions and direct impingement. In order to compare the electrode lives associated with engines having various accel-decel ratios we make the assumption that failure is represented by a fixed fraction of the original electrode mass being eroded away. This would only be in error if the distribution of impinging ions over the electrode surface varied drastically with D. Such is not the case, however.

Let the mass per unit area which can be eroded be represented by M. According to our scaling model M will increase in proportion with x_a, or

$$M = a\, x_a \tag{24}$$

where

$$a = \text{constant.}$$

Electrode life, L_a, will then be

$$L_a = M/[\dot{m}_a + \dot{m}_d + \dot{m}_s] \tag{25}$$

Substituting (14), (19), (22) and (24) into Eq. (25) yields

$$L_a = a x_a / [k_o\, V_o^{p+q} \cdot x_a \cdot \psi_a \cdot D^{(p+q)} + k_d\, \psi_d\, \frac{(D-1)^{(q+3/4)}}{D^{3/4}} \cdot x_a \cdot V_o^{(p+q}$$

$$+ k_s\, V_o^q\, D^{(q-3/2)} \cdot x_a] \tag{26}$$

for the general case. Defining L_o as the electrode life for the engine which does not require accel-decel (i.e. D = 1) we have from Eq. (26)

$$L_o = a\, x_o/x_o\, [k_o\, \psi_o\, V_o^{p+q} + k_s\, V_o^q]$$

$$= a\, x_o/k_o\, V_o^{p+q} \cdot \psi_o x_o (1 + f) \tag{27}$$

152

where

$$\psi_0 = \text{value of } \psi_a \text{ for } D = 1, \text{ and}$$

$$f = \frac{k_s V_0^{-p}}{k_0 \psi_0} \tag{28}$$

The relative electrode life of the two engines is equal to the ratio L_a/L_0. From (26) and (27)

$$\frac{L_a}{L_0} = \frac{1 + f}{\left[\frac{\psi_a}{\psi_0} D^{(p+q)} + \frac{n_d}{\psi_0} \frac{(D-1)^{(q+3/4)}}{D^{3/4}} + f D^{(q-3/2)}\right]} \tag{29}$$

Eq. (29) can be rewritten in terms of spacing ratio R [by means of Eq. (2)]. If we make this substitution and refer the life L_a to that of the diode with perfect optics (f = 0) we have

$$\frac{L_a}{L_0(f = 0)} = \frac{1}{\frac{\psi_a}{\psi_0} R^{4/3(p+q)} + \frac{n_d}{n_0} \cdot \frac{\psi_d}{\psi_0} \frac{(R^{4/3} - 1)^{(q+3/4)}}{R} + f R^{[4/3)q-2]}} \tag{30}$$

This is the expression for the life of an accel-decel system with spacing ratio R compared to that of the equivalent simple diode. p and q are the exponents for the charge exchange cross-section and sputtering yield functions respectively.

The terms in the denominator from left to right respectively represent the charge exchange in the accel region, the charge exchange in the decel region and direct impingement erosion. Each term has been normalized by the electrode mass so that they show electrode durability rather than absolute erosion rates. Only ψ_a and ψ_d vary with the spacing ratio R. All other terms on the right side of Eq. (30) are constants and independent of engine scale.

Both charge exchange erosion terms increase with engine scale while the direct impingement term decreases. Because ψ_a and ψ_d are functions of R a

quantitative analysis is required to determine the upper limit of the factor f before direct impingement becomes the dominant source of electrode erosion. This is done in the following section.

9. QUANTITATIVE EVALUATION OF THE SCALING FACTOR

A plot of relative life is a function of engine scale (R) requires knowledge of the various constants of Eq. (30). The values of p and q which have been used in the example calculations in the previous sections - namely - .125 and + .825 respectively are considered to best represent the published data for the case of a copper electrode and cesium ions. Thus we will employ the values of ψ_a and ψ_d plotted in Figures 65 and 66 respectively.

The ratio of neutral densities n_d/n_o is calculated assuming a reflection factor of G from the accel electrode and G' from the decel electrode (when the latter is used).

Without a decal electrode:

$$\frac{n_d}{n_o} = \frac{1 - G}{1 + G} = .1765 \text{ for } G = .7$$

This value of G corresponds to the reflection factor for the TRW Systems engine design.

With a decel electrode:

$$\frac{n_d}{n_o} = \frac{1 - G}{1 + G} (1 + G' + GG' + GG'^2 +)$$

$$= \frac{1 - G}{1 + G} \cdot \frac{1 + G'}{1 - GG'} = .343 \text{ for } G = .7 \text{ and } G' = .4$$

The value of .4 for G would be obtained with a decel electrode composed of $.31X_a$ diam. wires.

The .343 value is probably slightly low because of the lower operating temperature of the decel electrode.* Further, there will be a small rise in neutral density in the accel region because of reflection from the decel electrode. These corrections are small and hence will be neglected.

---

* lowering the velocity of reflected ions, hence increasing the neutral density.

155

Substituting these values into Eq. 30 leads to thrustor life curves as shown in Figure 68. The abscissa is scaled in terms of either accel-decel ratio D on the spacing ratio R. The ordinate is the electrode life relative to that of the equivalent diode with no direct impingement (same current density and net ion potential). Curve a shows the decrease in life due to increasing charge exchange in the accel region as the spacing ratio R is increased. In spite of the increased electrode mass it is seen that increasing R from 1 to 3 decreases life by more than a factor of five from this effect alone. Curve b shows the total effect of charge exchange erosion with the abrupt decrease at D=3 being caused by the addition of a decel electrode. The combined effects of charge exchange decrease the life at D=3 to 13% of that of the perfect diode. Curves c, d and e show the additional effects of direct impingement for f = 1 corresponds to equal erosion from charge exchange and direct impingement in the diode configuration (R=1). It is apparent that even in this severe condition there is no life advantage to be gained by going to accel-decel systems to increase the dimensions because the reduction in direct im-pingement is more than offset by increased charge exchange. Examination of the curves shows that the charge exchange in the decel region alone offsets the reduction in direct impingement leaving the increased charge exchange in the accel region uncompensated.

Further calculation shows that there is no life advantage in scaling up the engine size if the factor f is less than 4.25. What this means in terms of machining tolerance for the TRW Systems engine is cal-culated in the next section.

156
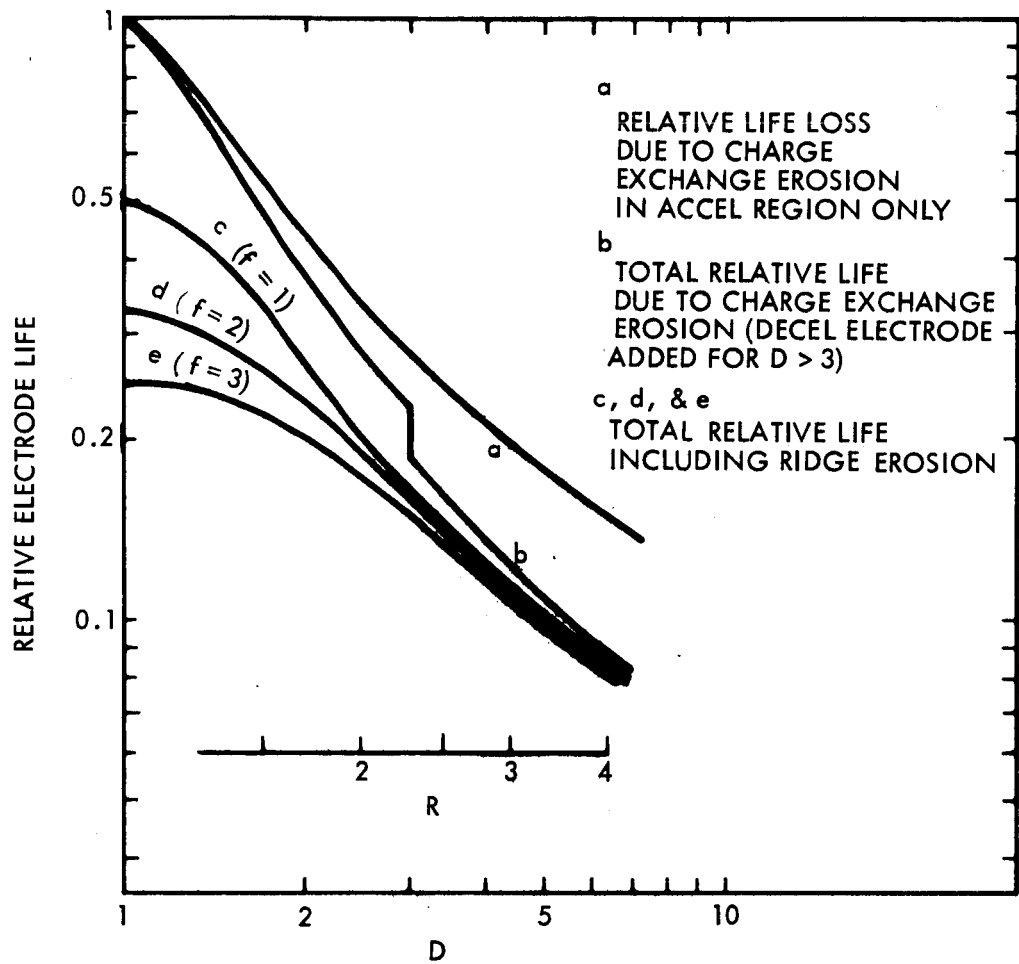
Figure 68. Relative electrode life as a function
of accel-decel ratio for perfect and
imperfect optics.

10. RELATIONSHIP BETWEEN THE MACHING TOLERANCES AND EROSION DUE TO IMPERFECT OPTICS

Evaluation of f by means of (11), (23), (28) and Figure 65 yields

$$f = \frac{k_s}{k_o} \frac{V_o^{-p}}{\psi_o}$$

$$= \frac{J \, \alpha \, G \, S_o \, W/x_o^2}{J \, \sigma_o \, n_o \, S_o} \cdot \frac{V_o^{(.125)}}{.15}$$

For emitter temperature around 1500°K neutral density in the accel region is

$$n_o \simeq 5 \times 10^{+14} \, \alpha J \, (1 + G) \, \text{atoms/cm}^3 \qquad (31)$$

From curve 2 of Figure 58 the charge exchange cross-section at 1 volt is

$$\sigma_o = 7.11 \times 10^{-14} \, \text{cm}^2 \qquad (32)$$

This curve also yields the value of p = -.125 used in the calculations for charge exchange erosion.

$V_o^{(.125)}$ ranges from 2.4 to 2.7 for the voltages between 1000 and 3000 volts. A nominal value of 2.6 (exact at V_o = 2000V) is selected. Substituting these values in the above expression we have (for G = .7)

$$f = \frac{.7 \times 2.6}{7.11 \times 10^{-14} \times 4 \times 10^{14} \times 1.7 \times .15} \, w/x_o^2 \, J$$

$$= .2 \, w/x_o^2 J \qquad (33)$$

where w and x_o are in cm, J is ion beam density in amperes per cm^2. Equation (33) was used to generate the table listed below for the TRW-Systems 1 mm diode (x_o = .1 cm) engine.

TABLE I

f as a function of w and J

$$[x_o = .1 \text{ cm}]$$

W inches	@ J = .01	@ J = .02	@ J = .04 amp/cm^2
.0002	1.0	.5	.25
.0004	2.0	1.0	.5
.0006	3.0	1.5	.75
.0008	4.0	2.0	1.0

The present fabrication technology associated with this design yields an equivalent flat on the contour flute ridges of between .0005 and .001 inches. This is due to the rounded edges caused by the final electropolishing of the machined contour. Obviously further lowering of f can be accomplished by a final honing of the flute ridges. However, it is apparant that present state of the art machining tolerances yield values of f (at practical current densities) well below 4.25. Consequently electrode life would decrease rather than increase if the diode spacing is increased.

11. ELECTRODE LIFE AS A FUNCTION OF I_{sp}

Generally speaking a mission requires engine operation at a given I_{sp} to obtain maximum rocket efficiency. The duration of the mission will determine the electrode life requirement and hence the maximum operating current density of the ion beam.

If the diode spacing is not adjusted to conform with the mission, both electrode life or rocket efficiency will be penalized. This is forcefully demonstrated in the following calculation.

The mass erosion rates defined by Eqs. (14), (19) and (22) are written to compare engines with different diode spacings all having the same net output beam potential. These can be revised for a particular engine having a diode spacing x_p, which will function as a space charge limited diode at an accelerating voltage V_p. At voltages above V_p the operation will be emission limited and no accel-decel is required. At voltages below V_p, on the other hand, accel-decel is required to achieve the desired current density.

In the latter case, the engine is operated with

$$V_a = V_p$$

$$V_d = V_p - V_o$$

and the accel-decel ratio is

$$D = \frac{V_a}{V_o} = \frac{V_p}{V_o}$$

In terms of V_p Eqs. (14), (19) and (22) become

$$\dot{m}_a = k_o \, \psi_a \, x_p \, V_p^{p+q} \tag{34}$$

$$\dot{m}_d = k_d \, \psi_d \, x_p \, \frac{(D-1)^{q+3/4}}{D^{(p+q+3/4)}} \cdot V_p^{p+q} \tag{35}$$

and

$$\dot{m}_s = k_s \, V_p^{q} \, x_p \tag{36}$$

160

If the allowable mass which can be eroded (per cm^2 of projected beam) is M the electrode life L will be [by Eqs. (25), (34), (35), and (36)]

$$L = \frac{M}{k_o V_p^{p+q} \cdot \psi_o \cdot x_p} \cdot \frac{1}{\left[\frac{\psi_a}{\psi_o} + f + \frac{k_d}{k_o} \frac{\psi_d}{\psi_o} \frac{(D-1)^{q+3/4}}{D^{(p+q+3/4)}} \right]} \tag{37}$$

where f is defined by Eq. (28), and ψ_o is the value of ψ_a for D = 1.

Eq. (37) applies to the accel-decel situation only — i.e. $V_o < V_p$. If the engine is operated above the perveance limit (for the emission limited case) there is a slight reduction in the value of ψ_a due to a more linear potential distribution in the accel region. This modest increase in relative life is completely masked by the rising sputtering yield due to the increased voltage however.

Neglecting the small correction for ψ_a, operation above V_p yields an electrode life

$$L = \frac{M}{k_o V_o^{p+q} \psi_o x_p (1 + f)} \quad \left(V_o \gtrsim V_p \right) \tag{38}$$

Relative life, referred to that when the engine is operated as a diode (at V_p) can be written in terms of the I_{sp} of the exhaust beam (I_o) where $I_o = 123 \sqrt{V_o}$ (for a cesium engine).

From Eq. (37) and (38) we obtain

$$\left. \begin{aligned} \frac{L}{L_p} &= 1/ \left[\frac{\psi_a}{\psi_o} + f + \frac{k_d}{k_o} \cdot \frac{\psi_d}{\psi_o} \frac{[I_p^2/I_o^2 - 1]^{q+3/4}}{\frac{I_p}{I_o}^{2(p+q+3/4)}} \right] \\ &\quad \text{for } I_o < I_p \\ &= \left(\frac{I_p}{I_o} \right)^{2(p+q)} /(1+f) \quad \text{for } I_o > I_p \end{aligned} \right\} \tag{39}$$

and

where L_p = electrode life for an engine with perfect optics (f = 0) operated at V_p and $I_p = 123 \sqrt{V_p}$. That is

$$L_p = M/k_o \; \psi_o \; x_p \; V_p^{p+q} \tag{40}$$

Equation (39) is used to calculate four cases. The same values of the constants p, q and k_d/k_o used in the previous example are employed. Values of ψ_a and ψ_d are those plotted in Figures 65 and 66.

The four cases are:

1) $x_p = x_o$, f = 0

2) $x_p = x_o$, f = 1

3) $x_p = 2 x_o$, f = .25

4) $x_p = 3 x_o$, f = .11

The results are plotted in Figure 69 where relative life is plotted as a function of I_{sp} normalized to the value of I_p for $x_p = x_o$. Cases 2), 3) and 4) represent three emitters with equal machining tolerances and diode spacings of say .1, .2 and .3 cm respectively. The relative values of I_p for various values of x_p are

$$\frac{I_1}{I_2} = \left(\frac{x_1}{x_2} \right)^{2/3}$$

The conclusions to be drawn from the curves of Figure 69 are the following:

1) Maximum life for any engine will be obtained by operating it as a space charge limited diode. The life decreases rapidly at specific impulses <u>above</u> or <u>below</u> this optimum.

2) The larger engines still show less electrode life (in this particular example) even when operated at their optimum I_{sp}. Scaling up the engine would not yield improved life if the value of f for the smallest engine is less than 1.1. This is almost a factor of four higher than the break-even value of f in the previous case (equal I_{sp} operation).
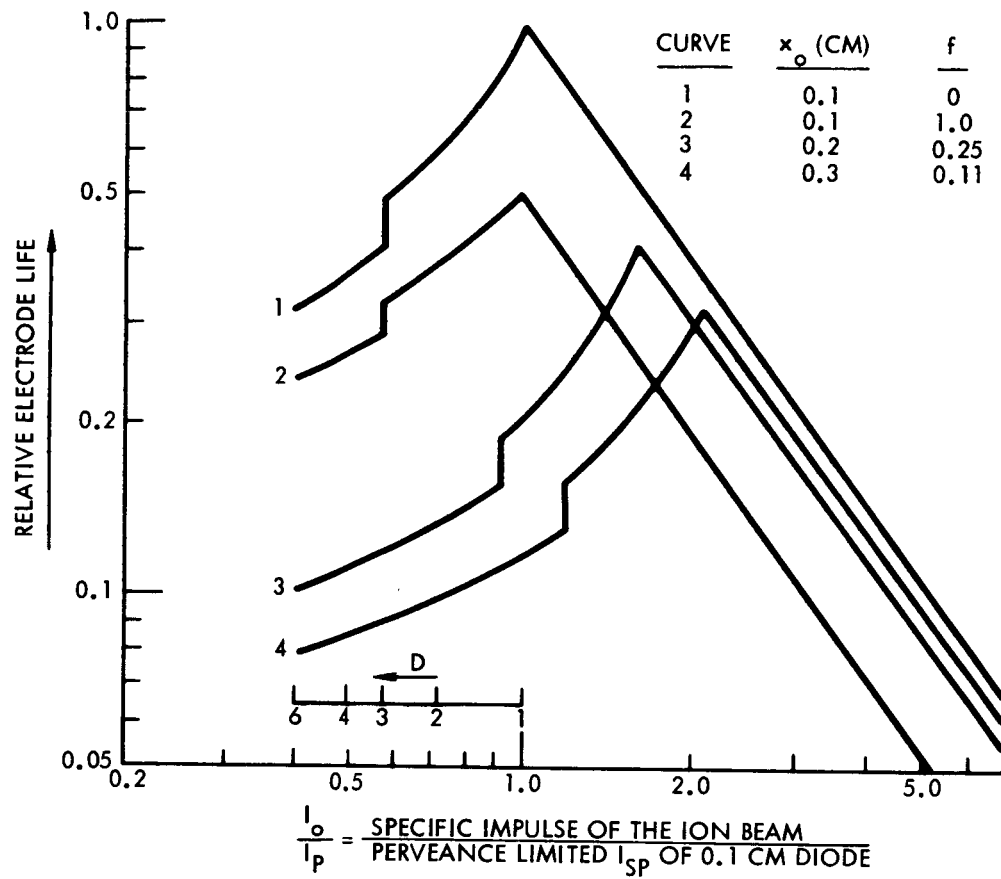
162

Figure 69. Relative electrode life as a function of the beam I_{sp} (normalized) for four engine designs.

12. THE WEIGHT PENALTY ASSOCIATED WITH OFF-OPTIMUM EXHAUST BEAM VELOCITY

In appendix I of reference (3) the rocket efficiency is calculated as a function of engine I_{sp} for various missions. The concluding remarks include the following statement: "Operating a given thrustor at a specific impulse higher than the mission I_{sp} is a notably ineffective way of improving mission performance".

These remarks were primarily directed toward prime propulsion missions where the velocity increment of the rocket is quite large. Because there are now more station keeping missions for electric thrustors than prime propulsion a somewhat broader evaluation is required. The following approximations are useful:

(1) If the weight of the thrustor system is specified then the velocity increment Δv gained by a thrustor operating at a specific impulse, I, compared with that obtained from an engine operated at the mission specific impulse[*], I_m, is approximately[**]

$$\frac{\Delta v}{\Delta v_m} \cong \frac{2}{(I/I_m + I_m/I)} \tag{40}$$

(2) If, however, the Δv requirement is fixed the relative thrustor system weights is approximately by the expression

$$\frac{M}{M_m} = (I/I_m + I_m/I)^r /2 \tag{41}$$

The power function, r, varies with the Δv requirement. For small Δv's and/or station-keeping applications its value is very nearly unity. In this case the weight penalty is only 25% when $I = 2I_m$.

[*]   Optimum mission I_{sp} is defined in chapter 4 of reference (20)
[**]   Assuming both thrustors have the same electrical efficiency and propellant utilization at any given I_{sp}.

164

For prime propulsion missions the magnitude of r increases rapidly with the Δv requirement. For example, when

$$\Delta v = v_c/2$$

is required (where v_c is the characteristic velocity* of the power plant) the value of r is about 2.7. In this case the weight penalty for a 2/1 ratio of operating to mission I_{sp} is 590%!

Returning to the three engine designs of Figure 69 let us calculate electrode and weight penalties relative to the 1mm engine for a prime propulsion mission requiring this amount of Δv. The results which are tabulated below uses a fictitious value for electrode life and thrust system weight, for the 1mm thrustor assuming, in addition that $I_p = I_m$ for this thrustor.

PRIME PROPULSION MISSION

mission time: 1 year
I_m = 5000 seconds
$\Delta v/v_c$ requirement: 0.5

Case No. 1 Operation of each thrustor at I_m = 5000 sec.

ENGINE	DIODE SPACING	ELECTRODE LIFE	THRUSTOR SYSTEM WEIGHT
1	.1 cm	2 years	1000 lbs
2	.2 cm	.86 years	1000 lbs
3	.3 cm	.46 years	1000 lbs

Case No. 2 Operation of each thrustor at its optimum I_{sp} (for electrode life)

ENGINE	ENGINE I_{sp} (SECONDS)	ELECTRODE LIFE	THRUSTOR SYSTEM WEIGHT
1	5000	2 years	1000 lbs
2	7900	1.66	1310 lbs
3	10,400	1.27	7200 lbs

* Characteristic velocity, first defined by Irving[21] can be expressed by the relation
$$v_c = \sqrt{2\tau/\xi}$$
where τ = mission time and ξ = specific weight of the power plant

In the first case the large scale engines cannot meet the electrode life requirement of the mission. By operating each thruster in the space charge limited mode all meet the electrode life requirement, however, the 2 mm engine package now weighs 31% greater and the 3 mm engine 620% greater than the 1 mm engine. This would not likely be an acceptable method of increasing the electrode life.

13. SUMMARY AND CONCLUDING REMARKS

(1) For practical electric thrustors where the accel electrode is the life limiting factory the best rocket efficiency can be achieved by designing the perveance of the accelerator to operate <u>without</u> accel-decel at the optimum I_{sp} of the mission.

(2) When erosion due to imperfect optics becomes a significant fraction for a given design, improving the machining accuracy is a much better way of improving electrode life than reverting to accel-decel.

One factor which has not been mentioned in this analysis is the arrival rate of sputtered electrode material on the surface of the emitter. Obviously if electrode life decreases as its size is increased this flux of sputtered atoms is increased at an even faster rate.

In comparing the three engines in the tabulation of the previous section the relative arrival rate of sputtered atoms (when all are operated at 5000 sec) would be 1, 4.65 and 13 for engine no's 1, 2 and 3 respectively.

The experiments of Shelton[8] and Wilson [10] with measurement of re-evaporation rates for various potential electrode materials show that the arrival rate is a very significant factor in determining emitter work function and its life (particularly when such tungsten sintering agents as nickel are used). This factor alone could place a very restrictive upper limit on the allowable beam current density as engine scale is increased.

REFERENCES

1. J. C. Beynon, S. G. Forbes and P. W. Kidd, "Program of Large Hi Perveance Ionizer Studies", NASA CR-54325, September 1965

2. S. G. Forbes, J. C. Beynon, D. A. Gordon and M. E. Kirkpatrick, "Design of a Modular Source Contact Ion Engine", ASD-TDR-63-545, July 1963.

3. S. G. Forbes and J. C. Beynon, "Design of a Modular Source Contact Ion Engine", AFAPL-TR-64-126, November 1964.

4. M. E. Kirkpatrick and R. A. Mendelson, "Development of Porous Ionizer Materials", AIAA Paper 66-221, March 1966.

5. P. Clausing, Ann Physik, 12, 961 (1932) – See also pp. 96 of Saul Duschman's "Scientific Foundations of Vacuum Technique", 2nd Ed. 1962. (John Wiley and Sons)

6. D. F. Hall, A. Y. Cho and H. Shelton, "An Experimental Study of Porous Metal Ionizers", AIAA Paper 66-218, March 1966.

7. A. Y. Cho and H. Shelton, "Ion Emitter Studies", NASA CR-54045, May 1964.

8. A. Y. Cho, D. F. Hall and H. Shelton, "A Program of Analytical and Experimental Study of Porous Metal Ionizers", NASA CR-54325, July 1965.

9. K. B. Chenve and E. T. Pitkin, "Sputtering at Acute Incidence", J.A.P., Vol. 36, pp. 3542-44, November 1965.

10. R. G. Wilson, "Ion Thrustor Electrode Surface Physics Studies", NASA CR-54679, October 1965.

11. G. R. Brewer, "On the Nature of Leakage Currents in Cs Contact Ion Engines", Hughes Research Labs, Res. Dept. No. 281, pp. 69, August 1963.

12. B. Thompson, G. Kuskevics and M. LaChance, "Composite Cesium Ionizers with Enhanced Life Time Characteristics", AIAA Paper 66-219, March 1966.

13. V. E. Krohn, "Negative Ions From Positive Cesium Ion Bombardment", J.A.P. 33, 3523-3525, December 1962.

14. G. Sohl, R. C. Speiser and J. A. Wolters, "Life Testing of Electron Bombardment Cesium Ion Engines", AIAA Paper 66-233, March 1966.

15. M. P. Ernstene, A. T. Forrester, G. W. Purmal and R. M. Worlock, "Surface Ionization Engine Development".

16. Magnuson et al, Gen. Dynamics/Astronautics - Contract NASA-1592

17. H. P. Smith, Jr., R. C. Herlbut and T. H. Pigford, "Investigation of Kilovolt Ion Sputtering", NASA CR-54406, July 1965.

18. R. C. Speiser and R. H. Vernon, "Cesium Ion-Atom Charge Exchange Scattering", American Rocket Society, October 9-15, 1961.

19. L. L. Marion, A. C. H. Smith and E. Caplinger, "Charge Transfer Between Positive Es Ions and Cs Atoms", Phys., Vol. 128 pp. 2243-2250, December 1, 1962.

20. E. Stuhlinger, "Ion Propulsion for Space Flight", McGraw-Hill, Inc., New York, 1964.

21. J. H. Irving: in Howard S. Seifert (ed), "Space Technology", John Wiley and Sons, Inc., New York, 1959.

NASA (1)
Washington, D.C. 20546
Attn: RNT/James Lazar

NASA-Lewis Research Center
21000 Brookpark Road
Cleveland, Ohio 44135
Attn: Spacecraft Tech. Procurement (1)
        Section (M.S. 54-2)

        Technology Utilization Office (1)
        (M.S. 3-19)

        Technical Information Divn. (1)
        (M.S. 5-5)

        Library (2)
        (M.S. 60-3)

        Spacecraft Tech. Division
        (M.S. 54-1)
          C.C. Conger (M.S. 54-1) (1)
          R. Shattuck (M.S. 54-3) (2)
          F. Kavanagh (M.S. 54-3) (2)

        Electric Propulsion Lab. (M.S. 301-1)
        W. Moeckel (1)

        Report Control Office (M.S. 5-5) (1)

NASA-Scientific & Tech. Info. Facility (6)
P.O. Box 33
College Park, Maryland 20740
Attn: NASA Representative RQT-2448

NASA-Marshall Space Flight Center (1)
Huntsville, Alabama 35812
Attn: Ernest Stuhlinger (M-RP-DIR)

Research & Technology Divn. (1)
Wright-Patterson AFB, Ohio 45433
Attn: AFAPL (APIE-2)/R.F. Cooper

AFWL (1)
Kirtland AFB, New Mexico 87417
Attn: WLPC/Capt. C. F. Ellis

Aerospace Corp. (1)
P.O. Box 95085
Los Angeles, Calif. 90045
Attn: Library/Tech. Documents Group

Jet Propulsion Laboratory (1)
4800 Oak Grove Drive
Pasadena, California 91103
Attn: J. J. Paulson

Electro-Optical Systems, Inc. (1)
300 N. Halstead St.
Pasadena, California 91107

Ion Physics Corp. (1)
South Bedford Street
Burlington, Mass. 02103
Attn: Sam Nablo

TAPCO, Div. of TRW Inc. (1)
New Product Research
23555 Euclid Avenue
Cleveland, Ohio 44117
Attn: R. T. Craig

General Electric Co. (1)
Space Flight Propulsion Lab.
Cincinnati, Ohio 45215
Attn: M. L. Bromberg

Hiram College (1)
Department of Physics
Hiram, Ohio 44234
Attn: Prof. L. Shaffer

Field Emission Corp (1)
611 Third Street
McMinville, Oregon 97128
Attn: L. W. Swanson

Battelle Memorial Institute (1)
505 King Avenue
Columbus, Ohio 43201
Attn: J. Anno

NASA-Langley Research Center (1)
Langley Field Station
Hampton, Virginia 23365
Attn: Technical Library

Colorado State University (1)
Fort Collins, Colorado 80521
Attn: L. Baldwin

General Electric Co. (1)
Missile & Space Divn.
Space Sciences Laboratory
P.O. Box 8555
Philadelphia, Pa. 19101
Attn: P. Gloevsen

University of Illinois
Dept of Electrical Engineering
Urbana, Illinois 61801
Attn: L. Goldstein (1)
        A. Cho (1)